

AD-A134 691

LASER DIAGNOSTIC DEVELOPMENT AND MEASUREMENT AND  
MODELING OF TURBULENT FL (U) DAYTON UNIV OH RESEARCH  
INST A J LIGHTMAN ET AL JUN 83 UDR-TR-83-22

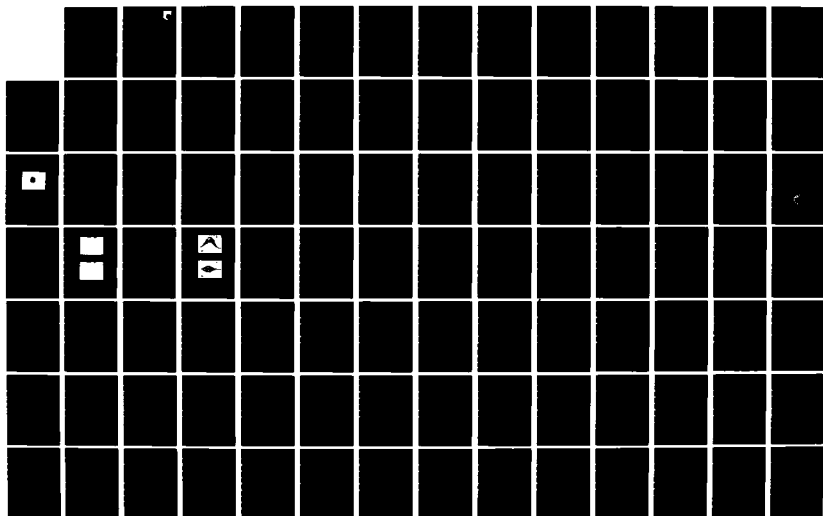
1/2

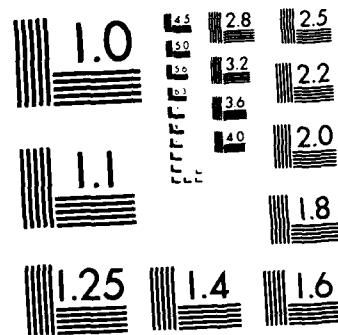
UNCLASSIFIED

AFWAL-TR-83-2044-PT-1 F33615-78-C-2005

F/G 20/4

NL





MICROCOPY RESOLUTION TEST CHART  
NATIONAL BUREAU OF STANDARDS-1963 A

AD-A134 691

AFWAL-TR-83-2044  
Part I



LASER DIAGNOSTIC DEVELOPMENT AND MEASUREMENT AND  
MODELING OF TURBULENT FLOWFIELDS OF JETS AND WAKES

Part I  
Two-Dimensional Laser Doppler Anemometer Studies of Isothermal  
Flowfield in a Ducted Centerbody Combustor

A. Lightman, P. D. Magill, and R. J. Andrews  
University of Dayton  
Research Institute  
Dayton, Ohio 45469

June 1983

FINAL REPORT FOR PERIOD 1 APRIL 1978 - 30 SEPTEMBER 1982

Approved for Public Release, Distribution Unlimited

AERO PROPULSION LABORATORY  
AIR FORCE WRIGHT AERONAUTICAL LABORATORIES  
AIR FORCE SYSTEMS COMMAND  
WRIGHT-PATTERSON AIR FORCE BASE, OH 45433

COPY

NOTICE

When Government drawings, specifications, or other data are used for any purpose other than in connection with a definitely related Government procurement operation, the United States Government thereby incurs no responsibility nor any obligation whatsoever; and the fact that the government may have formulated, furnished, or in any way supplied the said drawings, specifications, or other data, is not to be regarded by implication or otherwise as in any manner licensing the holder or any other person or corporation, or conveying any rights or permission to manufacture use, or sell any patented invention that may in any way be related thereto.

This report has been reviewed by the Office of Public Affairs (ASD/PA) and is releasable to the National Technical Information Service (NTIS). At NTIS, it will be available to the general public, including foreign nations.

This technical report has been reviewed and is approved for publication.

W. M. Roquemore.  
W. M. ROQUEMORE  
Fuels Branch  
Fuels and Lubrication Division  
Aero Propulsion Laboratory

Arthur V. Churchill  
ARTHUR V. CHURCHILL,  
Chief, Fuels Branch  
Fuels and Lubrication Division  
Aero Propulsion Laboratory

FOR THE COMMANDER

Benito P. Botteri  
BENITO P. BOTTERI, Assistant Chief  
Fuels and Lubrication Division  
Aero Propulsion Laboratory

"If your address has changed, if you wish to be removed from our mailing list, or if the addresses is no longer employed by your organization please notify AFWAL/POSF, W-PAFB, OH 45433 to help us maintain a current mailing list."

Copies of this report should not be returned unless return is required by security considerations, contractual obligations, or notice on a specific document.

Unclassified

SECURITY CLASSIFICATION OF THIS PAGE (When Data Entered)

| REPORT DOCUMENTATION PAGE  |   | READ INSTRUCTIONS<br>BEFORE COMPLETING FORM  |
|--|---|--|
| 1. REPORT NUMBER<br>AFWAL-TR-83-2044, Part I   | 2. GOVT ACCESSION NO.<br><b>A134691</b> | 3. RECIPIENT'S CATALOG NUMBER  |
| 4. TITLE (and Subtitle)<br>Laser Diagnostic Development and Measurement and Modeling of Turbulent Flowfields of Jets and Wakes - Part I  |   | 5. TYPE OF REPORT & PERIOD COVERED<br>Final Report for Period<br>1 Apr 1978 - 30 Sept 1982                           |
|  |   | 6. PERFORMING ORG. REPORT NUMBER<br>UDR-TR-83-22   |
| 7. AUTHOR(s)<br>A. J. Lightman, P. D. Magill, and<br>R. J. Andrews   |   | 8. CONTRACT OR GRANT NUMBER(s)<br>F33615-78-C-2005   |
| 9. PERFORMING ORGANIZATION NAME AND ADDRESS<br>University of Dayton<br>Research Institute<br>Dayton, Ohio 45469  |   | 10. PROGRAM ELEMENT, PROJECT, TASK<br>AREA & WORK UNIT NUMBERS<br>P.E. # 62203F,<br>Proj. # 3048,<br>W.U. # 30480596 |
| 11. CONTROLLING OFFICE NAME AND ADDRESS<br>Aero Propulsion Laboratory (AFWAL/POSF)<br>Air Force Wright Aeronautical Laboratories (AFSC)<br><u>Wright-Patterson Air Force Base Ohio, 45433</u>  |   | 12. REPORT DATE<br>June 1983   |
| 14. MONITORING AGENCY NAME & ADDRESS (if different from Controlling Office)  |   | 13. NUMBER OF PAGES<br>126   |
|  |   | 15. SECURITY CLASS. (of this report)<br>Unclassified   |
|  |   | 15a. DECLASSIFICATION/DOWNGRADING<br>SCHEDULE  |
| 16. DISTRIBUTION STATEMENT (of this Report)<br><br>Approved for Public Release, Distribution Unlimited   |   |  |
| 17. DISTRIBUTION STATEMENT (of the abstract entered in Block 20, if different from Report)   |   |  |
| 18. SUPPLEMENTARY NOTES  |   |  |
| 19. KEY WORDS (Continue on reverse side if necessary and identify by block number)<br><br>Laser Doppler Anemometry<br>Recirculating Flow<br>Free Jet Entrainment   |   |  |
| 20. ABSTRACT (Continue on reverse side if necessary and identify by block number)<br><br>A two-dimensional laser Doppler anemometer has been designed to take measurements in a ducted coaxial flow system having a center-body separating the jets. The measurements, made in isothermal flow, can be categorized as: central jet only (CO <sub>2</sub> ); annular jet only (air); and, combined central and annular jet flow. Radial profiles of the axial and radial/azimuthal velocity have been obtained. |   |  |

DD FORM 1 JAN 73 1473

EDITION OF 1 NOV 55 IS OBSOLETE

Unclassified

SECURITY CLASSIFICATION OF THIS PAGE (When Data Entered)

Unclassified

SECURITY CLASSIFICATION OF THIS PAGE(When Data Entered)

20. continued

The central jet only condition approximates a free jet since the central jet diameter is much smaller than the centerbody or duct diameter (1:29.3: 53.2). Measurements of the jet development (diameter, turbulence intensity, etc.) have been compared with free jet studies made by other investigators. Also, a study was made of the isotropy of the turbulent fluctuations and it was determined that fully developed turbulent flow begins further downstream than anticipated. The velocity profiles have been combined with gas sampling measurements to ascertain the jet entrainment. The results show a linear growth of the entrained mass starting at the entrance plane. Downstream (twenty diameters) the rate of growth increases to match past studies in that region.

The annular jet flow creates a recirculation vortex in the wake of the centerbody. The flowfield has been mapped out and the streamlines describing the flow have been obtained throughout the recirculating flow and further downstream. The location and strength of the vortex center has been determined. Velocity scans have been combined to obtain profiles of the average radial velocity and these are plotted (as well as the axial and azimuthal components that are directly measured).

The interaction of the recirculating annular air jet and the central jet has been examined. Profiles of the velocity field have been obtained for several central jet flow conditions. A normalized plot of the location of the central jet stagnation location agrees well with earlier measurements using a one-dimensional laser Doppler anemometer and a different central jet nozzle.

|                    |                                     |
|--------------------|-------------------------------------|
| Accession For      |                                     |
| NTIS GRA&I         | <input checked="" type="checkbox"/> |
| DTIC TAB           | <input type="checkbox"/>            |
| Unannounced        | <input type="checkbox"/>            |
| Justification      |                                     |
| By                 |                                     |
| Distribution/      |                                     |
| Availability Codes |                                     |
| Dist               | Avail and/or<br>Special             |
| A-1                |                                     |



Unclassified

SECURITY CLASSIFICATION OF THIS PAGE(When Data Entered)

## SUMMARY

A two-dimensional Laser Doppler Anemometer (LDA), using polarization to discriminate between the components, has been constructed and used to measure flowfields in a ducted coaxial jet system with a centerbody. The flowfields studied included central jet only, annular jet only, and combined central and annular jets. In all cases the central jet was  $\text{CO}_2$  and the annular jet was air.

The small diameter of the central jet nozzle relative to the centerbody and duct should result in the central jet behaving as a free jet for quite a distance downstream ( $\sim 100$  nozzle diameters in this system). Studies of the jet velocity profile development have been made and compared with other studies in the literature. The velocity measurements have been combined with concentration profiles to yield entrainment by the jet. The values obtained differ from previously published results. The consistency checks available in this system have demonstrated the reliability of these measurements.

The annular-jet-only measurements have been used to compute the streamline locations for the flow. The recirculation vortex established in the wake of the centerbody has been mapped and its center located in both position and strength. Consistency checks of the mass flow across the duct have demonstrated the quality of the measurements.

The coaxial flow measurements have looked at how the central jet perturbs the reverse flow profiles of the annular jet. It was found that as the velocity perturbation was dying out, the effect on the velocity fluctuations became most marked, with the rms velocity fluctuation increasing by almost an order of magnitude over the measurement with no central jet. Axial velocity profiles were measured for several central jet flows and

the results compared with previous measurements using a one-dimensional LDA. With the normalization used the results agree very well, even though different nozzles were used in the two measurements.



## PREFACE

This final report was submitted by the University of Dayton, under Contract No. F33615-78-C-2005. The project was sponsored by the Air Force Wright Aeronautical Laboratories, Aero Propulsion Laboratory, Wright-Patterson Air Force Base, Ohio, under Project No. 3043, Task 05, Work Unit 96. Dr. William M. Roquemore, AFAPL/POSF, was Project Engineer. The program was managed by Dr. Eugene H. Gerber of the University. This report describing the laser Doppler anemometer task was authored by Dr. Allan J. Lightman, the Principal Investigator, and Messrs. P. D. Magill and R. J. Andrews.

The authors wish to express appreciation to the following people for their assistance and support:

- Dr. W. M. Roquemore, for his encouragement and for many helpful discussions;
- Mr. J. S. Stutrud, AFWAL/POSF, for supporting the MODCOMP computer system;
- Mr. R. P. Bradley, AFWAL/POSF and Mr. M. Russell, AFWAL/POFA, for running the flow system;
- Mr. C. E. Orr, UDRI, for his work on the computer software system;
- Mr. M. Horne, UDRI, for his assistance in the construction and maintenance of the LDA system;
- Mr. C. M. Reeves, AFWAL/POSF, who provided his search-and-plot computer programs for generating graphic displays in this report;
- Dr. L. Krishnamurthy, UDRI, for many technical discussions;
- Ms. A. Kite, UDRI, for preparing this report; Ms. A. Cochran, for technical editing.

## TABLE OF CONTENTS

| SECTION |  | PAGE |
|---------|--|------|
| 1       | Introduction   | 1    |
| 2       | Laser Doppler Anemometer   | 7    |
|         | 2.1 Optical Design Criteria  | 13   |
|         | 2.2 Electronic System  | 16   |
|         | 2.3 Data Collection  | 19   |
|         | 2.4 Data Processing  | 21   |
|         | 2.5 Seeders  | 25   |
|         | 2.6 LDA System Check--Laboratory   | 26   |
|         | 2.7 LDA System Check--Tunnel   | 30   |
| 3       | Free Jet   | 35   |
|         | 3.1 Experiments  | 38   |
|         | 3.2 Results  | 40   |
| 4       | Annular Flow   | 81   |
|         | 4.1 Experimental Procedure   | 81   |
|         | 4.2 Results  | 83   |
| 5       | Conclusions  | 121  |
|         | Appendix A--CO <sub>2</sub> Concentration Measurement<br>Profiles for Central Jet Flows Into Air | 123  |
|         | References   | 125  |

# LIST OF ILLUSTRATIONS

| FIGURE |   | PAGE |
|--------|---|------|
| 1      | Schematic Diagram of Ducted Coaxial Flow System with Centerbody.  | 2    |
| 2      | Schematic Diagram of the Anticipated Flow Field.  | 4    |
| 3      | Single-Channel Dual-Scatter Laser Doppler Anemometer Optical Configuration.   | 8    |
| 4      | Two-Dimensional LDA Optical System Using Polarization to Differentiate the Orthogonal Velocity Components.  | 10   |
| 5      | (a) Positions and Polarizations of the Three Optical Beams at the Focusing Lens;<br>(b) Fringe Pattern Observed at LDA Focused Spot.  | 12   |
| 6      | Photograph of Fringe Pattern Observed on a Scattering Screen in the LDA Spot.   | 14   |
| 7      | LDA Spot and Collection Volume Observed by Off-Axis Paraboloid.   | 17   |
| 8      | Electronic System Processing the LDA Signal.  | 18   |
| 9      | One Channel of the LDA Computer Interface.  | 20   |
| 10     | Computer Summary of On-Line LDA Data Analysis.  | 22   |
| 11     | On-Line Computer Plot of Profile Data.  | 23   |
| 12     | (a) Large Seeder Built to Seed the Annular Jet. (b) Bed Mask Used to Ensure Cyclone Action of Flowing Gas.  | 27   |
| 13     | Collected Light as Chopper Passes Through LDA Spot. (a) Chopper at Center of LDA Spot. (b) Chopper Displaced from Center Location.  | 29   |
| 14     | Typical LDA Burst Observed with Bragg Cell Switched Off. (a) $F_{upper} = 2$ MHz and $F_{lower} = DC$ so the pedestal can be seen. (b) $F_{upper} = 2$ MHz and $F_{lower} = 0.1$ MHz. | 31   |
| 15     | Measured and Computed Centerline Entrance Velocities for the Central Jet as a Function of the Inlet $CO_2$ Flow.  | 33   |

# LIST OF ILLUSTRATIONS (Cont'd)

| FIGURE |   | PAGE |
|--------|---|------|
| 16     | Central Jet Nozzle, Designed as Described in ASME Power Test Codes PTC 19.5, 4-1959, Long-Radius Flow Nozzles, Low 3 Series.  | 36   |
| 17     | Schematic of Axisymmetric Jet Flow Showing the Various Regions Encountered in the Flow Development.   | 37   |
| 18     | (a) - (m) Profiles of Velocity Distribution Descriptors Based Upon the First Four Moments.  | 41   |
| 19     | Development of the Full Width of the Central Jet Measured at Half the Velocity Maximum.   | 55   |
| 20     | (a) - (d) Profiles of Velocity Distribution Descriptors Based Upon the First Four Moments.  | 57   |
| 21     | (a) - (f) Profiles of Velocity Distribution Descriptors Based Upon the First Four Moments.  | 61   |
| 22     | Overlays of the Normalized Average Axial-Velocity ( $\bar{w}/\bar{w}_{F0}$ ) and Normalized RMS Axial-Velocity Fluctuations ( $w/\bar{w}_{F0}$ ) for the Flow Conditions of 2, 6 and 16 kg/hr CO <sub>2</sub> . | 67   |
| 23     | Dependence of Average Axial Centerline Velocity on Downstream Location.   | 72   |
| 24     | Variation of Local Axial RMS Turbulence Fluctuation as a Function of Downstream Location.   | 75   |
| 25     | Entrained Mass as a Fraction of Entrance Mass at Each Downstream Measurement Station.   | 76   |
| 26     | On-Axis View of APL Combustor Showing the Three Scan Profiles Taken at the Axial Stations.  | 82   |
| 27     | (a) - (n) Radial Profiles of the Average Axial- and Azimuthal-Velocity and Average Axial- and Azimuthal-RMS Velocity Fluctuations for Annular-Jet-Only Flow of 2 kg/s Air.                                      | 84   |
| 28     | Radial Profiles of the Average Radial Velocity Component at Several Downstream Stations.  | 99   |

# LIST OF ILLUSTRATIONS (Cont'd)

| FIGURE |  | PAGE |
|--------|--|------|
| 29     | Axial Mass and Momentum Flow Computed from the Radial Profiles of the Axial Velocity.  | 100  |
| 30     | Streamlines Describing the Flowfield for the Annular-Jet-Only Flow Condition (2 kg/s air).   | 102  |
| 31     | (a.1) - (g.1) Radial Profiles of the Average Axial and Azimuthal Components of Velocity and RMS Velocity Fluctuations for Central Jet Flow of 6 kg/hr CO <sub>2</sub> and Annula Jet Flow of 2 kg/s Air. | 103  |
|        | (a.2) - (g.2) Expanded Profiles of the Average Axial and Radial Components of Velocity and RMS Velocity Fluctuations Around Centerline.  | 104  |
| 32     | Normalized Centerline Axial-Velocity Profiles Showing the Influence of the Central Jet on the Centerline Recirculation for Each Central Jet Flow Studied.  | 118  |
| 33     | Normalized RMS Axial-Velocity Fluctuation Profiles.  | 119  |
| 34     | Central Jet Centerline Stagnation Location Plotted as a Function of the Central Jet Entrance Velocity.   | 120  |

# LIST OF TABLES

| TABLE |   | PAGE |
|-------|---|------|
| 1     | Operating Conditions for the LDA Measurements   | 5    |
| 2     | Flow Rates Used in Central Jet Studies          | 33   |
| 3     | Profile Measurement Locations                   | 39   |
| 4     | Parameters Describing Centerline Velocity Decay | 74   |

# LIST OF SYMBOLS

|                  |  |
|------------------|--|
| $a$              | Virtual origin of central jet  |
| $D_C, D_F$       | Diameter of centerbody, central jet  |
| $d_m, l_m$       | Diameter and length of LDA measurement spot  |
| $d_f$            | LDA "fringe" spacing   |
| $D$              | LDA laser spacing  |
| $D_{e-2}$        | Laser beam diameter at $e^{-2}$ intensity  |
| $F_D$            | Doppler frequency  |
| $f$              | Focal length of lens   |
| $\hat{k}$        | Unit vector in direction of laser propagation  |
| $L, M, U$        | Lower, middle, upper laser beams for 3-beam geometry                                   |
| $M$              | Mach number  |
| $\dot{m}_0$      | Mass flow rate at inlet plane  |
| $\dot{m}_E$      | Entrained mass flow rate   |
| $\dot{m}_{CO_2}$ | Mass flow rate of $CO_2$ in central jet  |
| $\dot{m}_{om}$   | momentum flow rate   |
| $Re$             | Reynolds number  |
| $R_F, R_C, R_D$  | Radii of central jet, centerbody, duct   |
| $R, \theta$      | Cylindrical coordinates for location in the duct                                       |
| $U, V, W$        | Velocity components in the X,Y,Z directions respectively                               |
| $V_R, V_\theta$  | Velocity components in R, $\theta$ directions respectively                             |
| $u, w$           | RMS fluctuation in Y,Z component of the velocity                                       |
| $\bar{W}^F$      | Average of the Z component of velocity for the central jet at the measurement position |

|                      |  |
|----------------------|--|
| $\bar{w}_0^F$        | Average of the centerline velocity, Z component, in the plane being profiled |
| $\bar{w}_{\infty}^F$ | Average centerline velocity, Z component, at the inlet plane                 |
| X,Y,Z                | Cartesian coordinates for the flowfield                                      |
| Z <sub>AS</sub>      | Centerline location of the air stagnation point                              |
| $\phi_{1/2}$         | Diameter of the free jet, full width at half maximum velocity                |



## SECTION 1 INTRODUCTION

This three-part final report documents the research program performed for the Air Force Wright Aeronautical Laboratories, Aero Propulsion Laboratory, by the University of Dayton. The research had two overall objectives: (a) providing profile data that can be used to evaluate combustor and fuel combustion models and (b) evaluating the performance of combustor models and different diagnostic techniques in various combustion environments.

This volume, Part I of the report, documents the design and development of a two-dimensional laser Doppler anemometer and the experimental data collected. The analysis and modeling tasks involving the numerical flowfield predictions and their comparisons with the experimental data are described in Part II. Part III describes the design, development and performance of a two-channel time-resolved laser Raman spectroscopy system.

Study of the fluid dynamics-combustion interaction has become increasingly important in the design of new, high-performance, efficient jet engines. Designing a combustor to meet the performance needs of the engine, while operating on lower grade fuels and generating fewer environmentally harmful products, has become a serious challenge. Programs are now developing numerical computer models which can be used to design and/or analyze combustors. To validate the performance of these models, experimental measurements are required in combustors with well-defined boundaries and controllable inlet parameters.

A program has been underway for several years to produce laser-based diagnostic tools for nonintrusively monitoring the combustion processes in an axisymmetric research bluff-body combustor (see Fig. 1), located at the Aero Propulsion

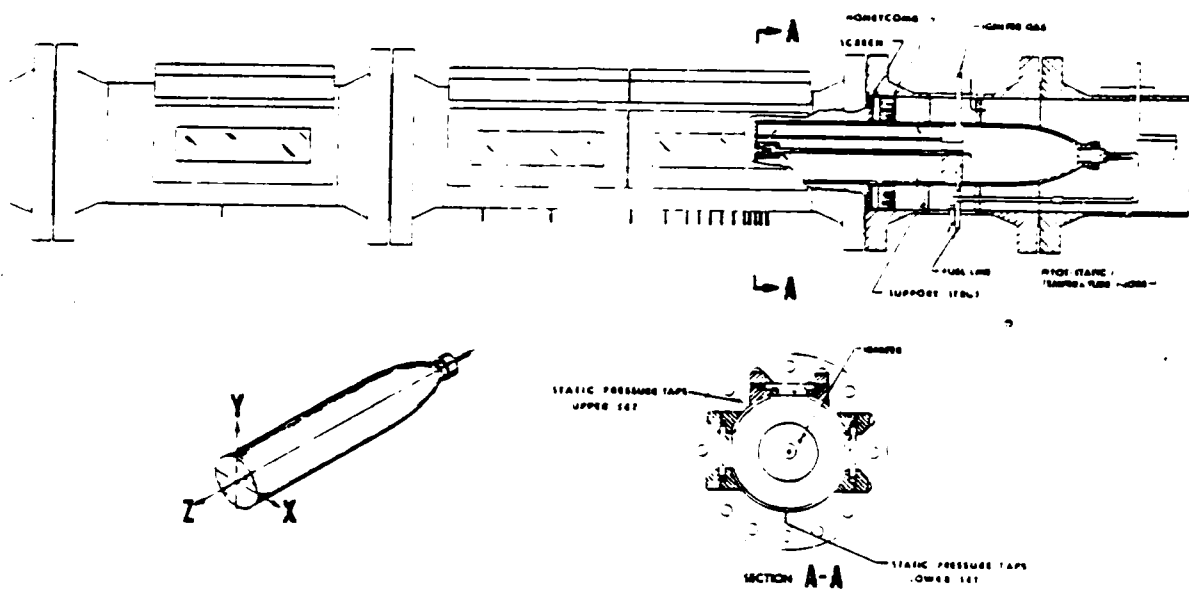


Figure 1. Schematic Diagram of Ducted Coaxial Flow System with Centerbody. The sizes and positions of the various elements are shown to scale. The coordinate system is referenced to the face of the centerbody on centerline and the velocity component in each direction is  $u(X)$ ,  $v(Y)$ , and  $w(Z)$ .

Laboratory, Wright-Patterson Air Force Base. The scope of the program includes the development of instruments for point measurements of the velocity of the flowfield, major species concentrations, and temperature. A goal of the instrumentation is to take data at a sufficiently high data rate to follow the fluctuations in the relevant flow parameters.

Global studies of the environment use schlieren, shadow-graph, and high-speed photography, and are made under the same operating conditions as the point measurements, to gain a system understanding of the fluid processes. Concurrent global and point measurements, as well as conditionally sampled point measurements, will be required in the future to advance our understanding and to provide the details needed for refining the computer models.

This report details the design and operation of the most recent version of the Laser Doppler Anemometer (LDA). The instrument measures two components of velocity and was used to profile the velocity flowfield in the combustor shown in Figure 1. The flowfield entrance geometry is that of coaxial jets with a central fuel jet issuing from the face of a centerbody and annular air entering around the periphery of the centerbody. A recirculation zone is established in the wake of the centerbody which extends about one centerbody diameter downstream, for the flow conditions being reported here (see Fig. 2). The first window station provides optical access from 50 mm upstream to 250 mm downstream of the centerbody face, extending past the end of the recirculation zone. The next optical station begins at 400 mm and extends to 700 mm downstream. Relevant dimensions of the combustor are:

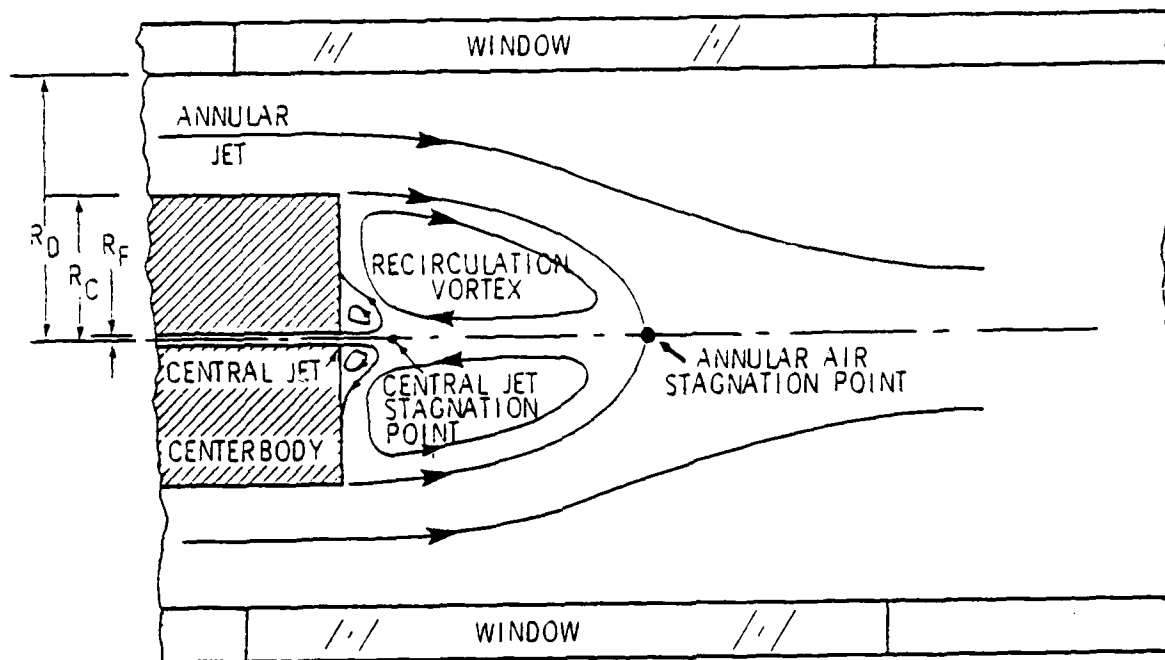


Figure 2. Schematic Diagram of the Anticipated Flow Field. The relevant dimensions are drawn to scale.

Fuel tube radius  $R_F = 2.39$  mm  
 Centerbody radius  $R_C = 70$  mm  
 Duct radius  $R_D = 127$  mm

Studies were made of the flowfield for the system in isothermal flow under three distinct operating conditions specified in Table 1. In the first test case the flow approximates a free jet, since  $R_F \ll R_D$ . The velocity profiles are coupled with concentration measurements, made under the same operating conditions with gas-sampling probes, to provide information on entrainment. The second test set provides the baseline flowfield for investigating the annular jet-central jet interaction and the influences of combustion on the flowfield. The last test set in this series examined the interaction of the two jets and the resulting flowfield.

TABLE 1  
 OPERATING CONDITIONS FOR THE LDA MEASUREMENTS

| TEST SET | FUEL FLOW<br>CO <sub>2</sub> (kg/hr) | ANNULAR FLOW<br>Air (kg/s) | REYNOLDS NUMBER<br>Re ( $\times 10^{-3}$ ) |
|----------|--------------------------------------|----------------------------|--|
| 1        | 2                                    | 0                          | 11   |
|          | 6                                    | 0                          | 32   |
|          | 16                                   | 0                          | 83   |
| 2        | 0                                    | 2                          | 481  |
| 3        | 6                                    | 2                          |  |
|          | 2                                    | 2*                         |  |
|          | 16                                   | 2*                         |  |

(\* centerline only)

## SECTION 2

### LASER DOPPLER ANEMOMETER

During the last decade, Laser Doppler Anemometry has been applied extensively to the study of fluid motion. LDA affords a means of measuring fluid velocity nonintrusively. The temperature of the fluid is rarely a serious concern while optical access to the measurement volume is available. As a result, LDA may be used in combustions flows where other sensors would be destroyed. LDA measurements can be made from a remote position and, if needed, by using a single-ended optical configuration (sender-receiver at the same location). Thus, it is possible to shield the optical system from any harsh environment near the measurement site.

The theory explaining the LDA technique has been presented by many authors (see for example Ref. 1) to whom the reader is referred for details. The most commonly used optical configuration is the dual-beam system, in which two beams of equal intensity are focused and crossed over at some location in space (see Fig. 3). A scatterer passing through that location will scatter light from each beam, each component being Doppler shifted from the original frequency by an amount depending upon the velocity of the scatterer along the direction of the optical beam. Using a square-law detector (e.g., photomultiplier tube) to monitor the scattered light results in a homodyne mixing of the two signals with a measurable beat note being produced (typically DC-30 MHz). The frequency of this signal is directly proportional to the velocity of the scatterer along the direction perpendicular to the bisector of the incident beam directions and in the plane containing them. The geometry shown in Figure 3 has a significant advantage over other geometries used for LDA; the Doppler frequency generated is independent of the position of the detector. As a result, the detector can collect scattered radiation over an extended angle and the signals will add

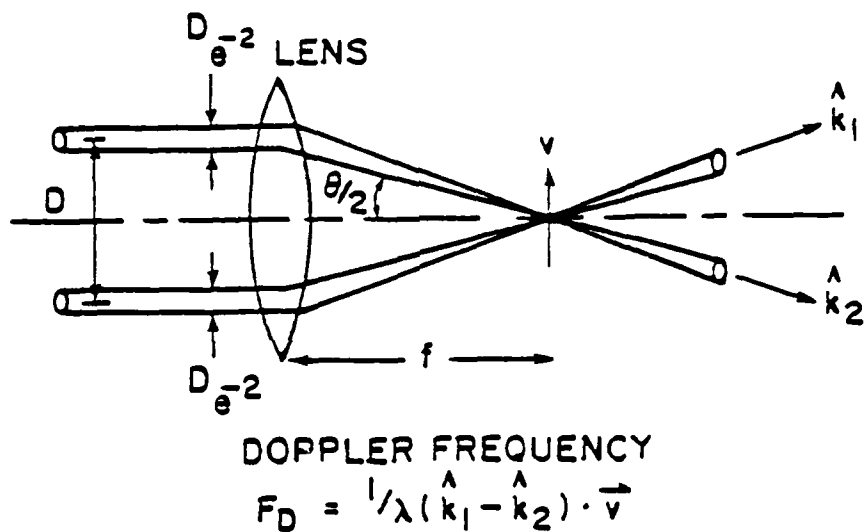


Figure 3. Single-Channel Dual-Scatter Laser Doppler Anemometer Optical Configuration. The Doppler frequency detected in the scattered radiation is independent of the collection angle. The  $\hat{\phantom{x}}$  symbol designates a unit vector.

constructively. The LDA system used in the studies reported here will be described in detail including the design criteria, the electronics for signal handling, the system checkouts, etc. The electronic hardware interfacing the LDA to the computer, the special electronics processing and control circuits designed and built for this system, and the computer software were all reported in depth in the Technical Manual.\*

The LDA system used in these studies is two-dimensional, with a three-beam optical configuration, and using polarization to separate the two orthogonal velocity components measured. The optical system is shown in Figure 4 and has been described in detail by Magill, et al.<sup>2</sup> The system is a composite of two independent channels identical to the channel shown in Figure 3.

The laser source is a 5W Argon-ion laser operated at 488 nm. The maximum laser power is approximately 1W in this single line, more than adequate for these studies. Typically 150 mW of laser power was used in the isothermal studies.

A dry refractory powder is dispersed in the flow system to act as a scattering source for the Doppler signal. The ability of the particle to track the fluid motion depends on several factors including particle diameter, shape, and density. The submicron particles used here were computed<sup>1</sup> to track fluctuations in the fluid flow, at 1 kHz frequency, with better than 99 percent accuracy. For the mixing studies, two seeders were used to seed each fluid independently. The seeders had to be adjusted carefully to match the seeding rates, so that the measurements in the mixing region would not unduly weight the influence of one of the fluids over the other.

---

\* Andrews, R. J., A. J. Lightman, and P. D. Magill, "Operation and Maintenance Manual for a Two-Dimensional Laser Doppler Anemometer," UDR-TR-82-152 (1982).



# LEGEND

1. POLARIZATION ROTATOR
2. SPATIAL FILTER AND BEAM EXPANDER
3. HALF-WAVE PLATES
4. BEAMSPLITTER
5. COMPENSATOR
6. BRAGG CELL MODULATOR
7. BEAM-STEERING PRISMS
8. POLARIZER
9. BEAM STOP
10. GLAN-THOMPSON POLARIZATION BEAMSPLITTER
- Li LENS
- Di PHOTOMULTIPLIER TUBE
- FO FIBER OPTIC
- M MIRROR

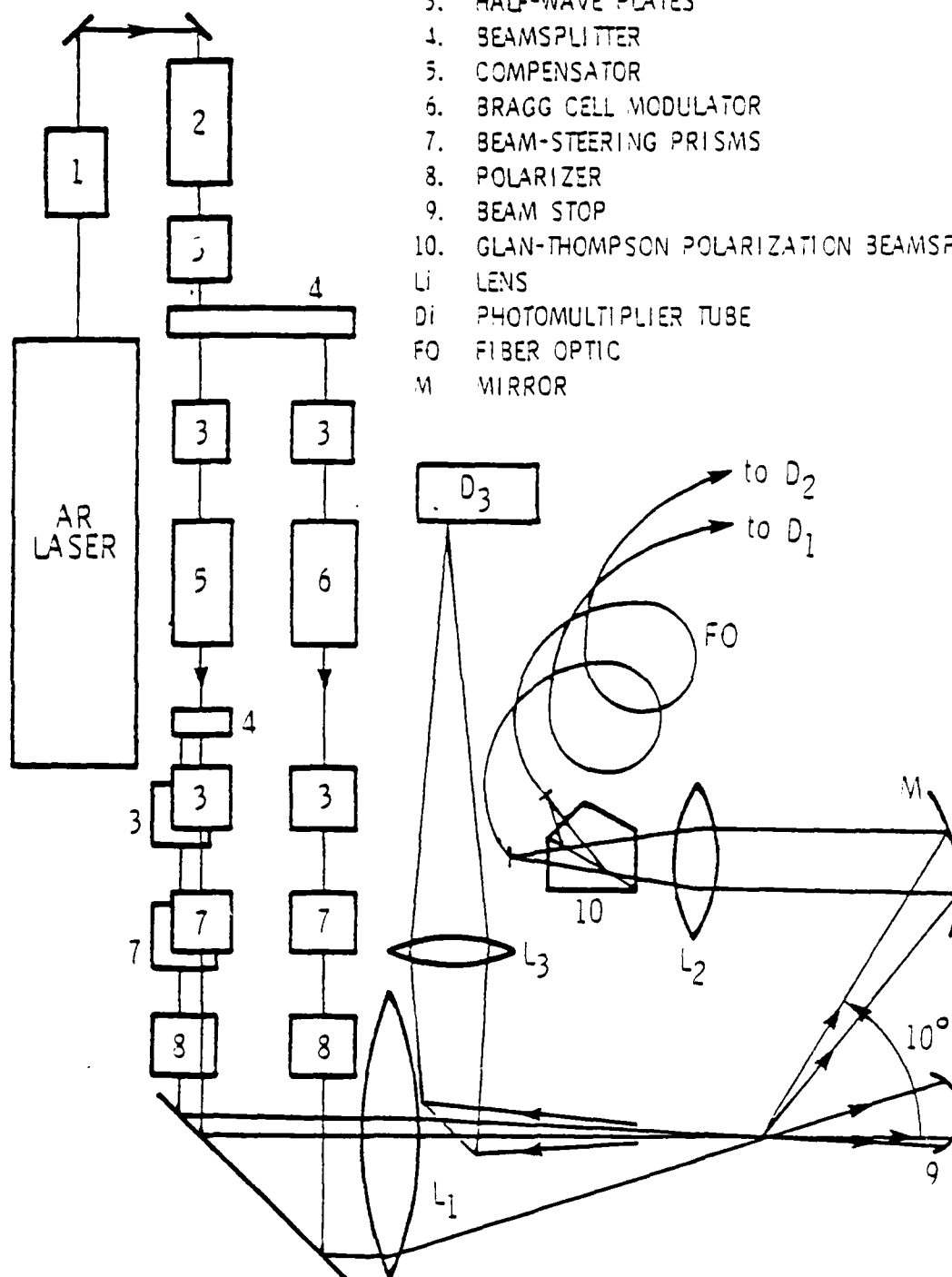


Figure 4. Two-Dimensional LDA Optical System Using Polarization to Differentiate the Orthogonal Velocity Components. The luminosity monitor is also shown (D<sub>3</sub>).

The scattered signal was collected at  $10^\circ$  from the forward direction. The available windows (300 mm x 76 mm) on the flow system limit the detection region to near the LDA optic axis when scans are made in the flowfield, so that shadowing does not degrade the signal so much that it becomes unusable. Forward scatter was chosen because it maintains the polarization signature needed to distinguish the velocity components and it provides greater signal strength. The most common difficulty with using polarization discrimination is crosstalk between the channels, depolarized scattering from one channel being received by the other channel. In tests using one channel of the LDA system alone, no crosstalk measurements were observed in the other channel.

Two reasons motivated the selection of polarization discrimination for the LDA. First, the optical system is more straightforward and easier to harden for use in the high acoustic level and large temperature-gradient environment where the LDA operated. Second, it was understood at the beginning of the program that 3-D LDA measurements would be required eventually. Using polarization for 2-D LDA made the other strong Argon laser line available for use in obtaining the third velocity component. Employing color separation for all components necessitates using either a weaker laser line for the third component, usually the line at 476.5 nm or 496.5 nm,<sup>3</sup> or a frequency-mixing scheme having degraded velocity resolution.<sup>4</sup> Results of research using this technique have not demonstrated any great degree of success.

The three-beam configuration produces two orthogonal LDA systems. The beams, all parallel to the optic axis, pass through the crossing lens at the locations shown in Figure 5(a) with the polarizations shown. The three beams cross on the optic axis at the focus of the lens. Placing a target at the crossing location produces the orthogonal fringe system shown in Figure 5(b), both sets of fringes at  $45^\circ$  to the optic axis. The U and L beams are orthogonally polarized and do not interfere. A photograph of

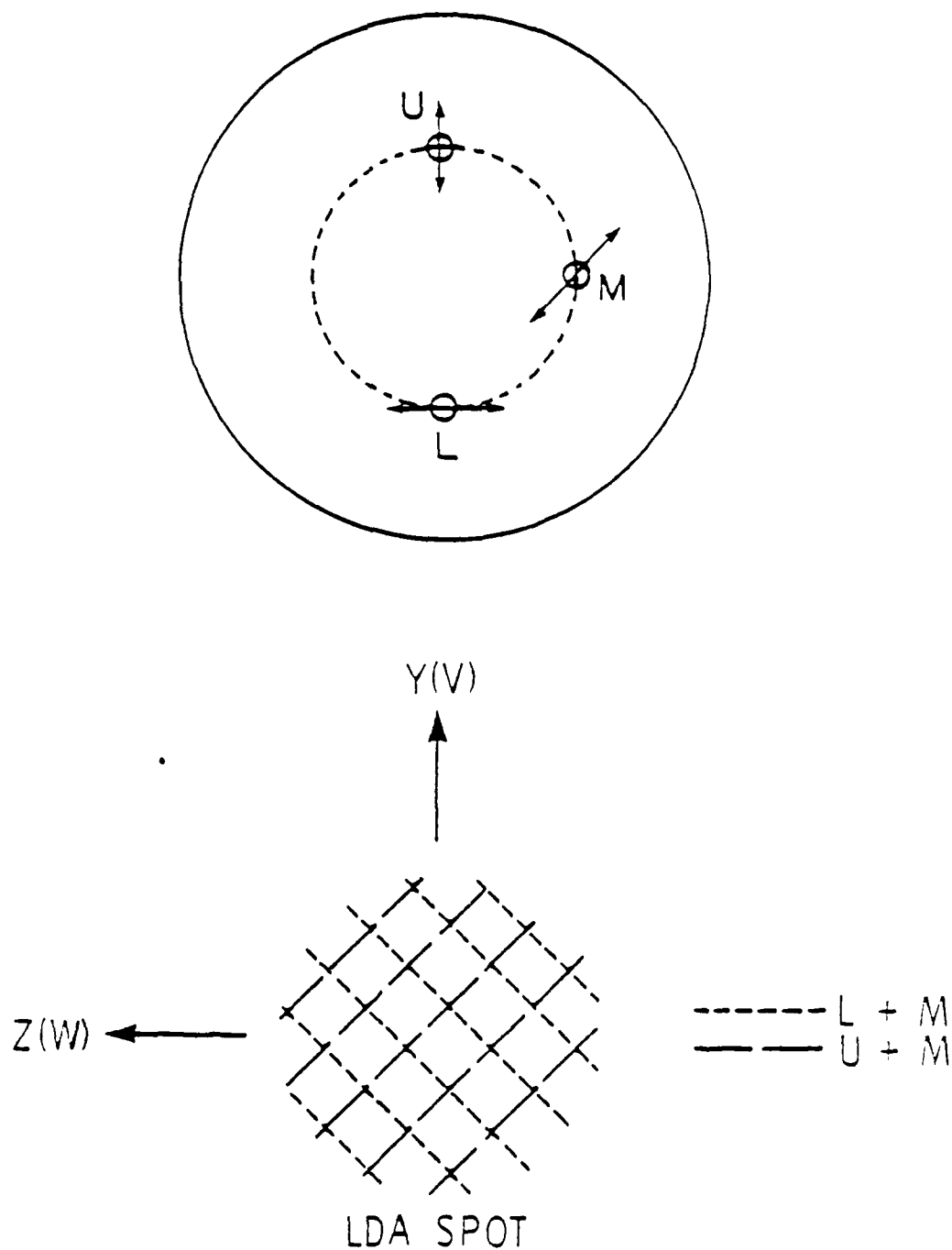


Figure 5. (a) Positions and Polarizations of the Three Optical Beams at the Focusing Lens; (b) Fringe Pattern Observed at LDA Focused Spot. Tunnel reference coordinates are also shown.

the fringe system is shown in Figure 6. In normal use, the fringe spacing is measured using the graticule that can be seen in Figure 6, rather than relying on computed parameters. For the optical system used--lens focal length 711 mm, laser wavelength 488 nm, three beams on a 50-mm diameter circle--the measured fringe spacing was  $10 \pm 0.1 \mu\text{m}$ .

The M beam, the optical beam common to both LDA systems, is frequency shifted by an acousto-optic modulator to produce a frequency offset that eliminates directional ambiguity. The Bragg cell operates at 40 MHz, permitting measurements of Doppler shifts of 30 MHz before interferences occur with the next laser mode at higher frequency, or with the laser discharge noise at lower frequency. The Doppler frequency range of 30 MHz corresponds to a velocity range of 300 m/s in the direction of measurement. This adequately covers the expected velocities with a sufficient safety margin.

## 2.1 OPTICAL DESIGN CRITERIA

The optical system had to be designed around the physical limits of the combustor. The combustor duct has a 254 mm inside-diameter and the LDA system had to scan across it. The closest optics on either side of the combustor, the sending and receiving optics, had to be separated by at least 1000 mm so that they would both be clear of the duct flanges at either extreme of the scan. Thus the sending and receiving optics had to have focal lengths of at least 500 mm for the optical design shown.

The LDA spot-size diameter was set according to the velocity resolution desired and the expected velocity range. To obtain 0.5% accuracy in measuring the Doppler period, it was necessary to measure the period for 32 cycles (at the higher velocities the lower signal-to-noise ratio limited the gating accuracy to about 1/6 fringe). The highest expected velocity was 300 m/s at the exit of the fuel tube. For a 10- $\mu\text{m}$  spacing fringe system this would provide a 30-MHz Doppler shift. By selecting the correct

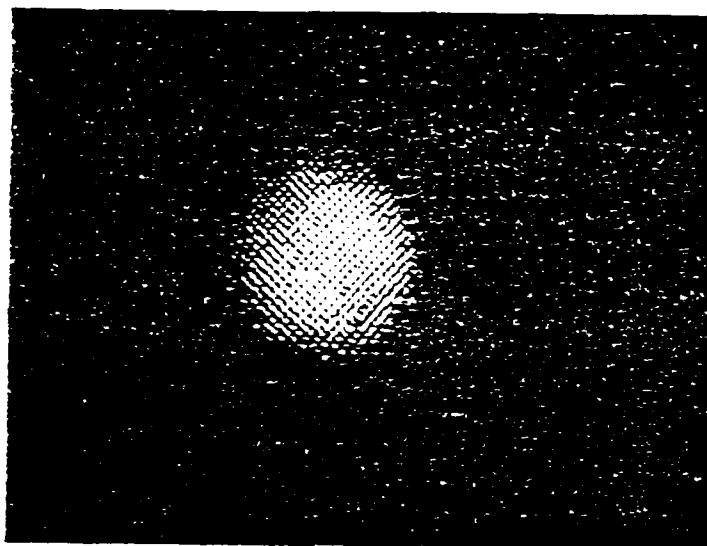


Figure 6. Photograph of Fringe Pattern Observed on a scattering Screen in the LDA Spot. The graticule, aligned with one of the fringe systems, has minor ruling spacing of 10  $\mu$ m.

Bragg cell mode of operation, the resulting measured frequency would be 70 MHz (shifting in the reverse direction results in a 10-MHz signal and a commensurate degradation in optical spatial resolution). For 32 Doppler cycles to be collected (70 MHz signal), the scatter must reside in the LDA spot for at least 0.45  $\mu$ s; thus the minimum spot diameter would be 135  $\mu$ m. In fact, it must be considerably larger. For the fringe system as shown at  $\pm 45^\circ$ , the minimum diameter is 160  $\mu$ m. If the fringe system were rotated  $45^\circ$  (to align with the Y and Z reference axis), the minimum diameter would increase to 240  $\mu$ m, dictated by the zero velocity in the Y direction. To increase the crossing region from which acceptable signals could be collected, it was decided to increase the spot dimension from the 160  $\mu$ m minimum size. The final choice was an engineering selection, determined by the availability of an off-the-shelf lens having near diffraction-limited performance. The LDA spot diameter used was 300  $\mu$ m and the lens had a focal length of 711 mm.

Several key parameters describe the LDA spot which will be used in this discussion. For conciseness they are listed here (refer to Fig. 3):

$$\text{Spot diameter} \quad d_m = (4 \lambda / \pi) f / D_e^2 \quad (1)$$

$$\text{Spot length} \quad l_m = d_m / \tan \theta / 2 \quad (2)$$

$$\text{Fringe spacing} \quad d_f = \lambda / 2 \sin \theta / 2 \quad (3)$$

The size of the laser beam was adjusted by selecting the collimating lens of the spatial filter-beam expander (#2, Fig. 4). It was chosen so as to pass through the 5-mm aperture of the Bragg cell without creating any interference fringes in the LDA spot. A diameter of  $\sim 1.5$  mm satisfied this requirement. The beam remained close to this diameter to the focussing lens. Using Eq. (1), this yielded a spot diameter of 294  $\mu$ m in agreement with the measured value. The fringe spacing from Eq. (3) is 9.82  $\mu$ m, marginally less than was measured. This probably results from the crossing point being slightly displaced

from the exact focal length. The length of the spot, from Eq. (2), computes to 11.8 mm. The parabolic mirror, M in Figure 4, is centered  $10^\circ$  off-axis. If the scattered light collected is limited to a small region around  $10^\circ$ , the spot length would be determined by the projection of the 200- $\mu$ m-diameter optical fiber through the crossing length (adjusted for the 50- $\mu$ m blur circle of the mirror). The collected spot length would be 1.44 mm. In fact the mirror's collection angle extends from  $3.3^\circ$  to  $16^\circ$  and the length of the LDA spot, which had to be measured experimentally, is 3 mm (see Fig. 7).

## 2.2 ELECTRONIC SYSTEM

The scattered radiation is transferred via an optical fiber<sup>5</sup> from the test cell to the control room 30 m distant. The optical fiber is immune to electrical noise and its bandwidth exceeds the requirements of the optical signals. The fiber overcomes difficulties with coaxial cables, such as high-frequency attenuation and spurious signal pickup. The signal is brought up to two matched photomultipliers and from there to two modified signal processor units through preamplifiers (see Fig. 8). CP<sub>1</sub> computes the Doppler period for a preset number of cycles, with or without comparison, as selected (see TSI 1990A manual) and also counts the number of Doppler cycles in the burst (N-cycle) to a maximum of  $2^{12}-1$ . (Standard 1990A's are limited to  $2^8-1$  cycles and could overflow once velocities dropped below 47 m/s in this system, losing the residence time information.) CP<sub>2</sub> computes the Doppler period only. Both processors signal that data are ready on their data bus at the end of the complete Doppler burst. If the data rate is too high at the location of interest, the processors can be limited in their data acceptance rate (unlimited, 30,000, 10,000, 3,000, 1,000, 300, 100 per second), using a specialized control circuit designed and constructed by the University of Dayton. Another detector monitors the

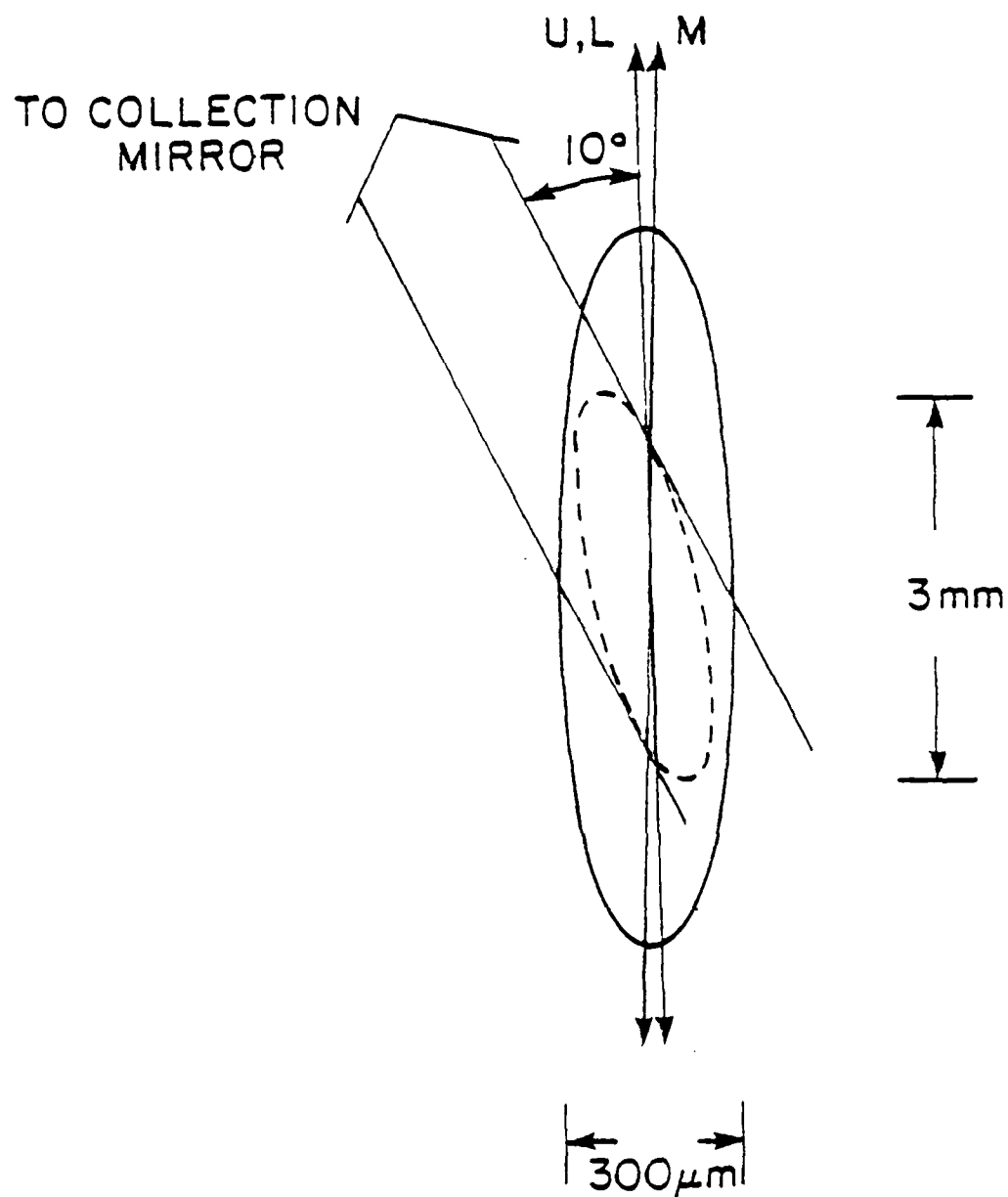


Figure 7. LDA Spot and Collection Volume Observed by Off-Axis Paraboloid.



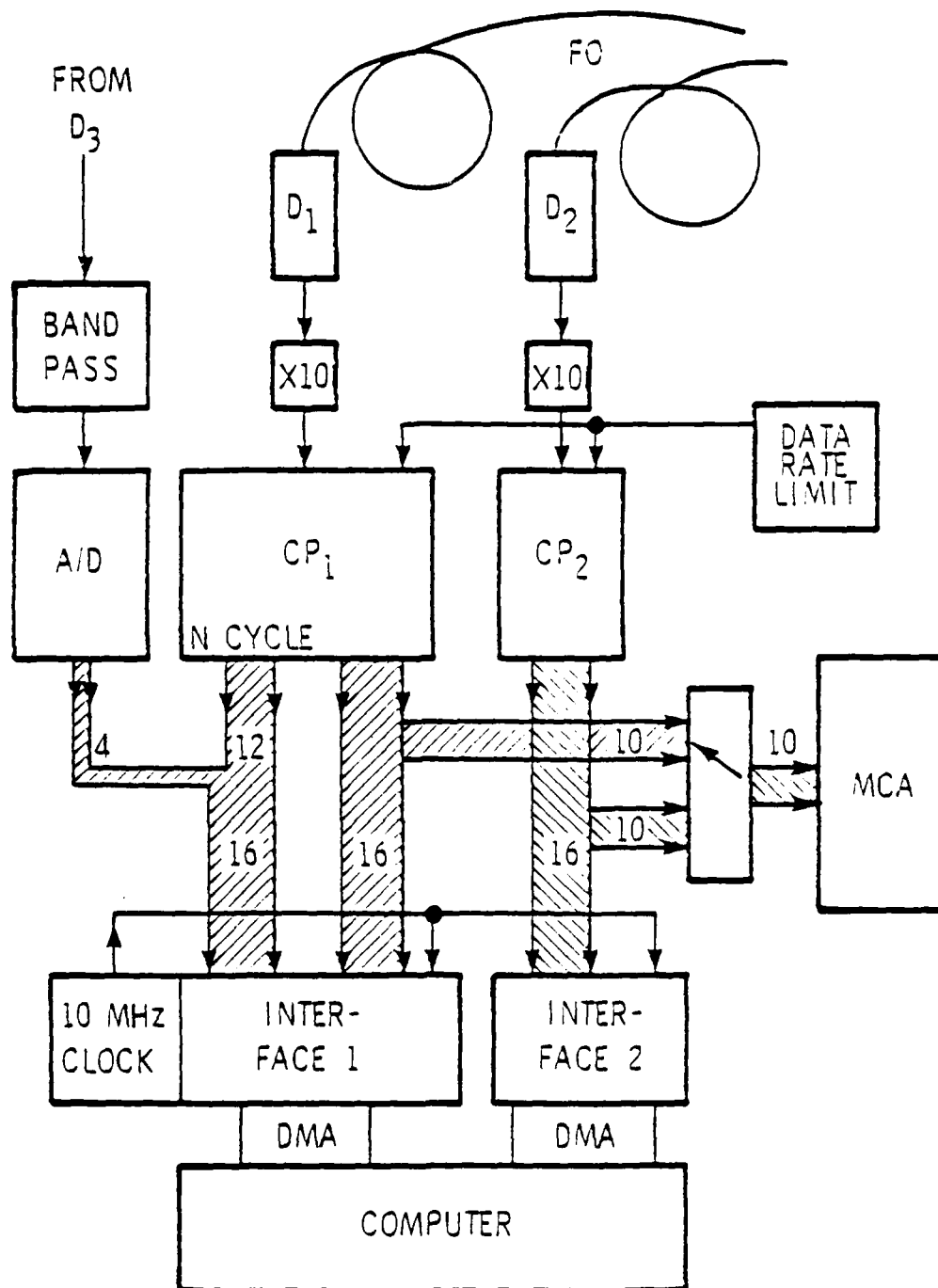


Figure 3. Electronic System Processing the LCA Signal. System shows how data are transformed from optical signal to computer words.

luminescence along the line of the anemometer's optical axis (used in combustion studies only). This signal is processed by a band-pass filter and digitized. The digital data are packed together with the N-cycle data, 4 bits luminosity, plus 12 bits N-cycle data in the 16-bit word fed to the computer.

A 10-MHz clock measures the interarrival time of the signals on each channel (Figures 8 and 9). As configured, the clock has a 12-bit resolution and a 27-bit dynamic range, permitting measurements to 409.5  $\mu$ s at full resolution and to 13.42 s at reduced resolution. Figure 9 shows the digital data flow on Channel 1, where three 16-bit data words are transferred to a fast buffer memory and by direct memory access (DMA) to the computer memory. Channel 2 transfers the elapsed time and the Doppler period only. The DMA unit on each channel can process 400k 16-bit words/s, permitting a long-term data collection rate of 130k data points/s, limited by Channel 1. The fast FIFO memory permits storage of a limited number of data-points when they arrive faster than the DMA can process them (it can accommodate the fastest rate of the counter-processor).

### 2.3 DATA COLLECTION

The sheer volume of data produced by the LDA system necessitated the development of extensive interactive software packages to collect and analyze the data. This system will be reviewed in the following paragraphs.

The LDA data are collected by a MODCOMP minicomputer. The internal architecture of this computer restricted the data to one page of memory, limiting the maximum number of data realizations to about 5,000 per data point. Typically, this provides sufficient data in the  $v, w$  coordinate frame to ensure the stability of the computed moments of the distribution (the velocity components  $u, v, w$  align in the  $X, Y, Z$  directions respectively). Once the data are collected in memory, they are converted from TSI- and UDRI-packed\* integer formats into real (floating-point)

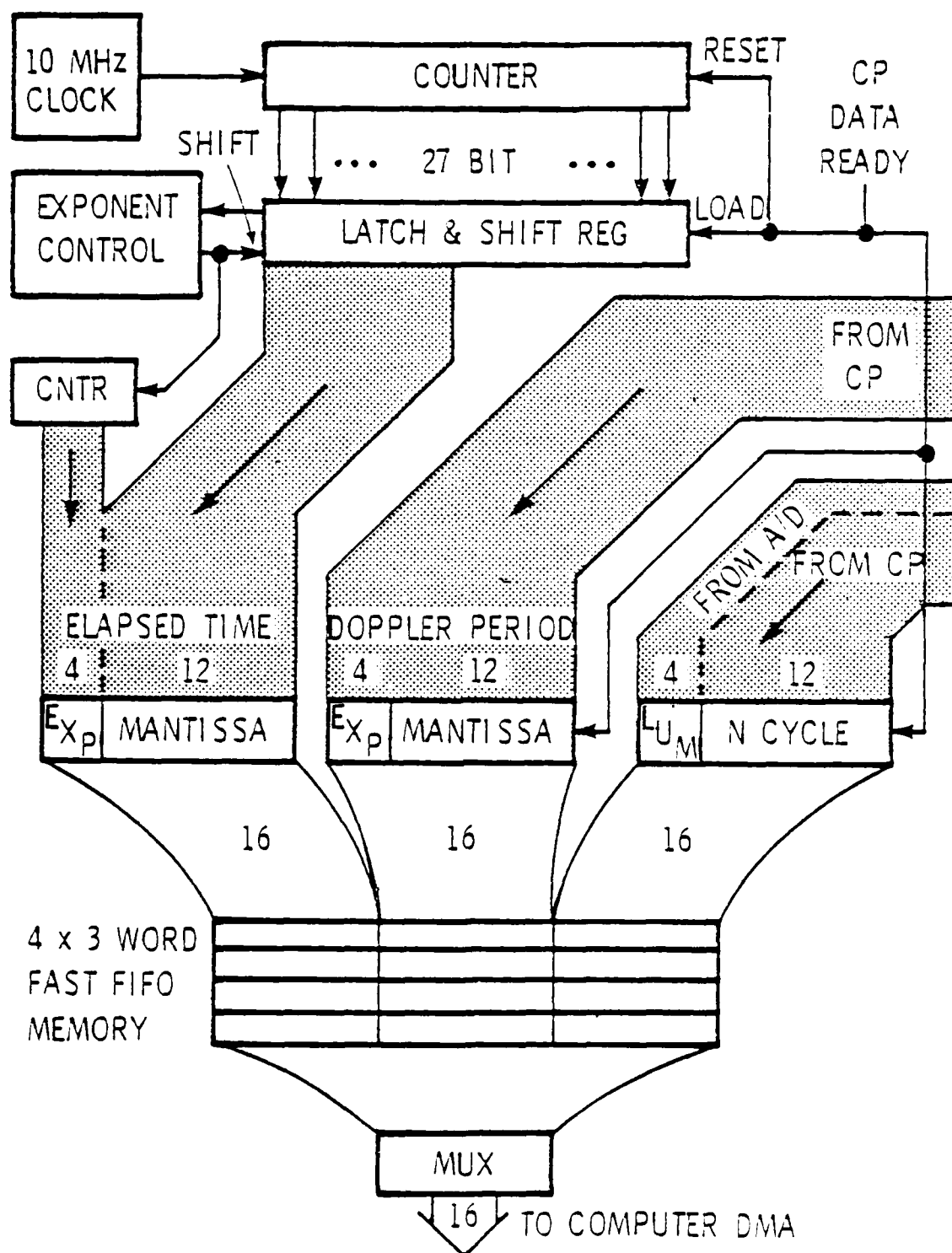


Figure 9. One Channel of the LDA Computer Interface. The FIFO memory is multiplexed through a direct memory access (DMA) controller. The inter-arrival timer is also shown.

numbers. The data are filtered, analyzed, reformatted, and put onto disk memory. A summary of the data (mean velocities, standard deviations, data rates, etc.) is presented to the operator on the computer console. In addition, a visual display of the velocity histograms and a summary of the run conditions and results are plotted on a Tektronix graphics terminal (see Fig. 10). If the data are to be retained, a hard copy is made of this display to be kept for reference. The average velocities are transformed to the v and w directions and are passed to another computer program which retains all data sent to it and can plot velocity profiles as the data are collected (see Fig. 11).

When the on-line data collection is terminated, the data storage disk is transferred to another MODCOMP computer, referred to as the HOST computer. The data are further filtered, and pointers are attached to the velocities to align the measurements of the velocity, in each direction, that occurred at the same instant. (The two channels operate independently and not all velocity realizations on one channel necessarily yield corresponding realizations on the other channel.) The data are then reformatted for more efficient use of magnetic tape and stored on an archival-data-record magnetic-tape set.

## 2.4 DATA PROCESSING

Analyzing the data obtained by LDA measurements is a subject for active discussion by researchers in the field. In

---

\* To speed data transfer, the information has been restructured into special formats that occupy less than half the number of bytes that data would occupy as individual, floating-point numbers.

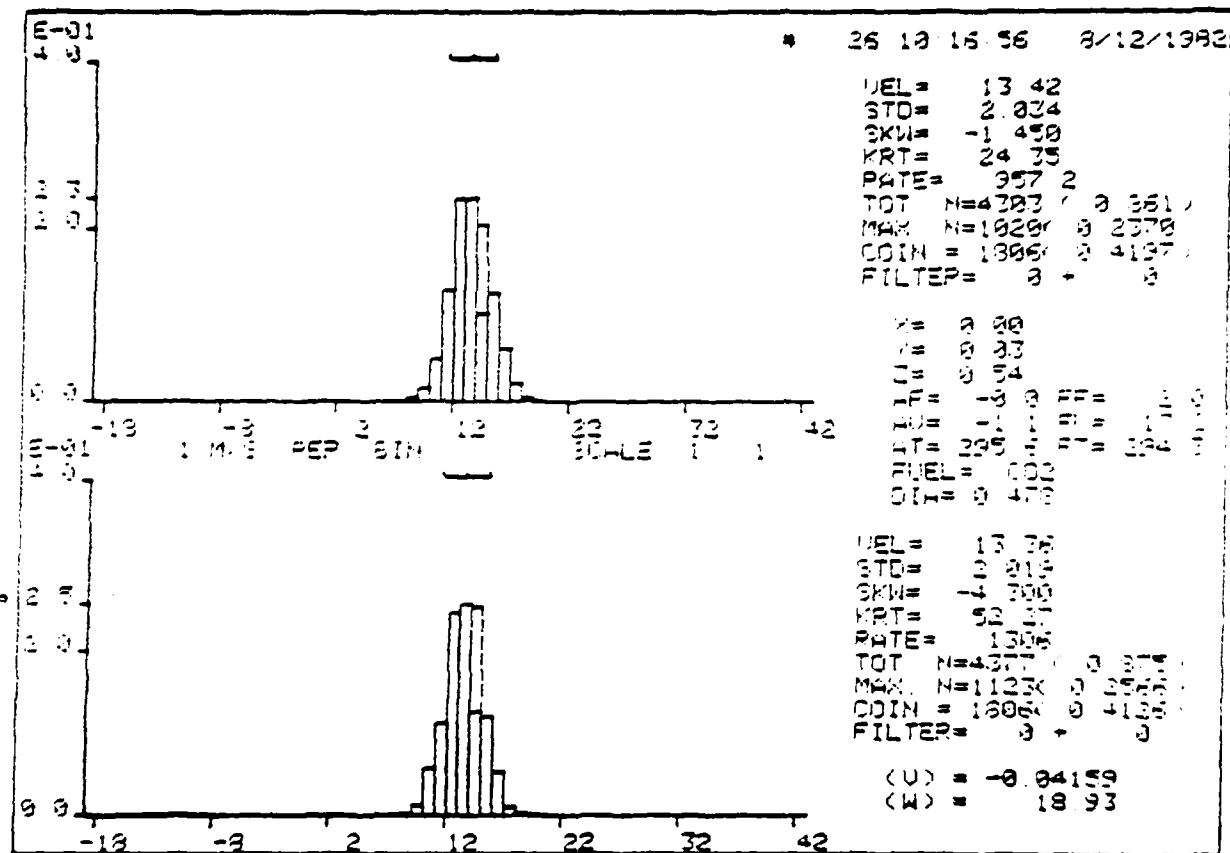
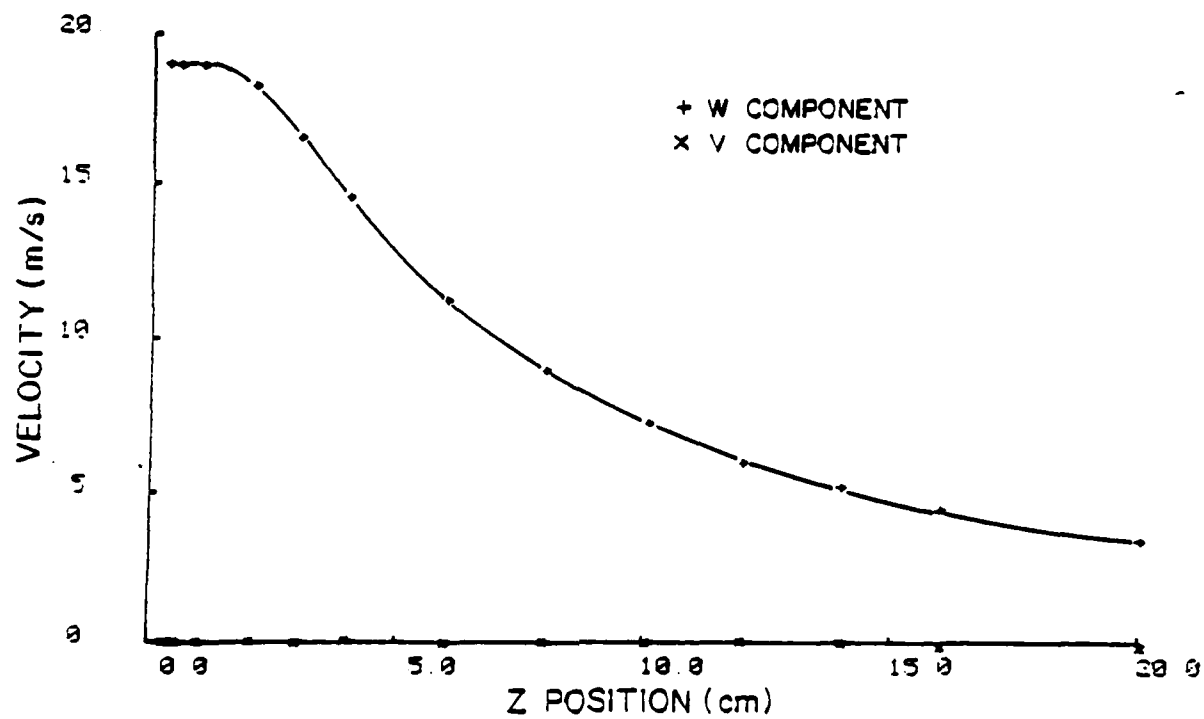


Figure 10. Computer Summary of On-Line LDA Data Analysis. Histograms and summary of the data are produced. The dotted extension to the histogram is a correction due to the velocity bin 14-15 m/s containing half as many period channels as the other bins shown.



AXIAL PROFILE FF=2 8/12/82

Figure 11. On-Line Computer Plot of Profile Data. Shown here is a centerline velocity profile of the central jet (2 kg/hr CO<sub>2</sub>, ASME nozzle). The transformed average axial and radial velocity components are plotted.

high-volume gas flow systems, the LDA data arrive randomly. Counter-processors interpret the Doppler signals and their output, which is discrete in time, and is valid only during the time of measurement. Using these measurements to infer the properties of the continuous flowfield, may result in biased values. To date, a variety of methods have been proposed and applied to correct biases in the data reduction schemes, but the underlying assumptions of these methods are not usually tested in the experiment. McLaughlin and Tiederman<sup>6</sup> discussed a velocity-biasing effect in measurements of flows that are uniformly seeded. Hoesel and Rodi<sup>7</sup> considered the situation where the seeding is sufficiently dense that the LDA measurements occur rapidly enough to follow the flow accurately.

Hoesel and Rodi<sup>7</sup> and Buchhave, et al.<sup>8</sup> considered corrections needed when the time between realizations was longer than the correlation length in the flow. Edwards<sup>9</sup> pointed out the need to measure the integral scale length at every location to ensure that the averages presented are indicative of the true mean flow and not just local. In addition, the data reduction and interpretation are further complicated when the turbulent flow has a time-dependent mean value.

The data processing programs written for the LDA system incorporate the aforementioned correctors with others of our own design, computing the mean value, standard deviation, skewness, and kurtosis. The processing schemes include: straight arithmetic processing; using a McLaughlin-Tiederman<sup>6</sup> bias corrector algorithm; trapezoidal integration of the velocity time history; weighting the data by residence time (Hoesel-Rodi,<sup>7</sup> Buchhave<sup>8</sup>); simulating processor-limited data collection (supposedly resulting in truly random selection of the data);<sup>10</sup> and other schemes to reduce the possibility of overemphasizing higher velocity measurements. Data arrival statistics are checked to see if the flow is uniformly seeded. A test is made of the McLaughlin-Tiederman assumption by analyzing the velocity-interarrival-time product statistics.

The processed data for each measurement are stored on a summary computer disk (see the Technical Manual for a complete listing) for ease when searching. At present the results of all these data reduction schemes are retained; our studies have not conclusively validated any one method. Data for the results shown in this report have been obtained using the arithmetic averaging scheme.

## 2.5 SEEDERS

Controlled seeding of fluid flow for LDA measurements is difficult. Many researchers have reported seeders which operate well in their restricted environment, but the requirements of this flow system have proven too demanding for these seeders. The large size of the tunnel which needs to be seeded uniformly across the duct, the large volume of air and seed, and the sustained operation for long periods combine to make demands beyond the capabilities of most seeders. In addition, the flow system has a coaxial configuration in which the two separate fluids, central jet and annular jet, must be seeded to the same concentration for unbiased LDA measurements.

A commercial seeder (TSI model 3400) has been modified for use with propane as well as other gases, and our operating procedure allows steady operation for long periods. This procedure includes regularly overhauling the unit, using only carefully prepared seed (baked dry, ground, and sifted), and regular replacement of the fluidized bed media. In addition, the delivery line has been designed to supply the seed within the fuel line, away from walls. Even with this care, the range of operation of the unit is limited.

Seeding the annular flow, which can exceed 2 kg/s, is more difficult. The seeder must put out  $10^3$  times as much seed per time interval to balance the seeding densities in the annular and central flows. A high-volume, fluidized bed seeder that uses a cyclone separator to remove larger agglomerates has been built,

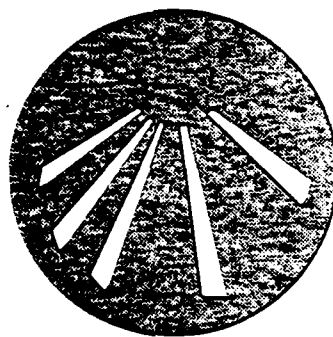
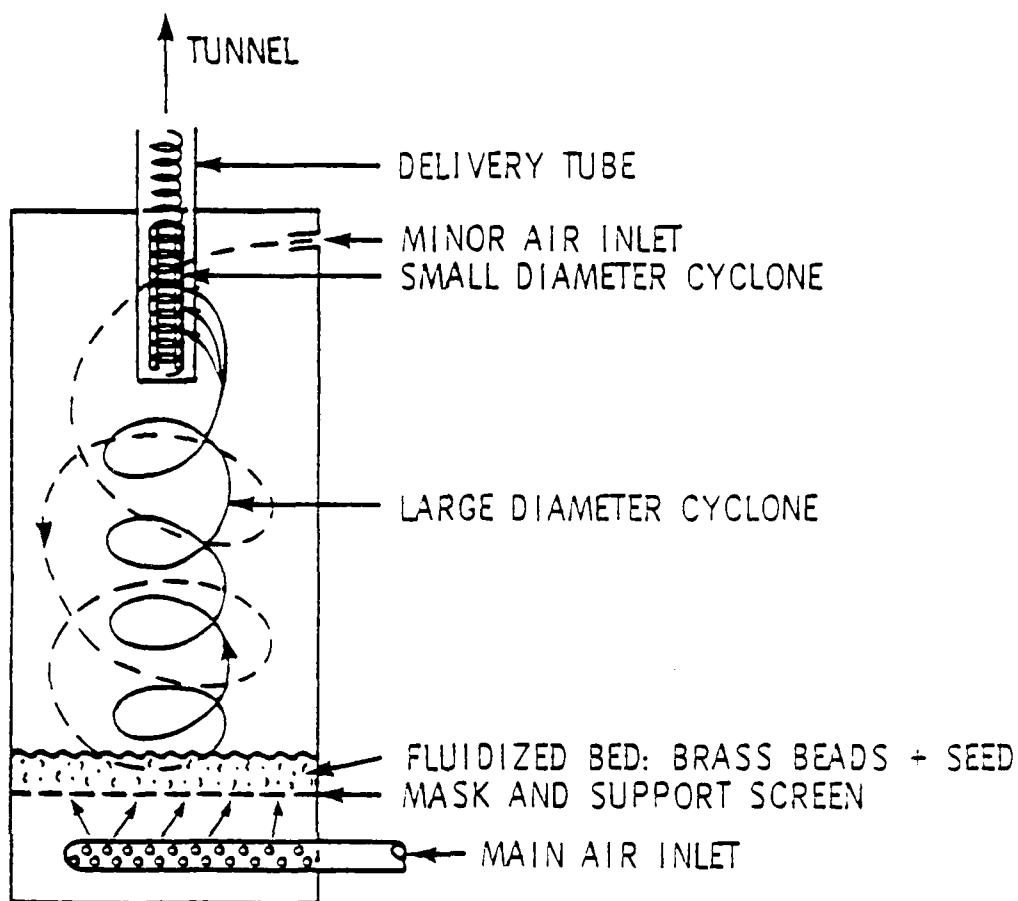


as shown in Figure 12(a). When operated with a solenoid valve on the air supply to provide an air hammer stirring effect, this seeder produces sufficient seed to balance the two fluids. To ensure a uniform repeatable cyclone action, the fluidized bed is supported on a wire mesh above the air inlet. An unbalanced passage mask, shown in Figure 12(b), forces the cyclone action which removes the larger particles. Another smaller diameter cyclone, at the exit port, is used to sift the seed further. Then the seed particles are dispersed into the upstream flow in the combustor duct via a dual-slotted delivery tube, each slot covers 80 percent of the duct diameter. The small seeder emits  $3 \times 10^5$  seed particles per second in continuous operation, and the large seeder emits  $4 \times 10^8$  particles per second in pulsed operation.

Three types of seed material have been tested in the LDA system:  $\text{TiO}_2$  with a flow agent,  $\text{Al}_2\text{O}_3$  (alpha) with a flow agent, and  $\text{Al}_2\text{O}_3$  (gamma). The nominal diameters of the seed particles are respectively  $0.2 \mu\text{m}$ ,  $0.3 \mu\text{m}$ , and  $0.05 \mu\text{m}$ . It was determined that the  $\text{TiO}_2$  seed was best for combustor studies, the gamma-alumina worked best in cold flow, and the alpha-alumina seed made the largest contribution to depolarized scattering, probably as a result of its jagged shape. As mentioned earlier, Durst<sup>1</sup> has shown that  $1.3 \mu\text{m}$  diameter  $\text{TiO}_2$  can follow 1 kHz fluctuations in air with 99 percent accuracy, and  $0.4\text{-}\mu\text{m}$ -diameter particles track 10-kHz fluctuations, also with 99 percent accuracy. Thus, even if the  $\text{TiO}_2$  has agglomerated somewhat, it should not exceed a size which would distort the turbulent energy spectrum, beyond the measurement uncertainties, in the frequency range of interest (1 to 5 kHz maximum). All the seed materials should provide accurate spectra over the entire frequency band of interest.

## 2.6 LDA SYSTEM CHECK--LABORATORY

The LDA system was tested in the laboratory prior to being moved into the tunnel. The first parameter validated was the



FLUIDIZED BED MASK

Figure 12. (a) Large Seeder Built to Seed the Annular Jet. A fluidized bed and two cyclone separators are used to produce an output of suitable seed particles. (b) Bed Mask Used to Ensure Cyclone Action of Flowing Gas.

spot diameter (the visual checks using a microscope objective to enlarge the spot are inaccurate). A chopper run by a synchronous motor was mounted on a traversing table and inserted in the optical system near the focal position. The chopped beam was picked up by a solid-state detector (having an appropriate bandwidth) and displayed on an oscilloscope. As the chopper blade passes through the beam, the signal will go from off to on (or vice versa) with a time characteristic that depends upon the laser mode. For a TEM<sub>00</sub> mode and a chopper blade that linearly traverses the laser beam, the following relations are valid:

$$\text{Laser Intensity Profile} \quad I(r) = I_0 \left( \frac{1}{2} \right) e^{-\frac{1}{2} \left( \frac{r}{a} \right)^2} \quad (4)$$

$$\text{Collected Intensity} \quad I_c(t) = I_0 F(vt/a) \quad (5)$$

where  $I_0$  is the laser beam intensity,

$F(x)$  is the error function,

$v$  is the linear velocity of the chopper as it passes through the optical beam,

$a$  is the beam dimension,<sup>11</sup>

and  $t$  is the time, referenced to  $t=0$  when the chopper blade is at the center of the beam.

Using tabulated values of the error function the 10% to 90% transition of the transmitted intensity will occur in a distance of 2.56  $a$ . The chopper was scanned along the optic axis and the minimum rise time of the transmitted beam (Figure 13a) corresponds to

$$a = 76 \text{ } \mu\text{m} \pm 4.5\%$$

The commonly accepted definition of the LDA spot diameter is the diameter of the  $e^{-2}$  contour. This would correspond to

$$d_m = 4a = 304 \text{ } \mu\text{m} \pm 4.5\%$$

as designed. By traversing the chopper along the optic axis, the beam separation and hence the overlap could be computed from the

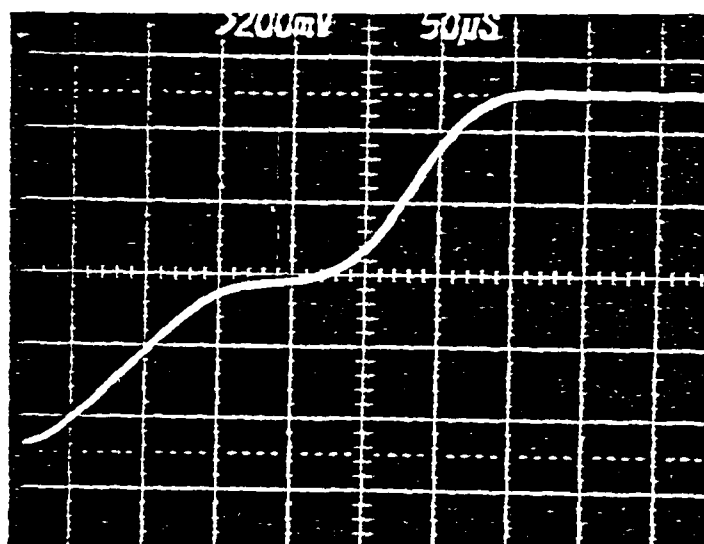
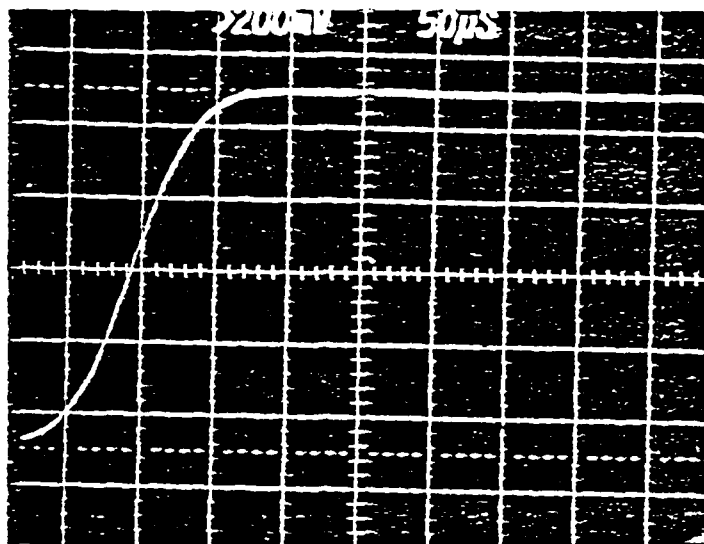


Figure 13. Collected Light as Chopper Passes Through LDA Spot. (a) Chopper at Center of LDA Spot. (b) Chopper Displaced from Center Location. Three beams are present but the U and L beams and the chopper blade are aligned when the chopper passes through so the resulting trace shows a single rise to a height representing the sum of the intensities.

observed oscilloscope traces (Figure 13b). All the computed parameters matched the design.

Next, the LDA signal was examined using a scattering source. The Bragg cell had to be turned off to allow examination of the profile and the Doppler burst together. Typical signals are shown in Figures 14(a) and (b). The signals have the textbook shape and quality, showing 50% visibility. In actual operation, the signal-to-noise ratio obtainable is much less than for these signals. The Bragg cell is needed and the bandwidth of the processor must be expanded to encompass the expected velocity fluctuations. The much higher frequency results in a decrease in the signal in direct proportion to the frequency, as a result of the fewer scattered photons collected per Doppler cycle. The expected signal-to-noise ratio should vary as

$$\text{SNR} \propto (f_0 \Delta f)^{-1/2}$$

where  $f_0$  is the Doppler frequency  
and  $\Delta f$  is the amplifier bandwidth.

Scaling the SNR observed in Figure 14 to typical operating conditions will result in a minimum degradation in SNR of 15 to 20 dB (usually more, since the signal shown was obtained at the center of the LDA spot, the optimum location). Studying the normally obtained LDA signal with a spectrum analyzer showed that under standard operating conditions the processors operated on signals with SNR of 10 to 20 db, sufficient for reliable processing.

## 2.7 LDA SYSTEM CHECK--TUNNEL

The LDA system was tested in the combustion tunnel before being used for experimental study. Due to time limitations a simple, straightforward test was desired. The simplest test was to measure the fuel exit velocity at various flow rates and to compare the measurements with (a) that expected from a simple, flat-top profile and with (b) that predicted by a computation

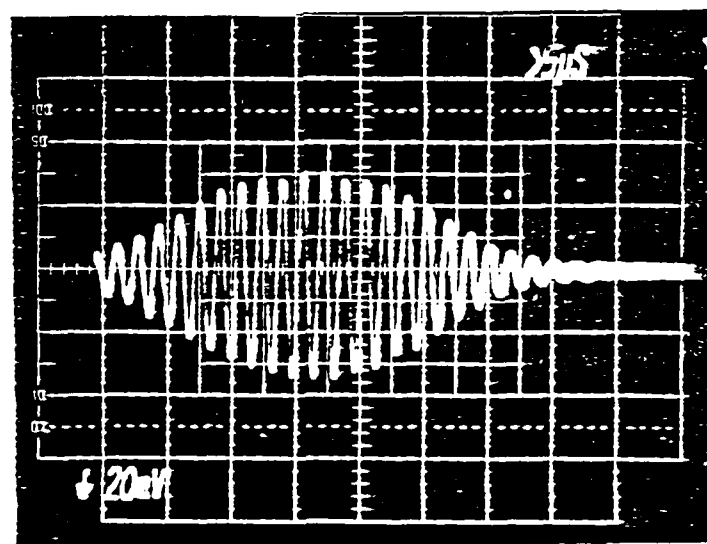
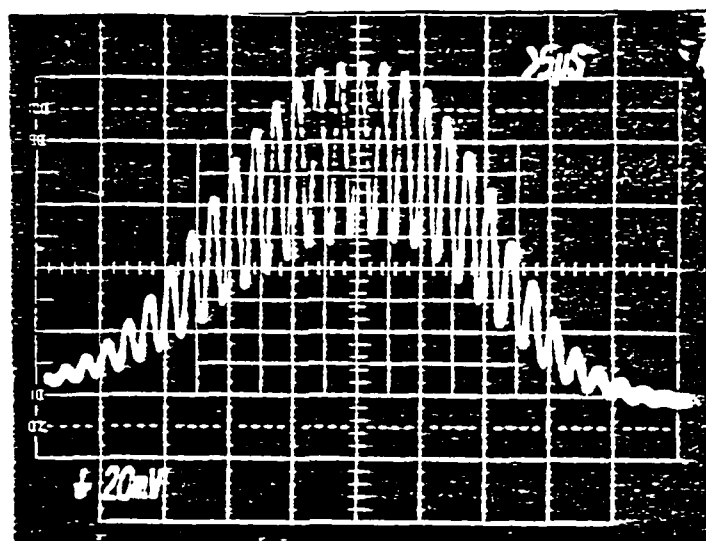


Figure 14. Typical LDA Burst Observed with Bragg Cell Switched Off. (a)  $F_{\text{flipper}} = 2 \text{ MHz}$  and  $F_{\text{flower}} = \text{DC}$  so the pedestal can be seen. (b)  $F_{\text{flipper}} = 2 \text{ MHz}$  and  $F_{\text{flower}} = 0.1 \text{ MHz}$ .

that took temperature and compressibility into account. The fuel flow was increased in an attempt to reach choked flow, limited by the fuel nozzle. The results of the LDA measurements and the two predictions are shown in Figure 15. In the region  $M < 0.5$ , all three are in excellent agreement. When  $0.5 < M < 0.67$  the LDA and corrected predictions agree. Beyond  $M = 0.67$  all three are different, with the LDA measurements being the only values going to the correct asymptotic limit.

The quality of the LDA RF-bursts observed, the close match of the measured optical parameters with the design specifications, and the correct low-velocity measurements leading to the expected asymptotic limit ( $M=1$ ) all gave confidence in the operation of the LDA system. After these checkouts, the system was used for flowfield investigations as described in the following sections.

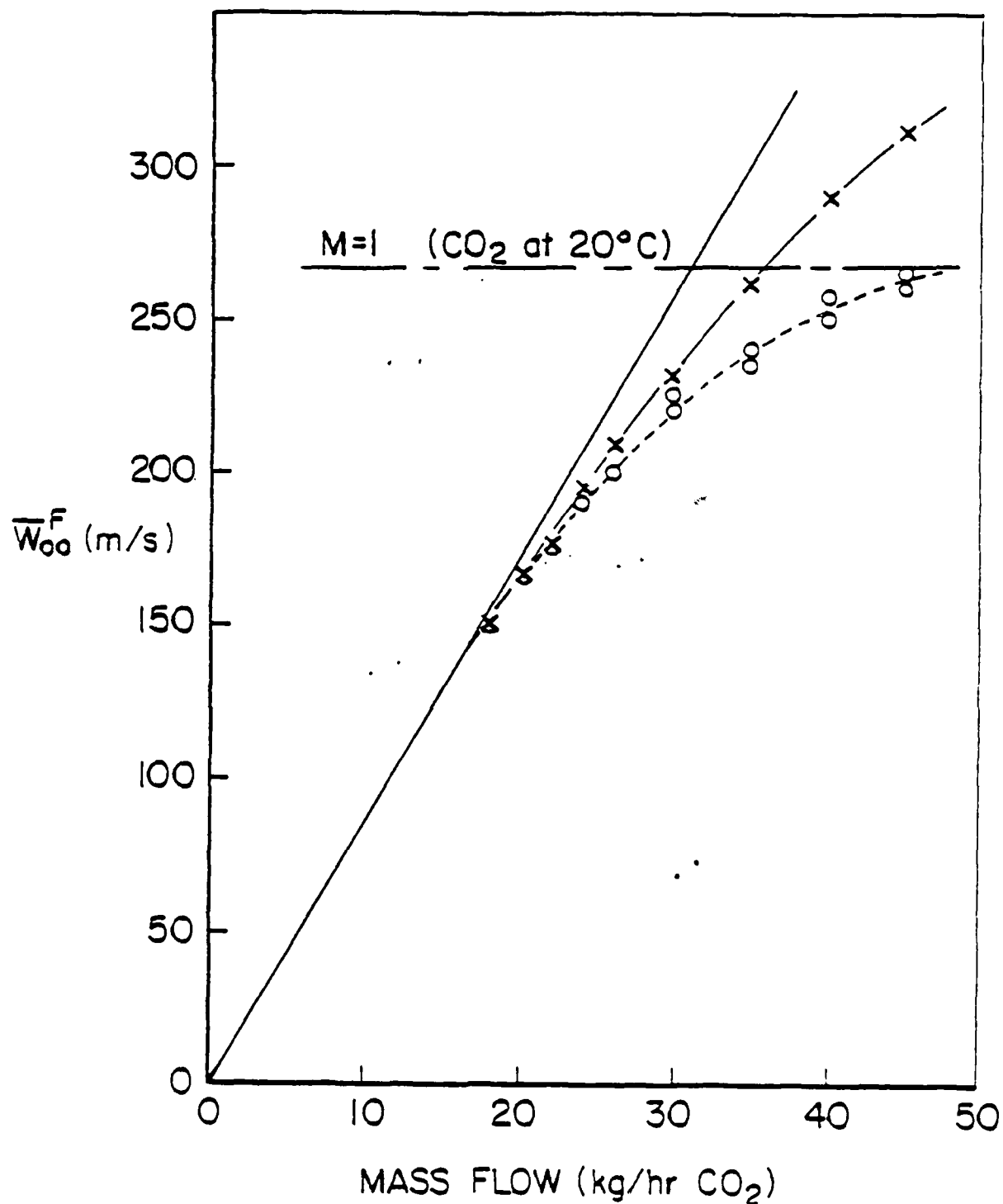


Figure 15. Measured and Computed Centerline Entrance Velocities for the Central Jet as a Function of the Inlet CO<sub>2</sub> Flow. The straight line is the linear computation, the X symbols are the result of a computation that included a compressibility factor, and the O symbols are the LDA measurements.



### SECTION 3

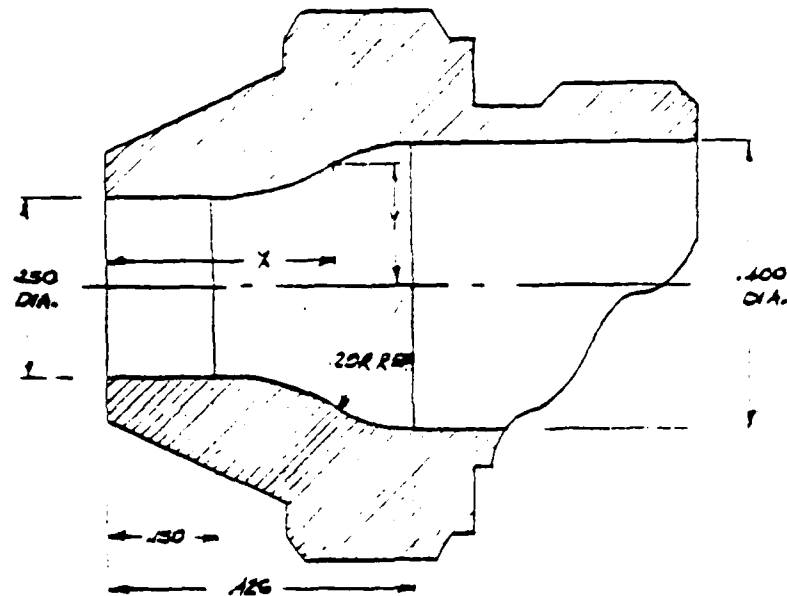
#### FREE JET

The free, turbulent, axisymmetric jet is a standard flow in which new instrumentation and/or hypothesis concerning fluid flow and mixing are tested. It has been studied extensively<sup>12</sup> and there exists a considerable body of published results which can be used in any new study. With this in mind it was decided that the free jet, or as close an approximation as can be obtained in the ducted system available, should be the initial flowfield investigated with the two-dimensional LDA.

The central jet issues into the duct through a nozzle at the center of the bluff body. The nozzle diameter, centerbody diameter, and duct diameter are in the relative proportions of 1:29.3:53.2. Thus the jet will have the characteristics of a free jet for quite some distance downstream. The short-taper nozzle was constructed according to an ASME standard<sup>13</sup> (see Fig. 16) designed to produce a flat profile with a very thin boundary layer. This type of nozzle was selected to ensure commonality with the work of other researchers.

Classical studies of the free jet have concentrated on such parameters as the centerline velocity decay, profiles of the mean velocity and the velocity fluctuations taken at a fixed axial location, and the downstream development of these profiles. Recently researchers have investigated the mixing processes in the jet, dividing the jet into different regions of behavior (see Fig. 17) and trying to interpret the parametric variations which characterized these regions.<sup>14</sup>

The study of jet entrainment has recently received new experimental attention using more modern tools. Past studies have included the porous wall technique used by Ricou and Spalding<sup>15</sup> and Hill.<sup>16</sup> More detailed study of the development



| X    | Y     | X    | Y     |
|------|-------|------|-------|
| .150 | .1250 | .290 | .1536 |
| .160 | .1251 | .300 | .1583 |
| .170 | .1255 | .310 | .1636 |
| .180 | .1262 | .320 | .1695 |
| .190 | .1271 | .330 | .1753 |
| .200 | .1281 | .340 | .1805 |
| .210 | .1291 | .350 | .1849 |
| .220 | .1317 | .360 | .1887 |
| .230 | .1338 | .370 | .1919 |
| .240 | .1362 | .380 | .1946 |
| .250 | .1389 | .390 | .1967 |
| .260 | .1420 | .400 | .1983 |
| .270 | .1455 | .410 | .1993 |
| .280 | .1493 | .426 | .2000 |

Figure 16. Central Jet Nozzle, Designed as Described in ASME Power Test Codes PTC 19.5, 4-1959, Long-Radius Flow Nozzles, Low 3 Series.

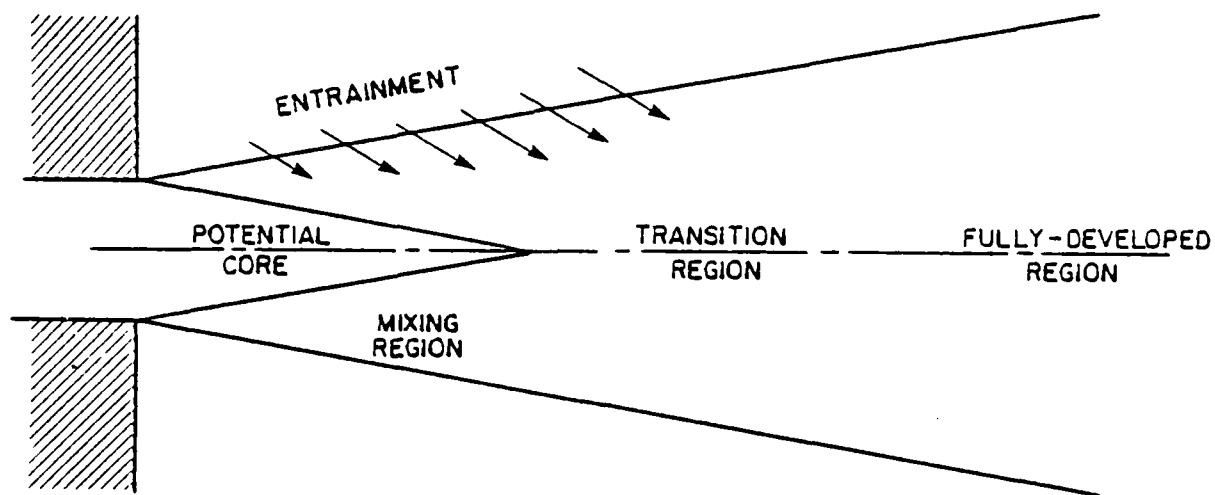


Figure 17. Schematic of Axisymmetric Jet Flow Showing the Various Regions Encountered in the Flow Development. The jet is shown issuing from a wall, as observed in this study.

region is possible by examining the downstream velocity profiles. Crow and Champagne<sup>17</sup> and Boguslawski and Popiel<sup>18</sup> used hot-wire probes to measure the velocity profile in the region out to 10 nozzle diameters downstream. Their results have been contrasted<sup>13</sup> with the earlier measurements by Hill<sup>16</sup> in the same region and the further downstream results<sup>15</sup> (out to several hundred diameters). Substantial differences have been found. The LDA system was used to study the velocity profiles in the region between 0.4 and 105 fuel tube diameters. This region overlaps that of the previous studies and it was thought that this might clarify the observed differences.

### 3.1 EXPERIMENTS

The experiments concentrated on the central jet with a CO<sub>2</sub> flow of 6 kg/hr, the same flow used in the coaxial studies. Additional profiles were made at selected locations for CO<sub>2</sub> flows of 2 and 16 kg/hr, to look at the scaling as a function of the central jet Reynolds number (see Tables 2 and 3).

TABLE 2  
FLOW RATES USED IN CENTRAL JET STUDIES

| Flow (CO <sub>2</sub> )<br>kg/hr | Reynolds Number<br>Re ( $\times 10^{-3}$ ) |
|----------------------------------|--|
| 2                                | 11   |
| 6                                | 31   |
| 16                               | 83   |

TABLE 3  
PROFILE MEASUREMENT LOCATIONS

| $Z/D_F$<br>CO <sub>2</sub><br>kg/hr | 0.4 | 1.0  | 2.1  | 3.1  | 4.2  | 6.3 |
|-------------------------------------|-----|------|------|------|------|-----|
| 2                                   | x   |      | x    |      |      |     |
| 6                                   | x   | x    | x    | x    | x    | x   |
| 16                                  | x   |      | x    |      |      |     |
| $Z/D_F$<br>CO <sub>2</sub><br>kg/hr | 8.4 | 10.5 | 20.9 | 29.3 | 83.8 | 105 |
| 2                                   | x   |      | x    |      |      |     |
| 6                                   | x   | x    | x    |      | x    | x   |
| 16                                  | x   |      | x    | x    | x    |     |

The entrance profile was approximated by the profile at  $Z/D_F = 0.4$ , the closest approach of the LDA. The central jet boundary layer is thin in this region, near the entrance plane, and the velocity gradient is steep. The LDA spot dimensions form an acceptance aperture which is convoluted with the true flowfield to provide the measured flowfield. To minimize the effects of this aperture the LDA scans were made in the vertical plane going through the centerline, in which direction the LDA spot aperture is minimum.

The measured profiles were combined with density profiles measured with intrusive probes.<sup>19</sup> A numerical integration scheme (assuming cylindrical symmetry) was used to obtain the mass and momentum flow within each profile. The mass of CO<sub>2</sub> was computed (the intrusive probe measures the fraction of CO<sub>2</sub> in the sample, the concentration being diluted by the air that the jet entrains). Mass and momentum conservation required that the CO<sub>2</sub> mass flow be constant, equal to the issuing central jet CO<sub>2</sub> flow, and that the jet momentum be constant at every axial station

(assuming that the contribution of the natural abundance of  $\text{CO}_2$  in the entrained air is negligible compared with the jet flow).

### 3.2 RESULTS

Figures 13(a) to (m) show plots of the central jet profiles measured. Each figure presents the results for the  $w$  and  $v$  components. For these scans  $w$  is the axial component and  $v$  is the radial component, except for 13(i) and 13(k) where  $v$  is the azimuthal component. Each page has four plots: average velocity; rms value of the fluctuating component; skewness; and kurtosis of the measurement distribution. (Skewness relates to the symmetry of the distribution; it is zero for a symmetric distribution. Kurtosis is a shape parameter describing the distribution; it is 3 for a Gaussian distribution and 1.8 for a flat-top distribution.)

The profile at  $Z/D_f = 0.4$  is the inlet profile<sup>2</sup>. The flat top of the velocity profile is evident. Other measurements taken in this region confirmed the flat profile. The shear layer thickness observed is largely due to the width of the LDA measurement volume (300  $\mu\text{m}$ ). The shear layer width measured from the velocity profile indicates the true shear layer's maximum width is on the order of 100  $\mu\text{m}$ . The symmetry of the flow (in the measurement plane) is evident in all four plots shown.

The skewness, when traced from  $r/R_f = 0$  outward shows a sharp drop from 0 to -1, then a rapid increase to +1, and then a drop back to 0. The variation occurs within the observed shear layer. This shape is anticipated for the situation where the shear layer is thinner than the LDA cross section. As the measurement volume moves into the shear layer, a large part of it remains in the potential core. Hence the skewness will be negative. When the spot straddles the shear layer, the skewness will tend to zero. As the spot moves to the outside but still overlaps the shear layer, the bulk of the LDA volume will be in

|         |     |
|---------|-----|
| $Z/D_F$ | 0.4 |
| FF      | 6   |
| AF      | 0   |

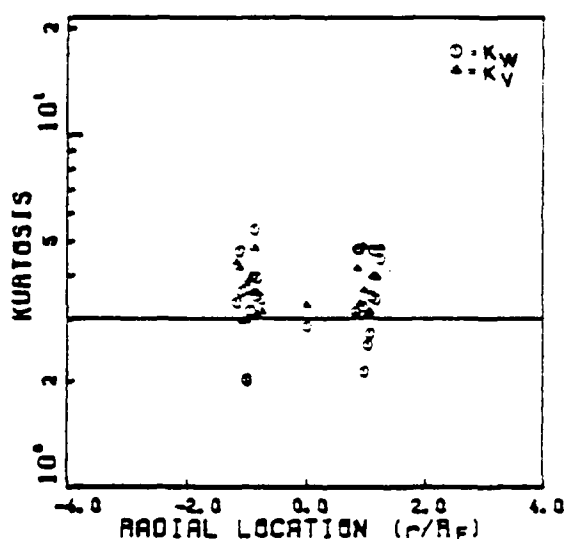
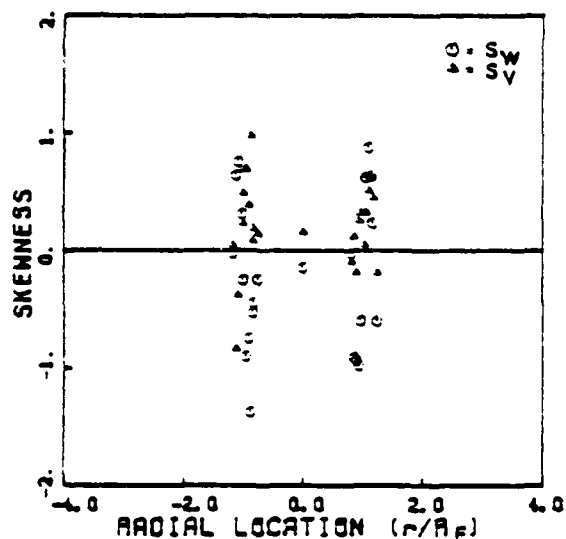
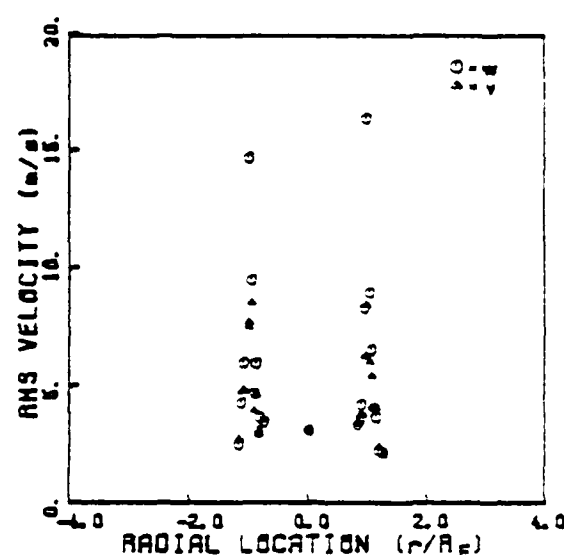
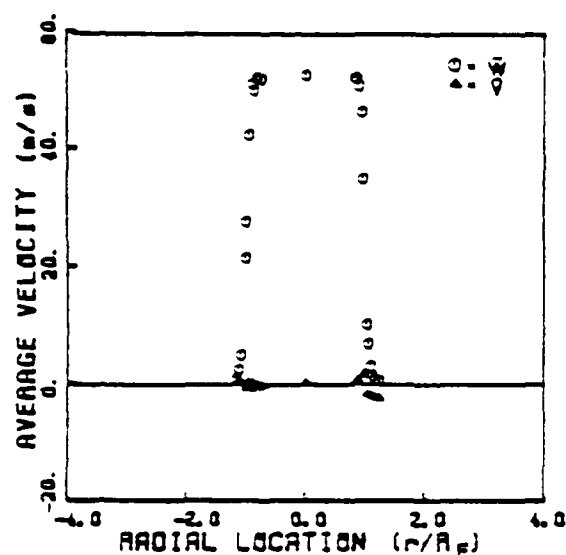
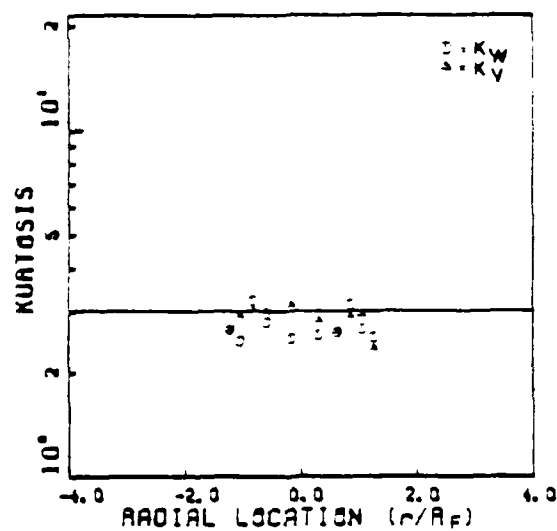
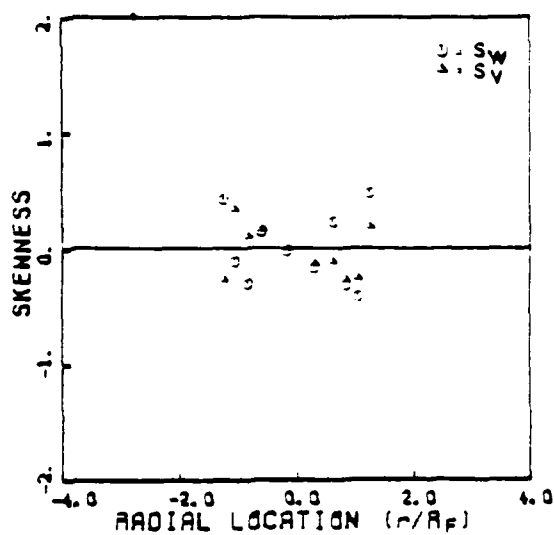
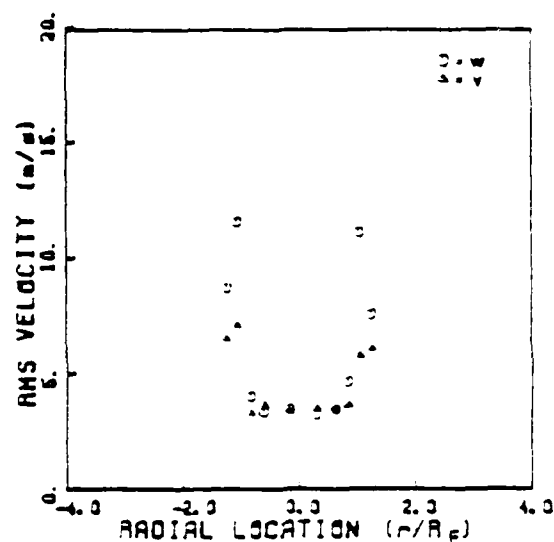
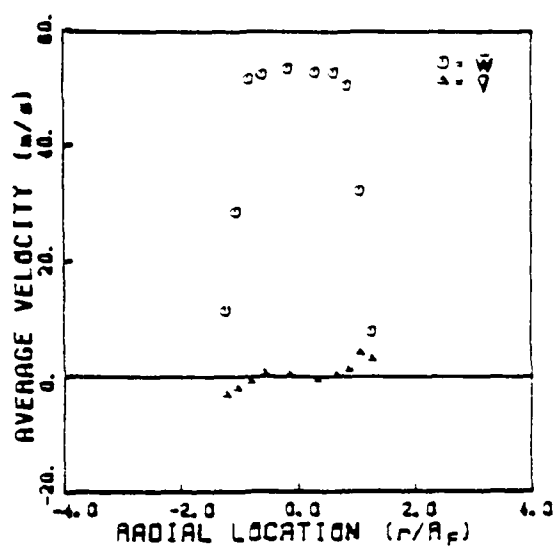


Figure 13. (a) - (m) Profiles of Velocity Distribution Descriptors Based Upon the First Four Moments. Measurements are for the central-jet-only condition with  $\text{CO}_2$  mass flow of 6 kg/hr. The location and flow conditions for each set are given at the top of the page. Figures 13(i) and 13(k) are X-scans so the V-component is the azimuthal component. For all the other plots the V-component is the radial component. The W-component is always the axial component.

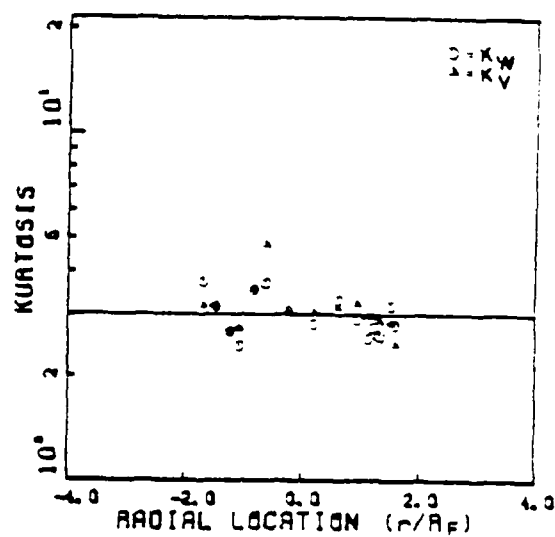
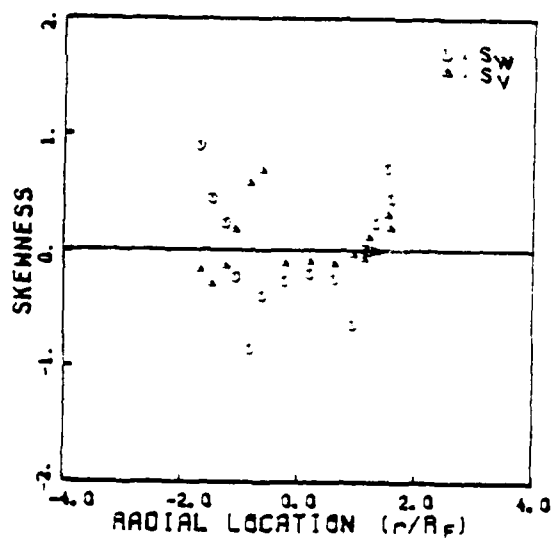
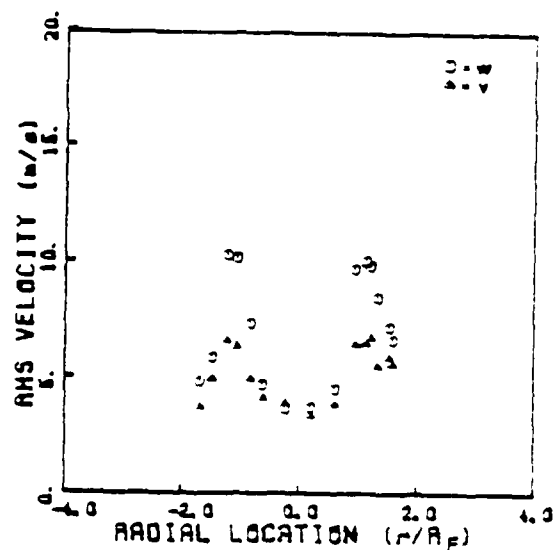
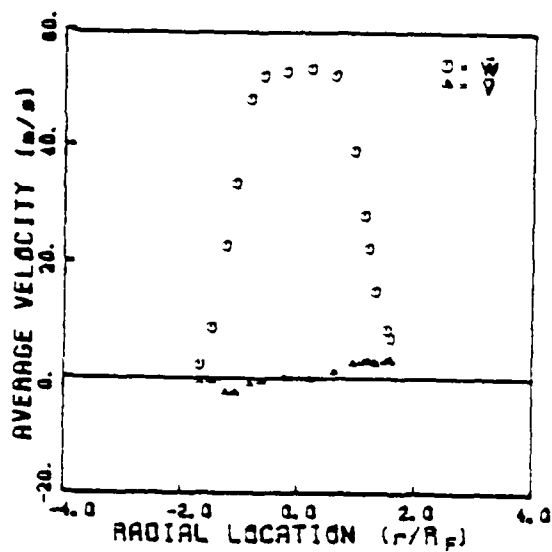
|         |     |
|---------|-----|
| $Z/D_F$ | 1.0 |
| $PF$    | 6   |
| $AF$    | 0   |



(b)

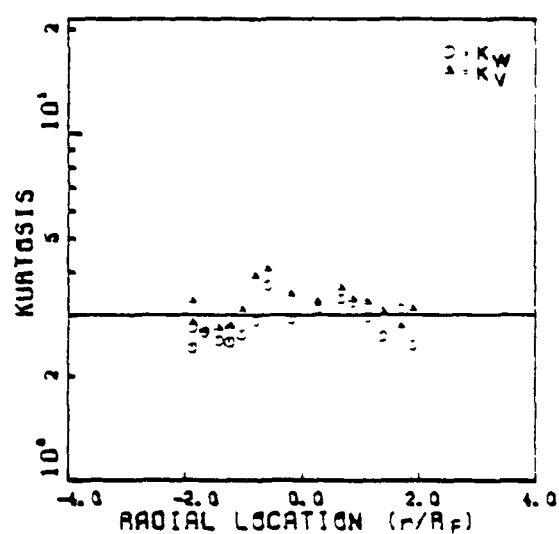
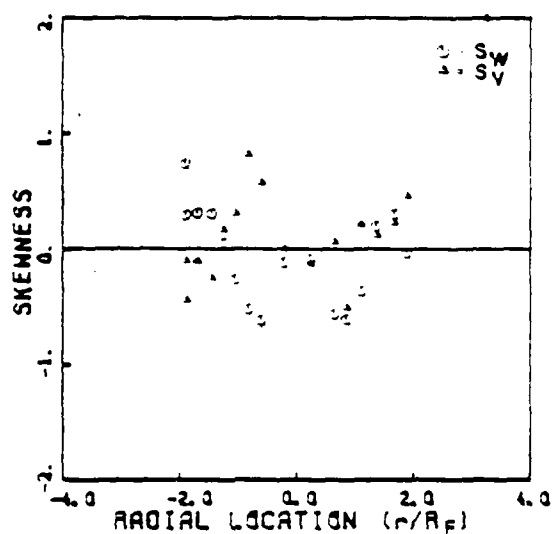
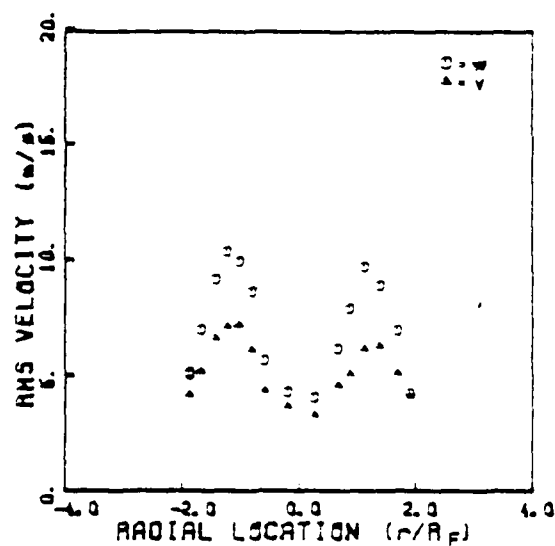
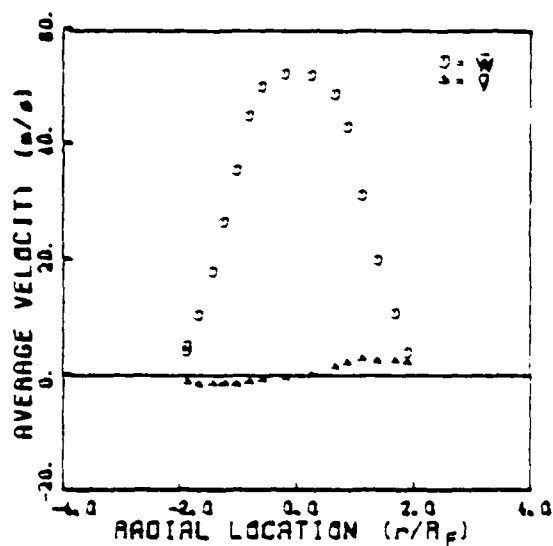


|         |     |
|---------|-----|
| $Z/D_p$ | 2.1 |
| FF      | 6   |
| AF      | 0   |



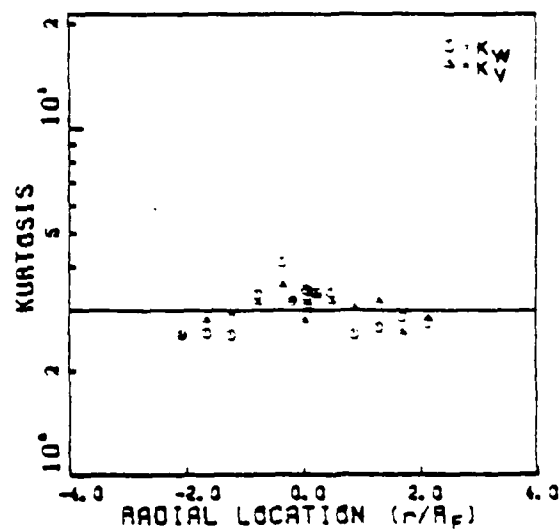
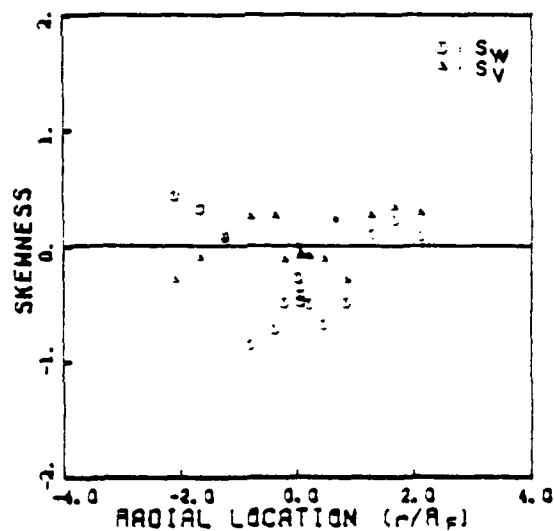
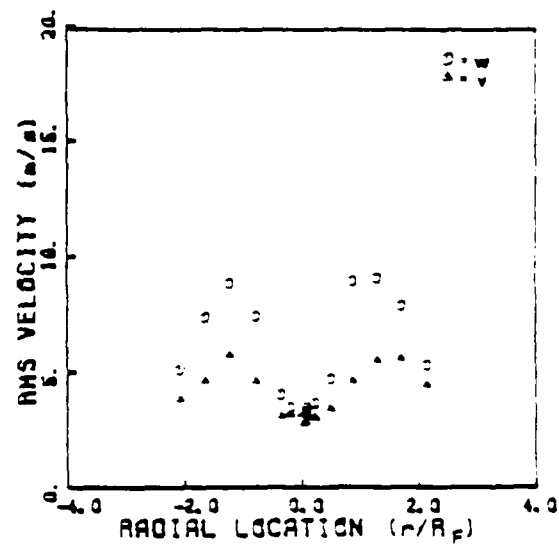
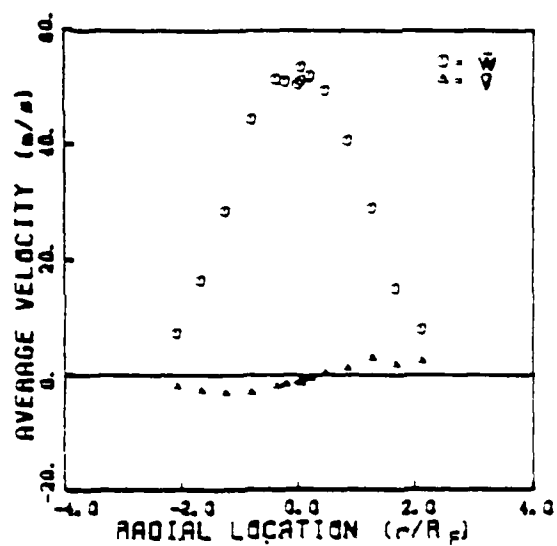
(c)

|         |     |
|---------|-----|
| $Z/D_F$ | 3.1 |
| FF      | 6   |
| AF      | 0   |



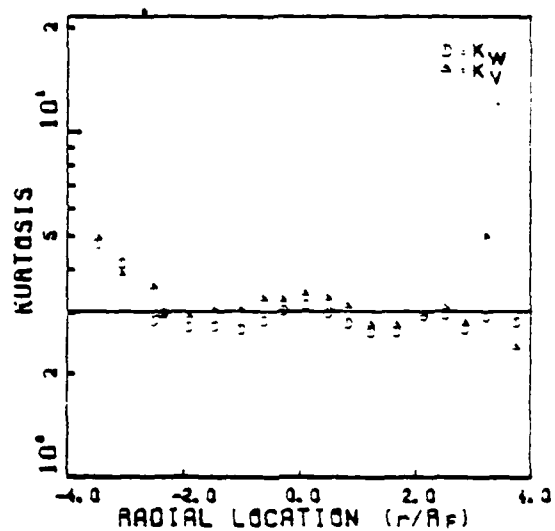
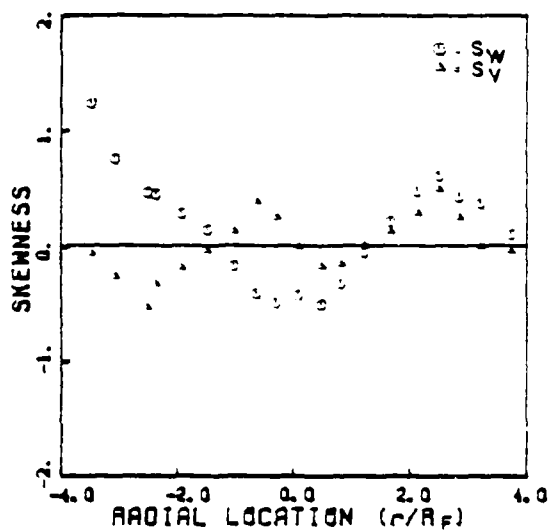
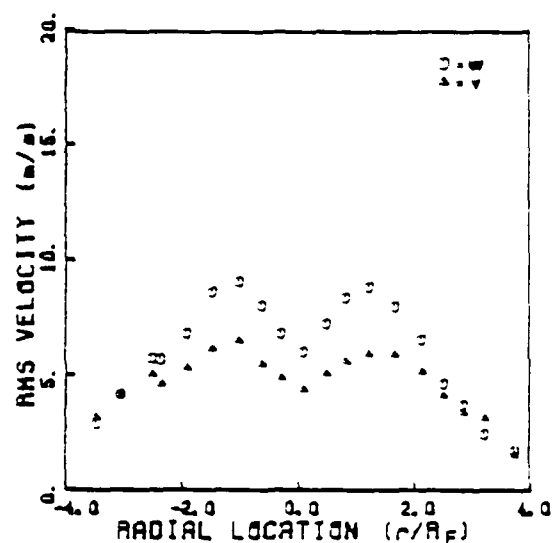
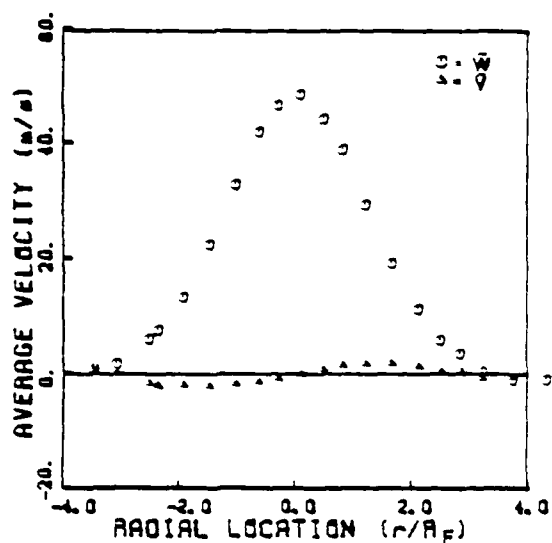
(d)

|                  |     |
|------------------|-----|
| Z/D <sub>p</sub> | 4.2 |
| FF               | 6   |
| AF               | 0   |



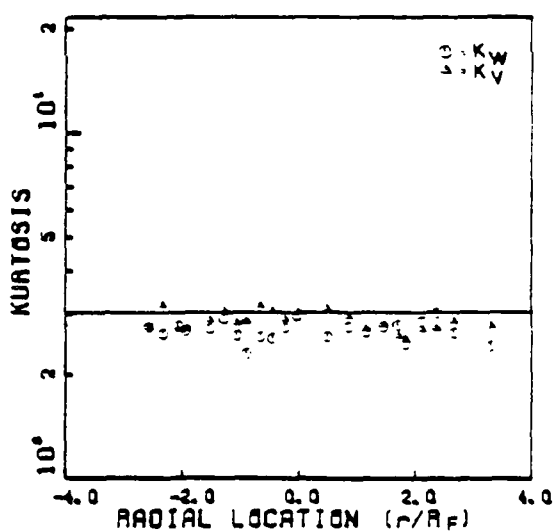
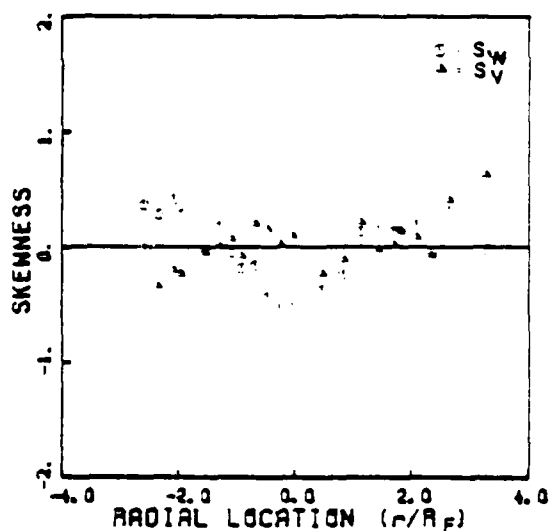
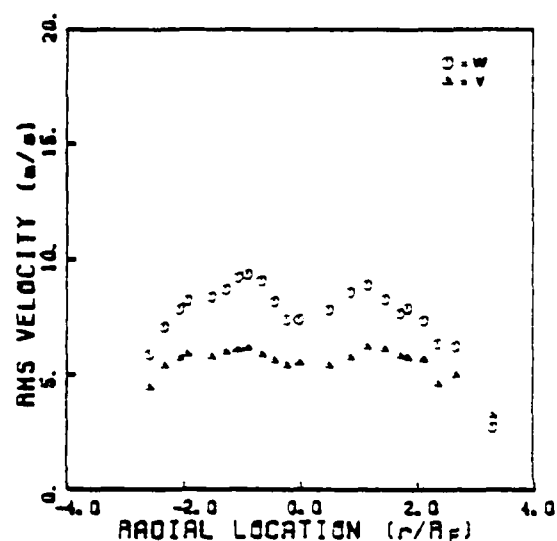
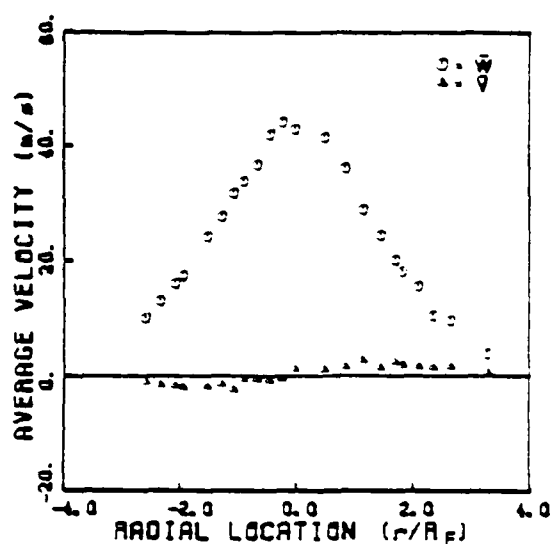
(e)

|         |     |
|---------|-----|
| $Z/D_F$ | 6.3 |
| FF      | 6   |
| AF      | 0   |



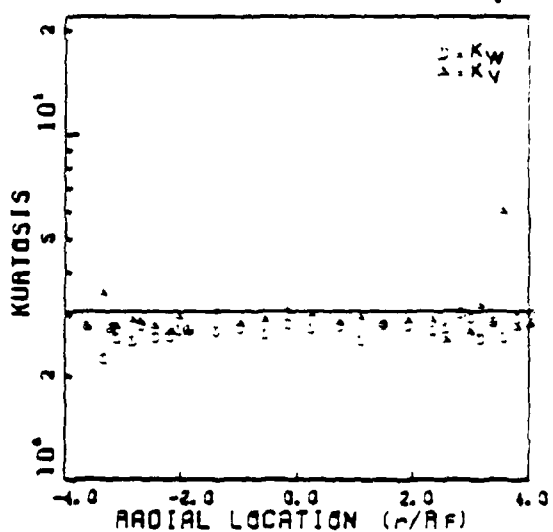
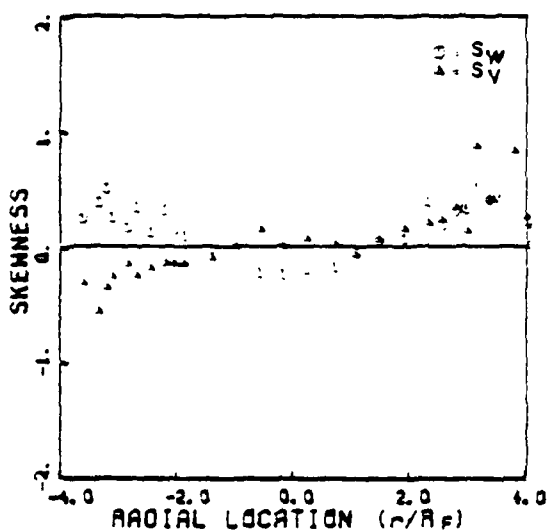
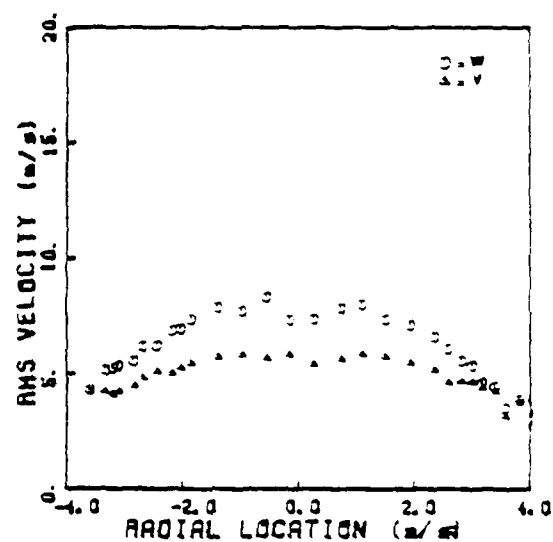
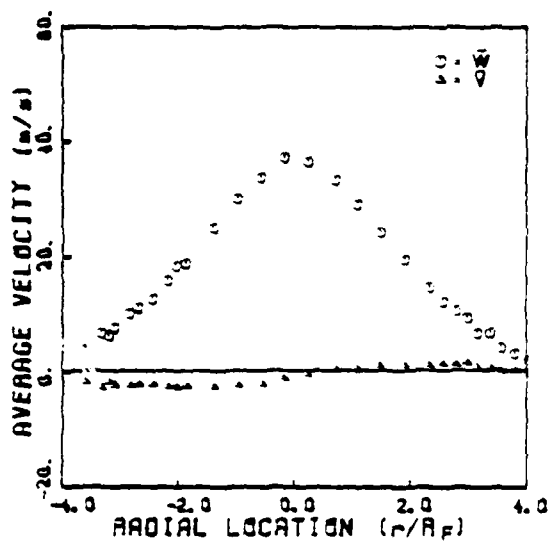
(f)

|                  |     |
|------------------|-----|
| Z/D <sub>p</sub> | 8.4 |
| FF               | 6   |
| AF               | 0   |



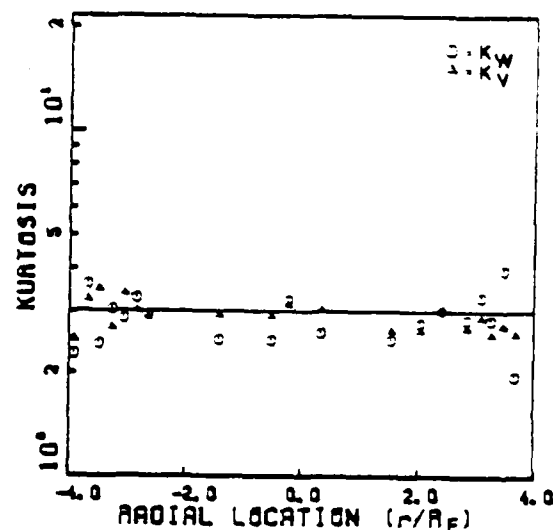
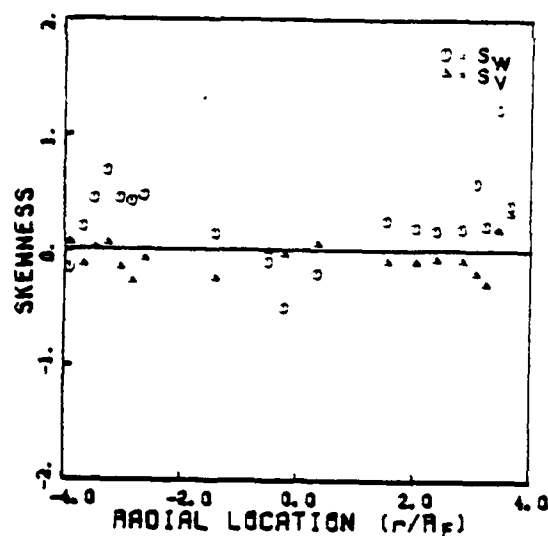
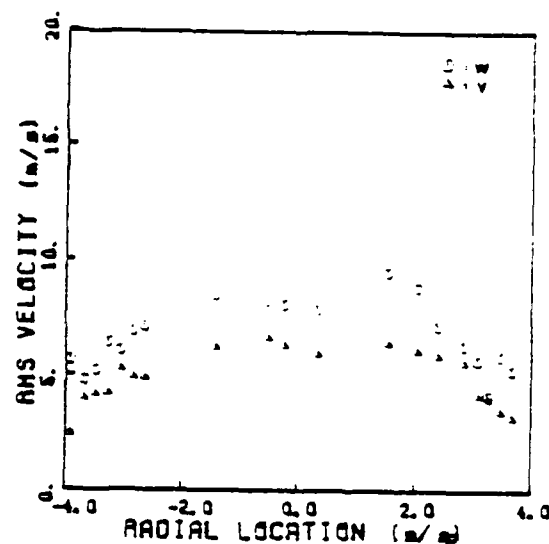
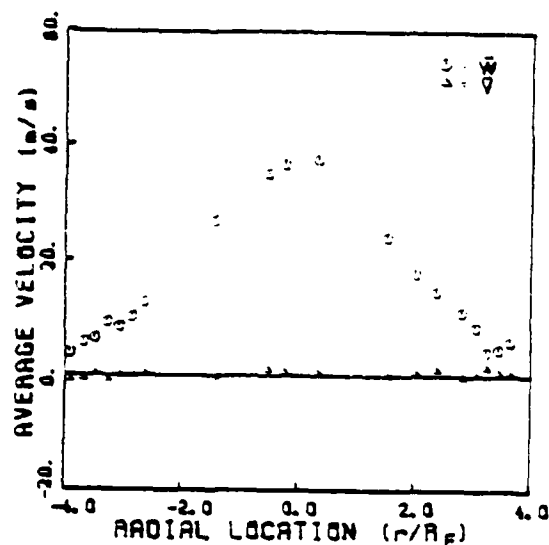
(g)

|         |      |
|---------|------|
| $Z/D_F$ | 10.5 |
| FF      | 6    |
| AF      | 0    |



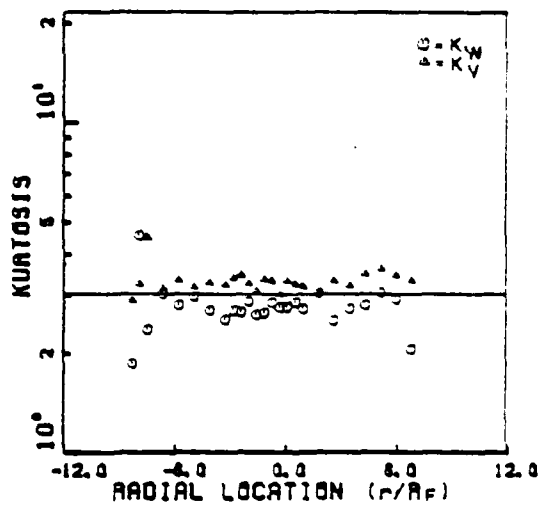
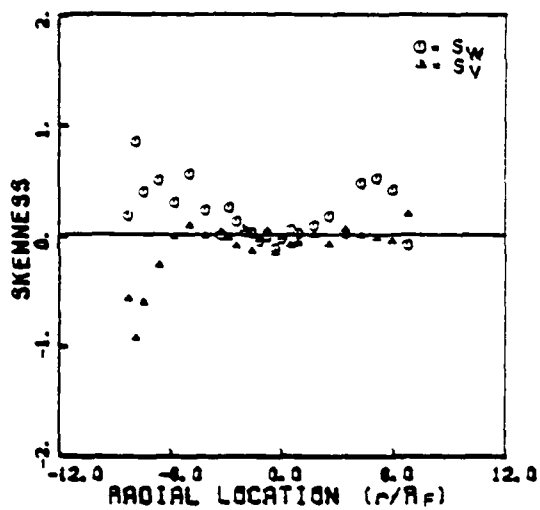
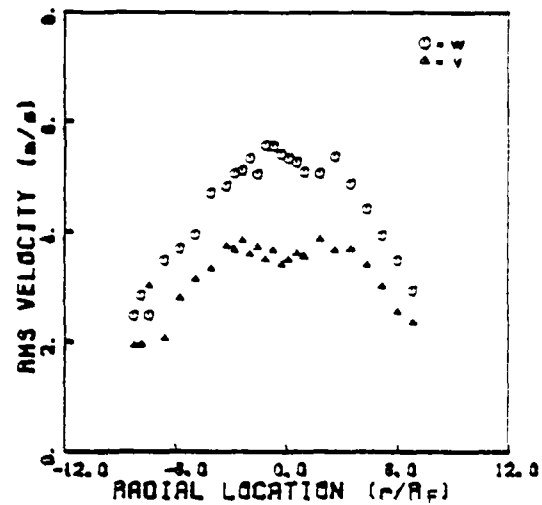
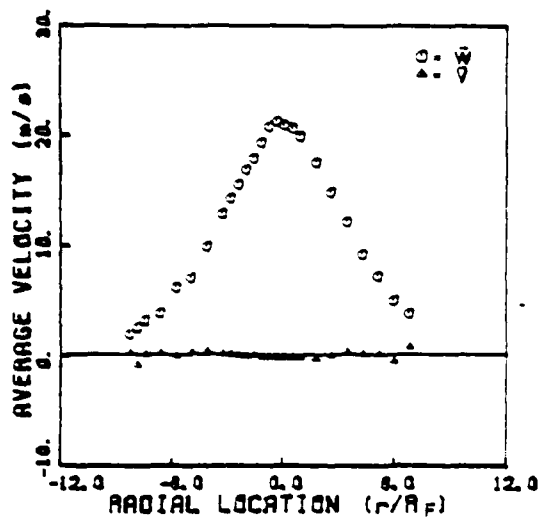
(h)

|                  |      |
|------------------|------|
| Z/D <sub>p</sub> | 10.5 |
| FF               | 6    |
| AF               | 0    |



(i)

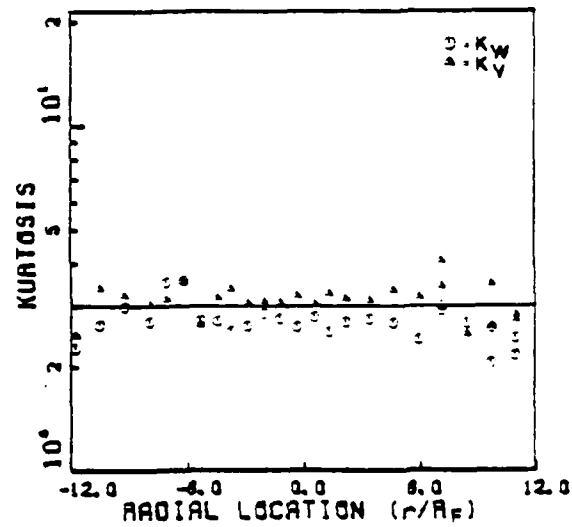
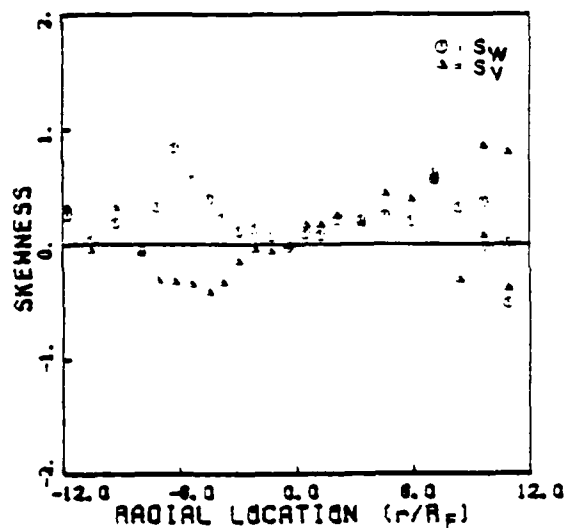
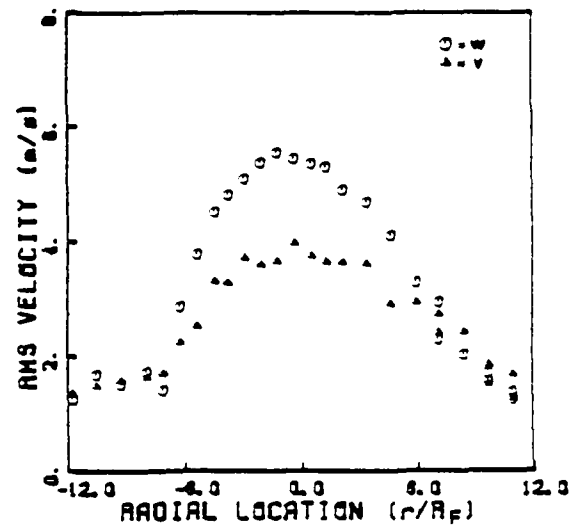
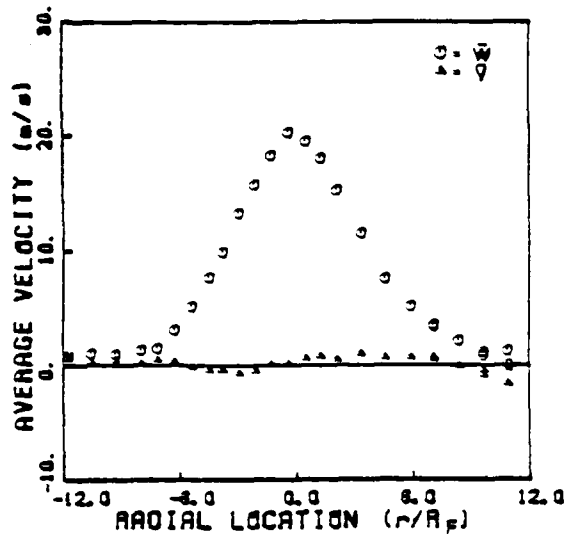
|                  |      |
|------------------|------|
| Z/D <sub>F</sub> | 20.9 |
| FF               | 6    |
| AF               | 0    |



(j)

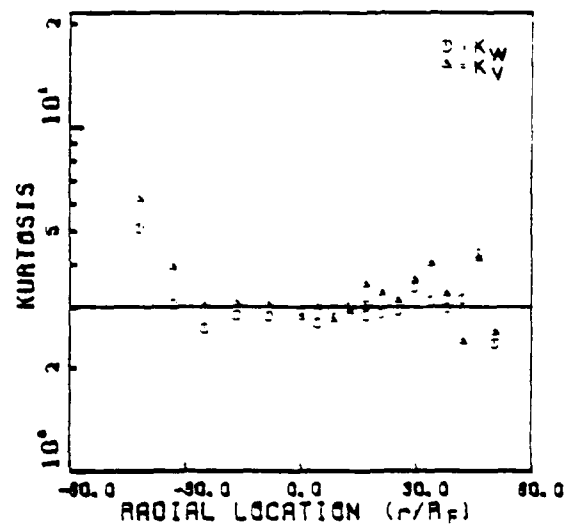
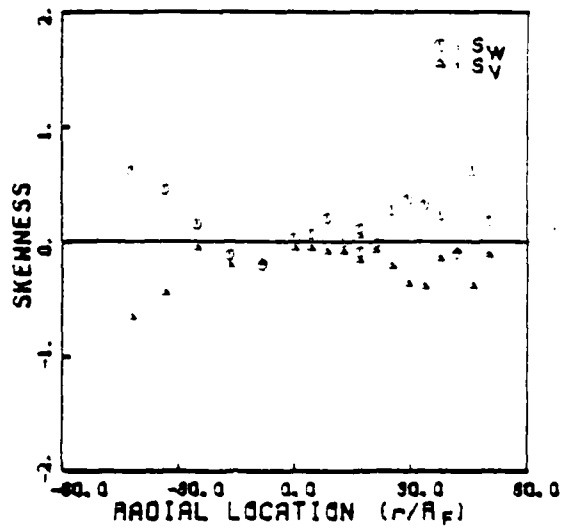
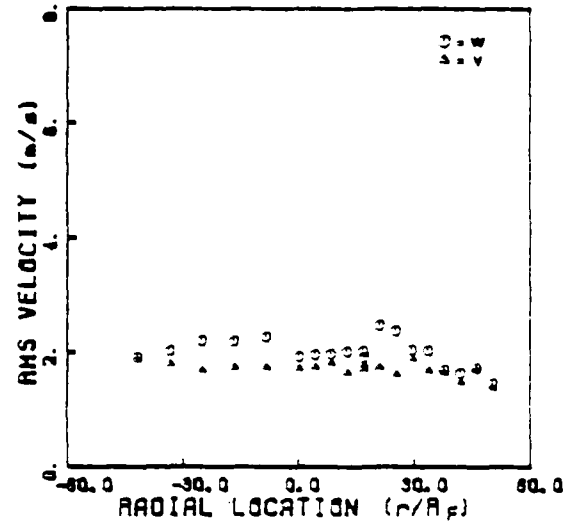
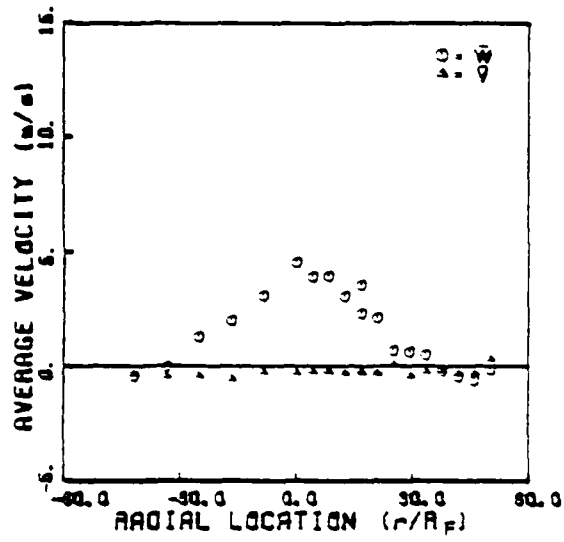


|         |      |
|---------|------|
| $Z/D_F$ | 20.9 |
| FF      | 6    |
| AF      | 0    |



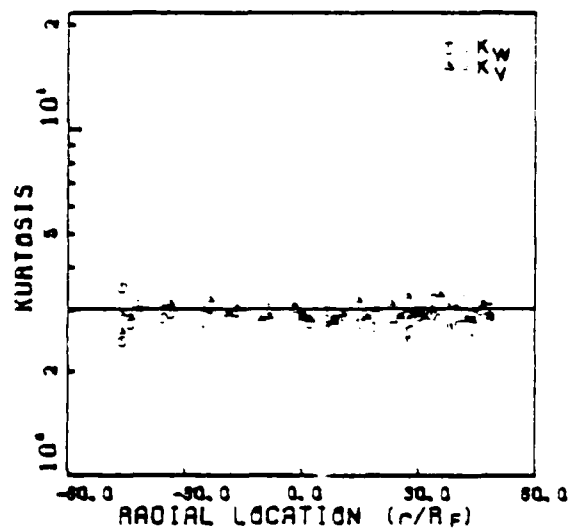
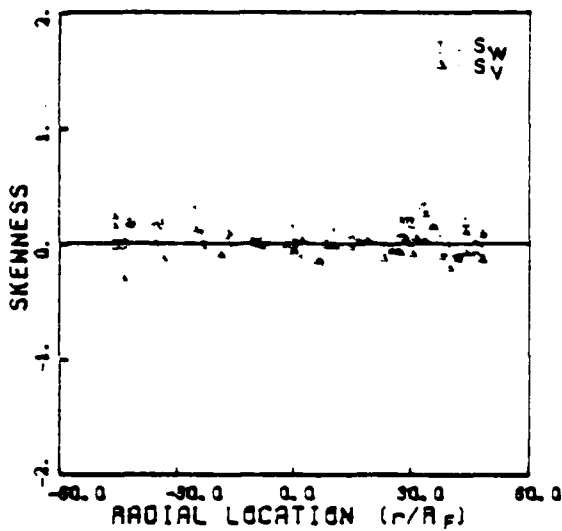
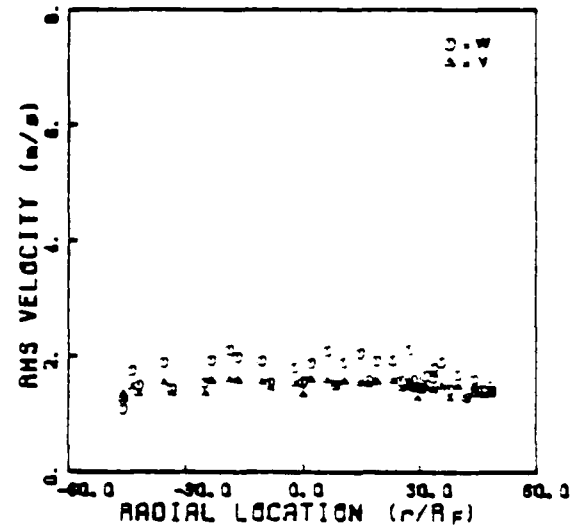
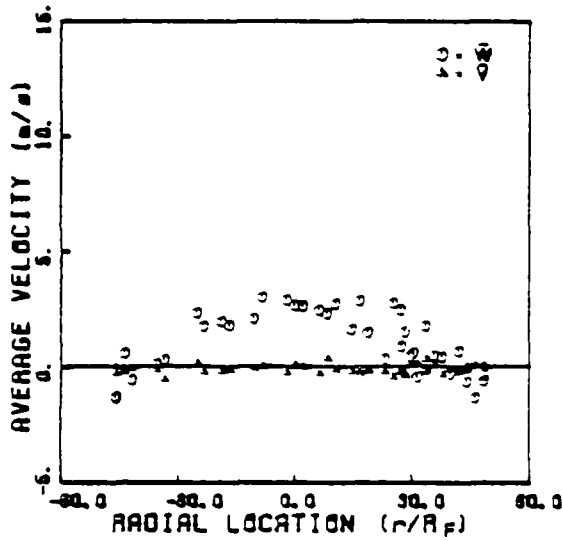
(k)

|                  |      |
|------------------|------|
| Z/D <sub>p</sub> | 83.8 |
| FF               | 6    |
| AF               | 0    |



(1)

|                  |       |
|------------------|-------|
| Z/D <sub>p</sub> | 104.7 |
| FF               | 6     |
| AF               | 0     |



(m)

the zero velocity region. The contribution of the shear flow will provide a positive skewness. Once the spot is completely outside the flow, the skewness should decrease back to zero.

At the downstream measurement stations the shear layer grows in width and the effects of the LDA spot size diminish. Far enough downstream the shapes of the profiles will reflect the fluid dynamics and not be influenced by the LDA dimensions, as at the upstream stations.

Several key parameters are used to describe the jet profile as it develops downstream. One of these is the width of jet. (In our discussions we will use  $\phi_{1/2}$ , the full width at half-maximum velocity.) There are many references to the development of a free jet into the same fluid (e.g., air-air). Hinze<sup>20</sup> discusses the work of Forstall<sup>21</sup> whose measurements extrapolate to the relation  $\phi_{1/2} = 0.25 Z$  for a free jet into a still gas, and the work of Van der Hegge Zijnen who obtained  $\phi_{1/2} = 0.16 (Z+a)$ ,<sup>22</sup> where  $a$  is the virtual origin of the jet. Other reported measurements are  $\phi_{1/2} = 0.172 Z$ <sup>23</sup> and  $\phi_{1/2} = 0.186 Z$ <sup>24</sup>. For the jet studied in this experiment, CO<sub>2</sub> into air, the results shown in Figure 19 yield the best-fit relationship

$$\begin{aligned}\phi_{1/2} &= 1.10 (Z/D_F - 4.8) & (6) \\ &= 0.230 (Z + a)\end{aligned}$$

with

$$a = -4.8 D_F.$$

The data point at  $Z/D_F = 104.7$  was not used since it was determined that at this location the central jet had spread so much that it was interacting with the duct boundary layer.

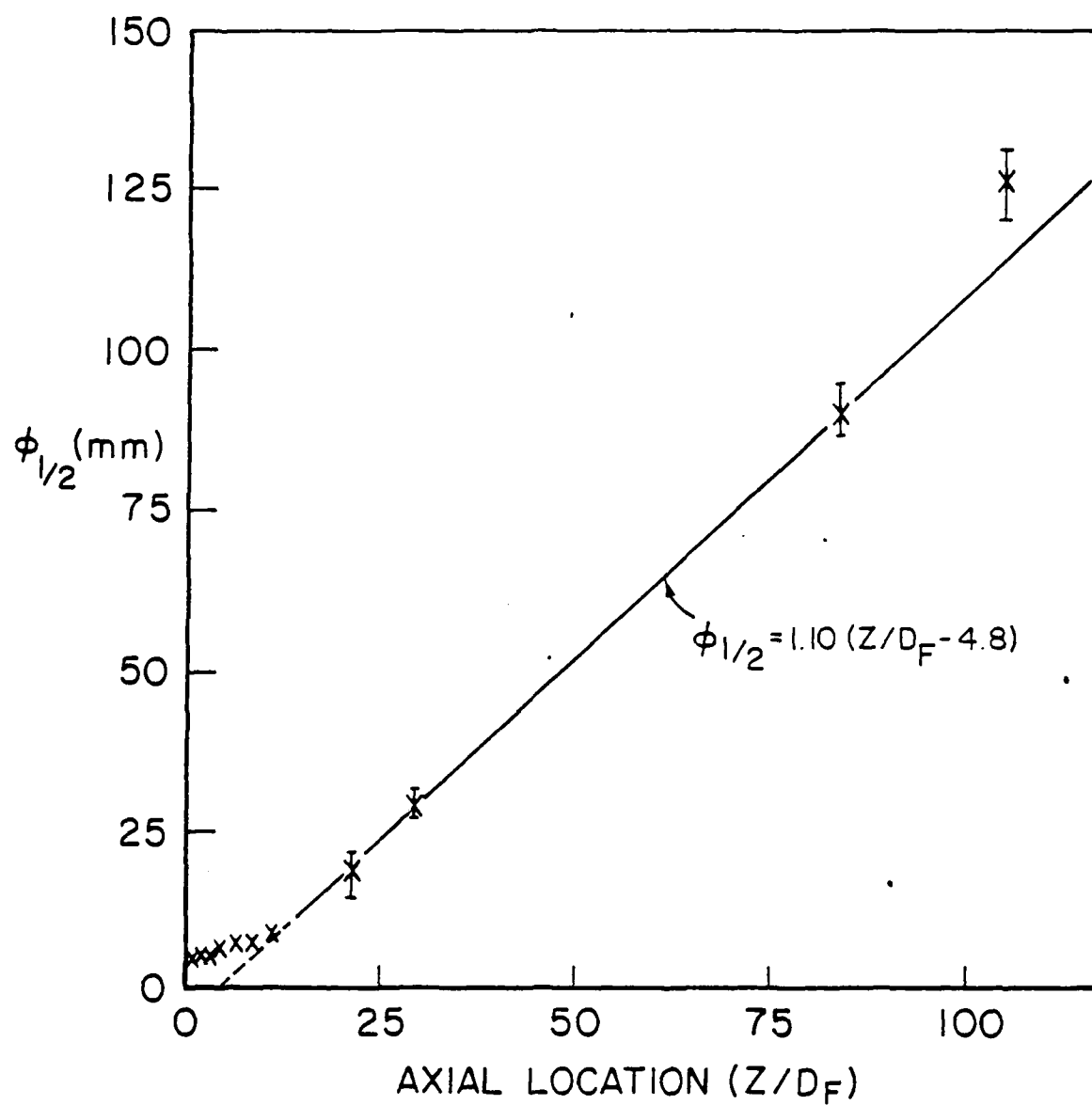


Figure 19. Development of the Full Width of the Central Jet Measured at Half the Velocity Maximum. Note that the measurement at  $Z/D_F = 104.7$  has not been used since the jet has spread to where it is interacting with the duct.

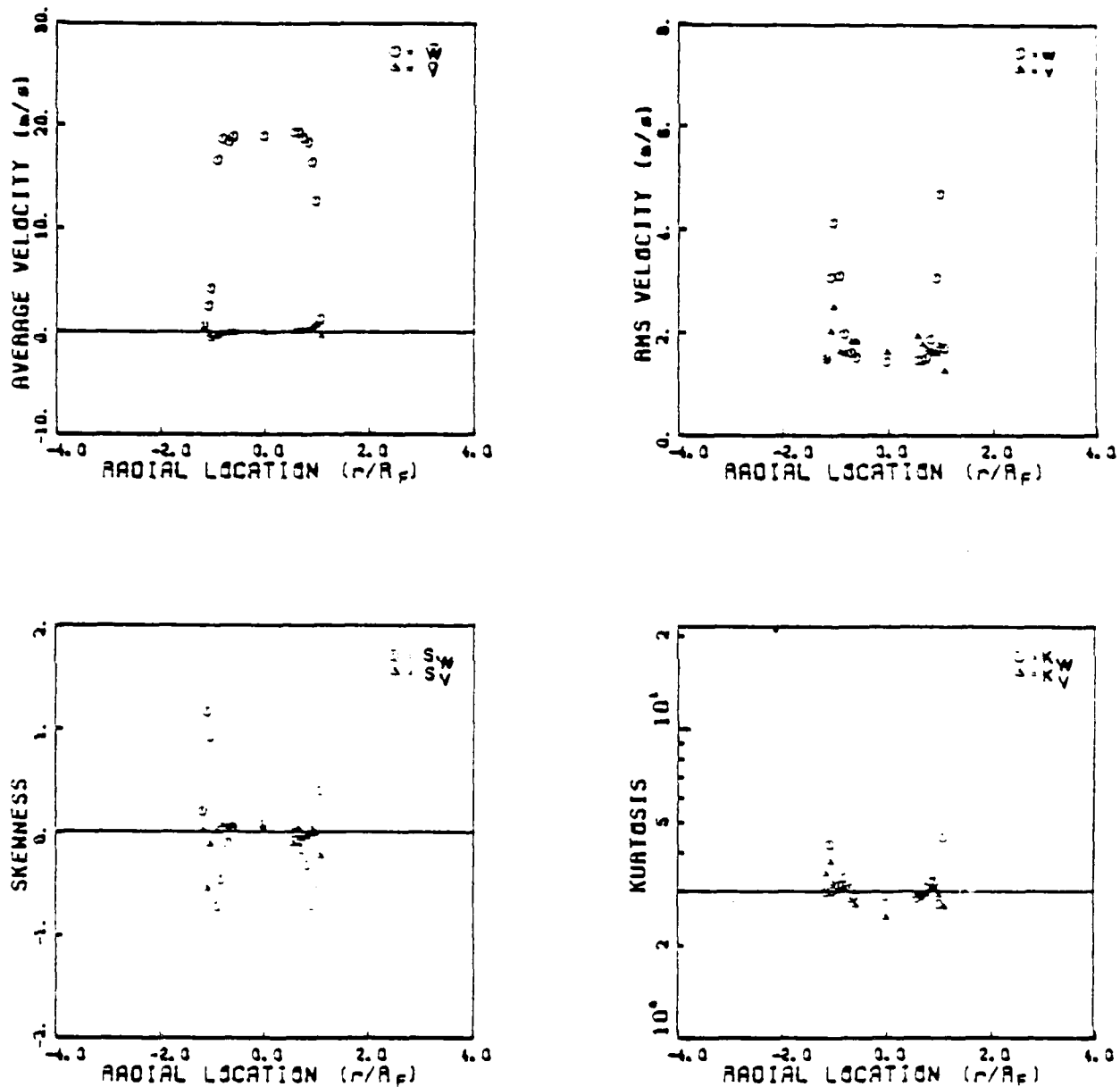
Measurements were also made with jet flows of 2 and 16 kg/hr. The results shown in Figure 19 encompass all measurements. The profiles at 2 kg/hr [Figs. 20(a) to 20(d)] and 16 kg/hr [Figs. 21(a) to 21(f)] were taken at a limited number of stations. They were used for comparison with the profiles of 6 kg/hr flow to investigate systematic variations with Reynolds number. Figures 22(a) to (d) are overlays of the average axial velocity and rms axial velocity fluctuation for the three flow rates, each normalized to its centerline inlet velocity, at the four downstream stations. In Figure 22(a), the inlet profile shows all three profiles to be identical, both velocity and rms fluctuation. In Figures 22(b) to 22(d) the profiles of the 2 kg/hr and 6 kg/hr flows remain the same; the 16 kg/hr flow profile increasingly deviates from the other two the farther downstream the measurement. In the region of the flow field  $z > 4$  cm, all the profiles have the same shape; the flow at 16 kg/hr does not attain the same proportion of the maximum velocity. The shape of the velocity profile is

$$\frac{\bar{w}^F(r)}{\bar{w}_0^F} = e^{-2.29(\frac{r}{z/D_F - 4.3})^2} \quad (7)$$

where the numerical factor in the exponent was selected by matching the observed width data of Figure 19.

Many of the numerical models used for predicting fluid flow assume isotropic turbulence. The fully developed region illustrated in Figure 17 is thought to be the region characterized by isotropic turbulence. From Figures 18(k) and 21(f) it can be seen that the rms fluctuations have not become isotropic at  $z/D_F = 21$  for  $Re = 31,000$  and  $z/D_F = 84$  for  $Re = 83,000$ , considerably farther downstream than was anticipated. Comparing the rms fluctuations of the V component in Figures 13(h) and 13(i) shows that the radial and azimuthal components are already

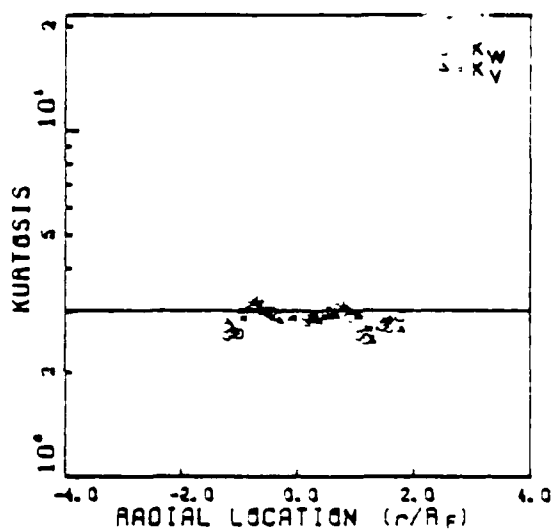
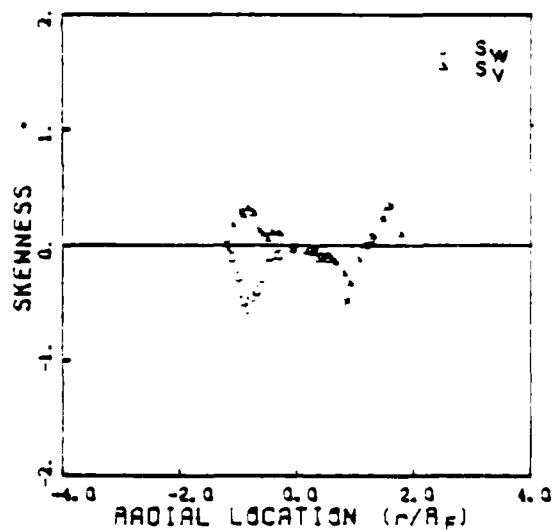
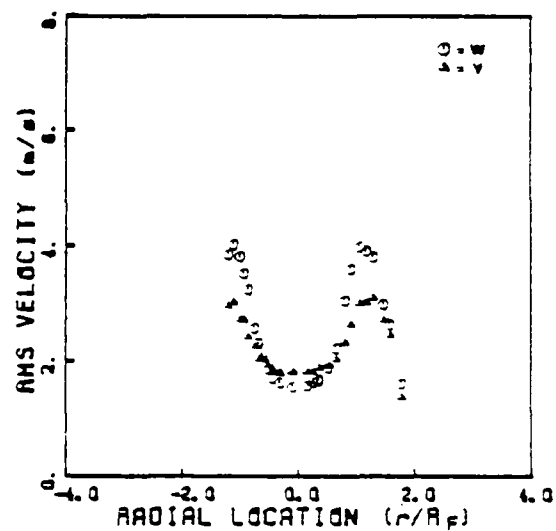
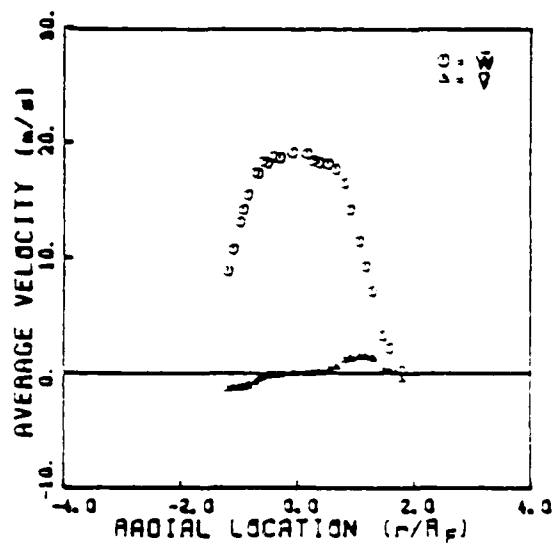
|         |     |
|---------|-----|
| $Z/D_p$ | 0.4 |
| FF      | 2   |
| AF      | 0   |



(a)

Figure 20. (a) - (d) Profiles of Velocity Distribution Descriptors Based Upon the First Four Moments. Measurements are for the central-jet-only condition with  $\text{CO}_2$  mass flow of 2 kg/hr.

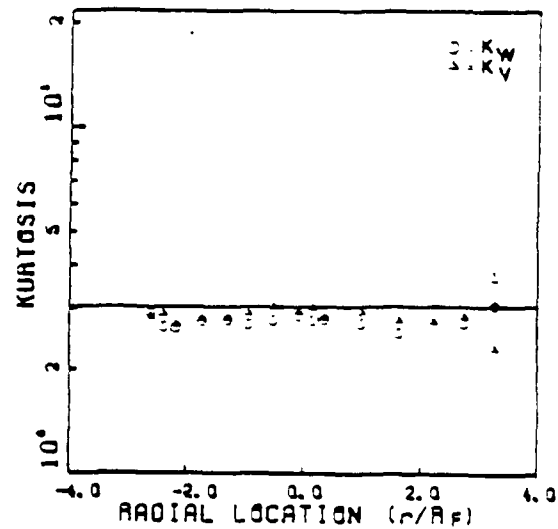
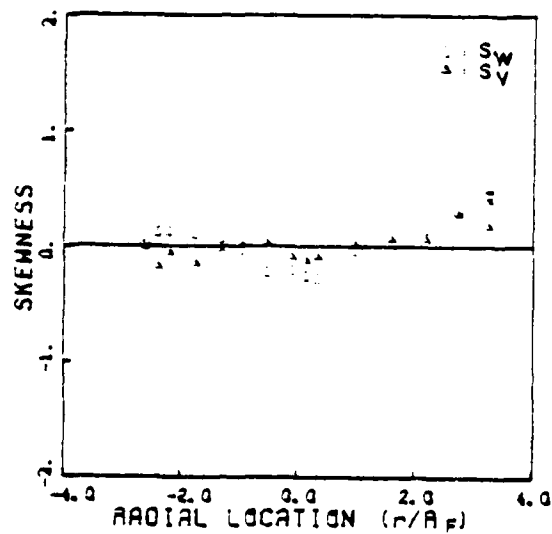
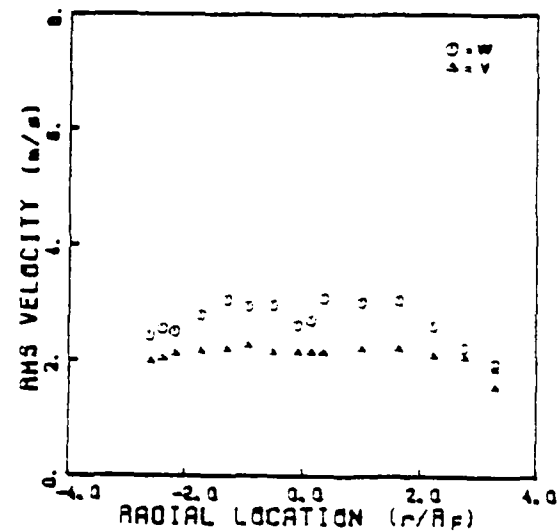
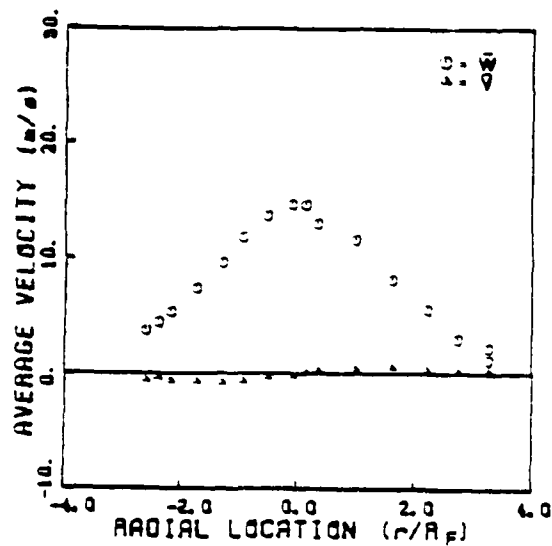
|                  |     |
|------------------|-----|
| Z/D <sub>F</sub> | 2.1 |
| FF               | 2   |
| AF               | 0   |



(b)

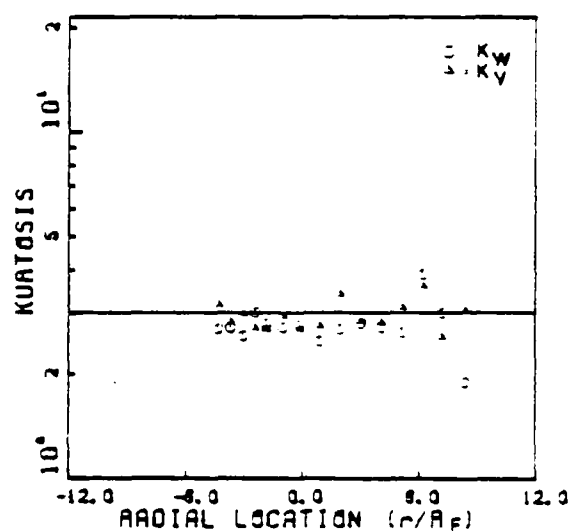
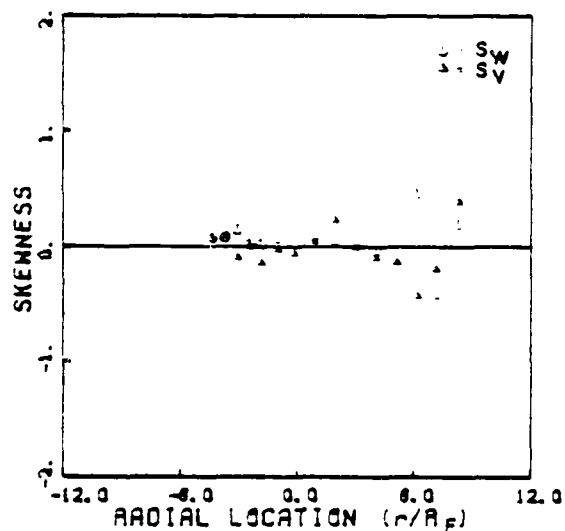
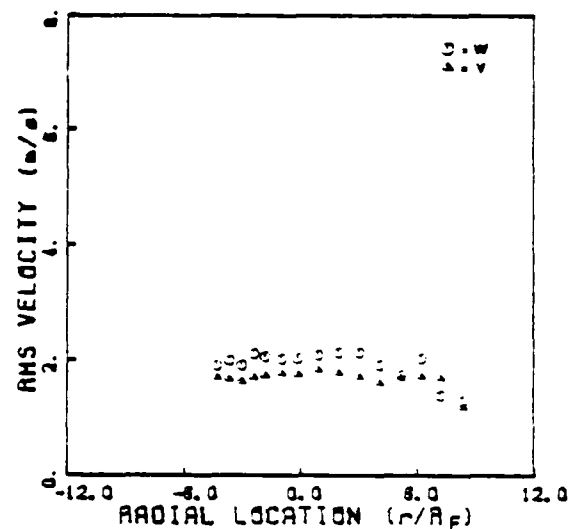
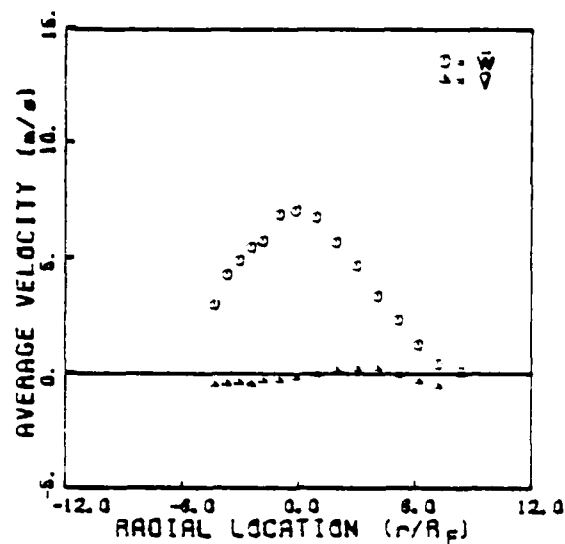


|         |     |
|---------|-----|
| $Z/D_F$ | 8.4 |
| FF      | 2   |
| AF      | 0   |



(c)

|         |      |
|---------|------|
| $Z/D_F$ | 20.9 |
| FF      | 2    |
| AF      | 0    |



(d)

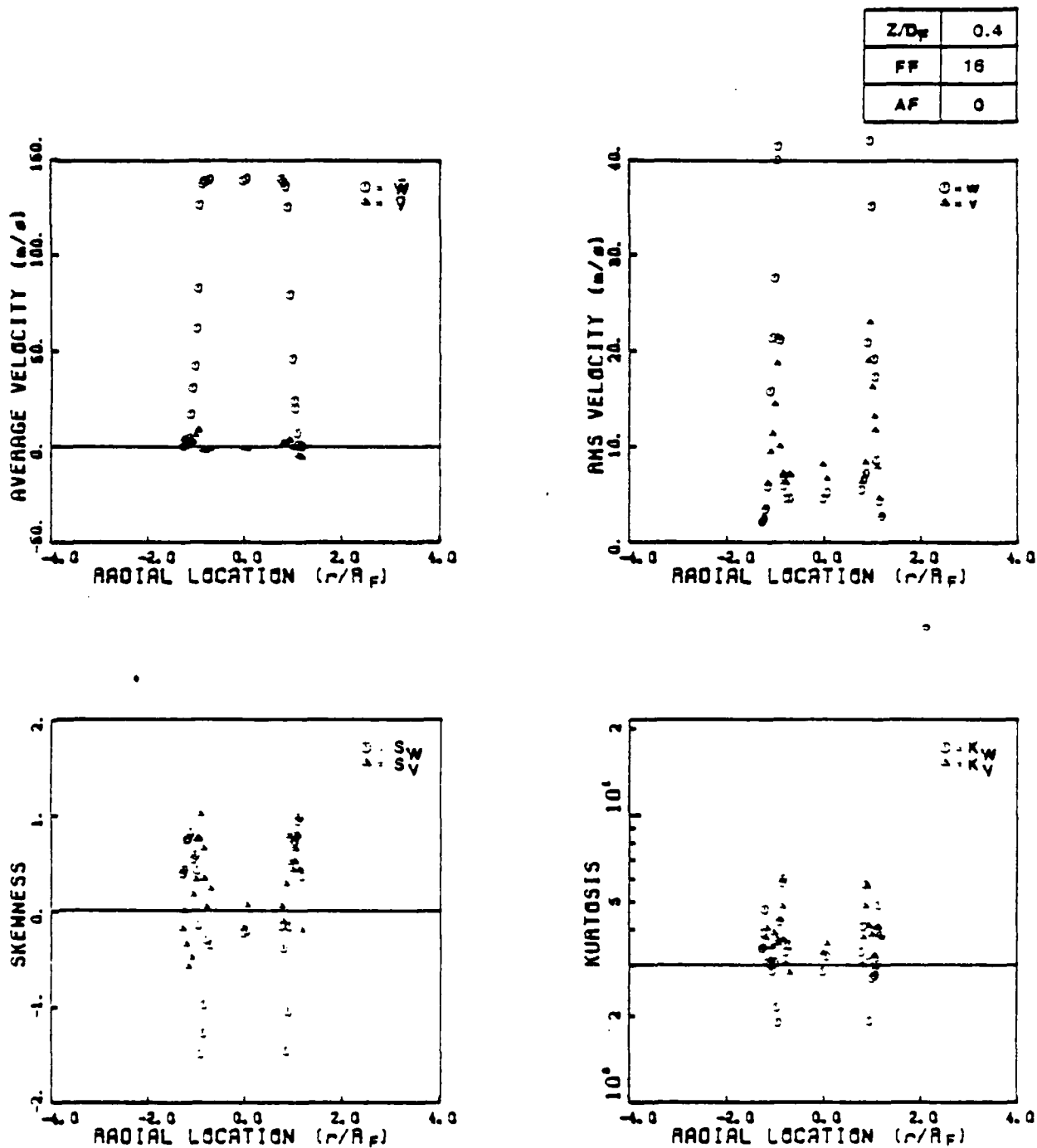
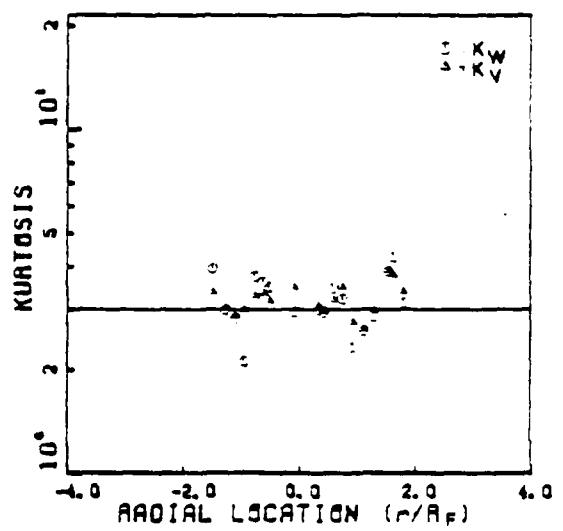
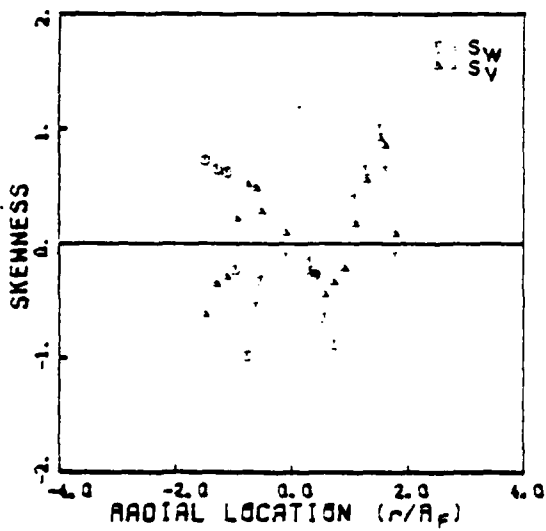
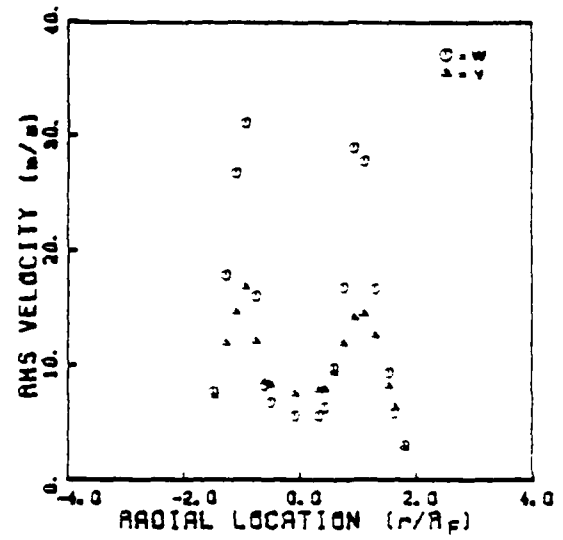
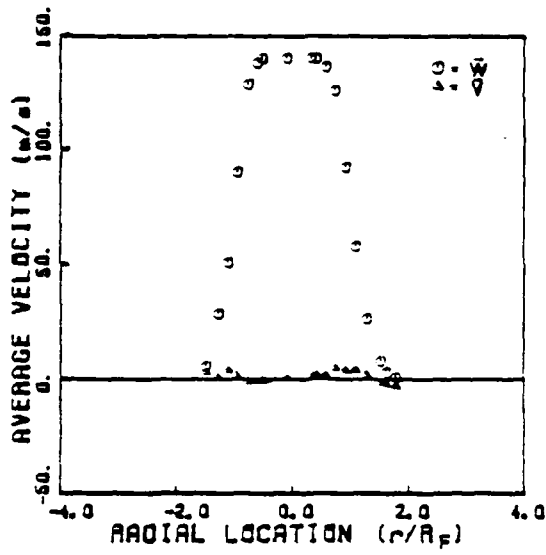


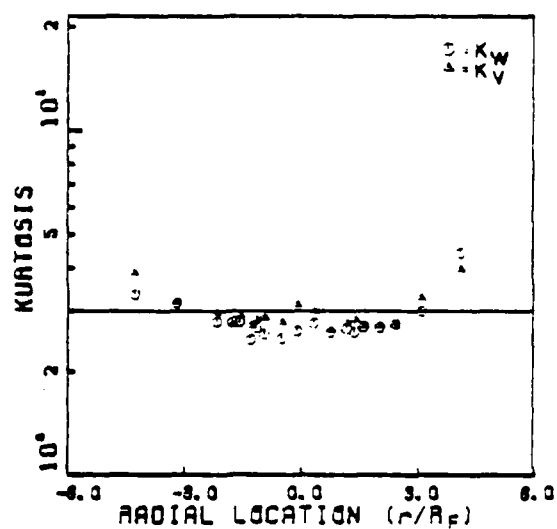
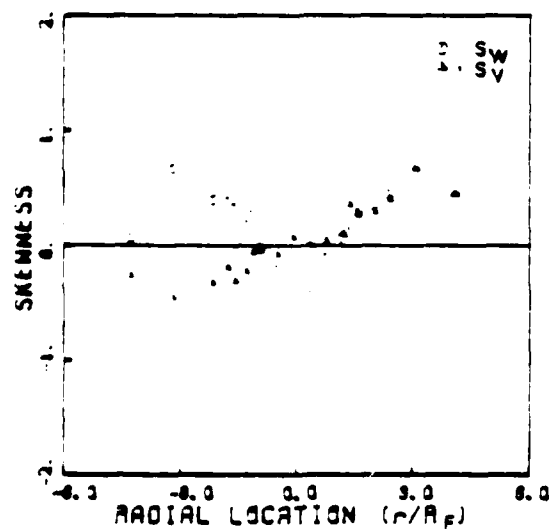
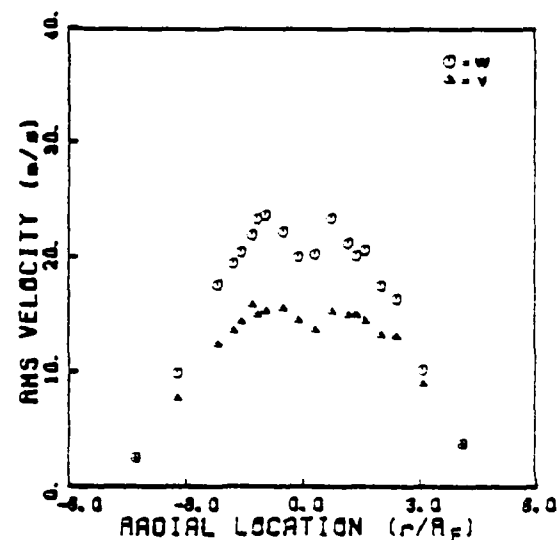
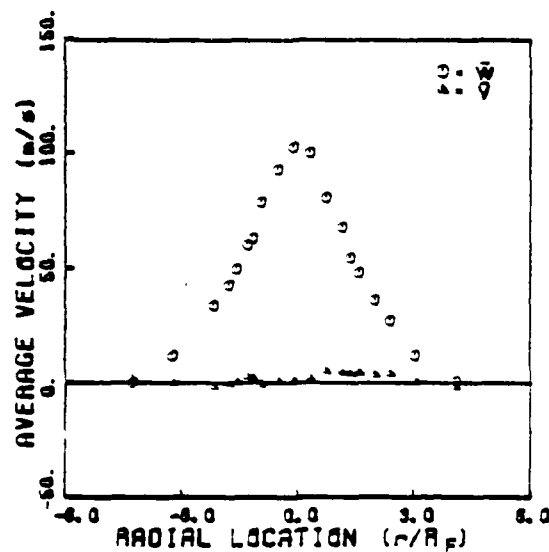
Figure 21. (a) - (f) Profiles of Velocity Distribution Descriptors Based Upon the First Four Moments. Measurements are for the central-jet-only condition with CO<sub>2</sub> mass flow of 16 kg/hr.

|         |     |
|---------|-----|
| $Z/D_F$ | 2.1 |
| FF      | 16  |
| AF      | 0   |



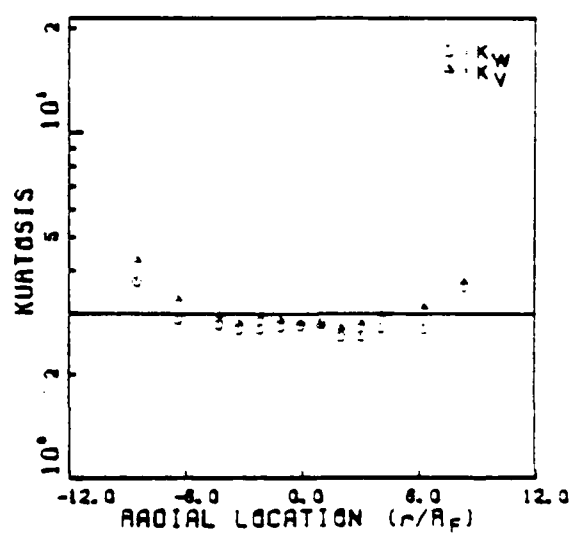
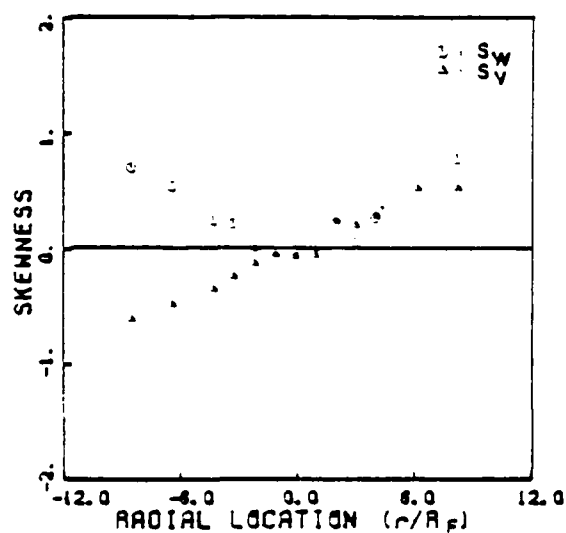
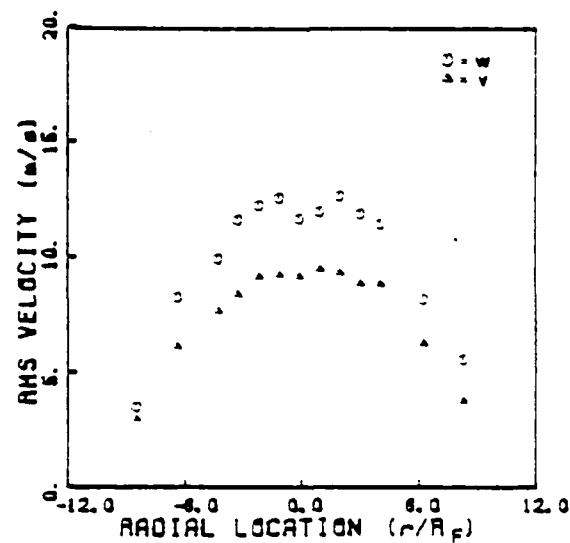
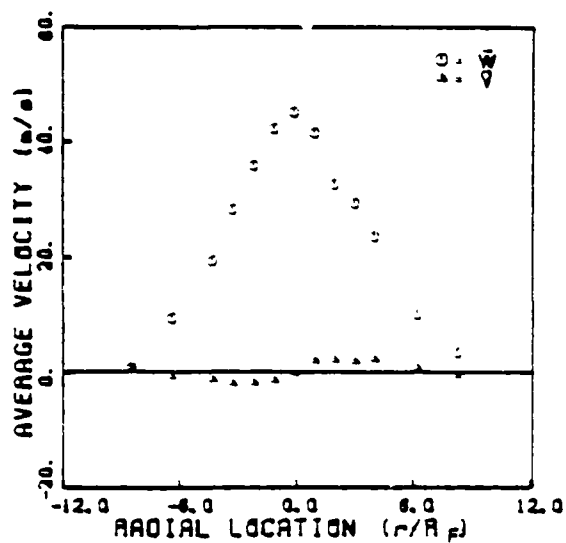
(b)

|                  |     |
|------------------|-----|
| Z/D <sub>F</sub> | 8.4 |
| FF               | 16  |
| AF               | 0   |



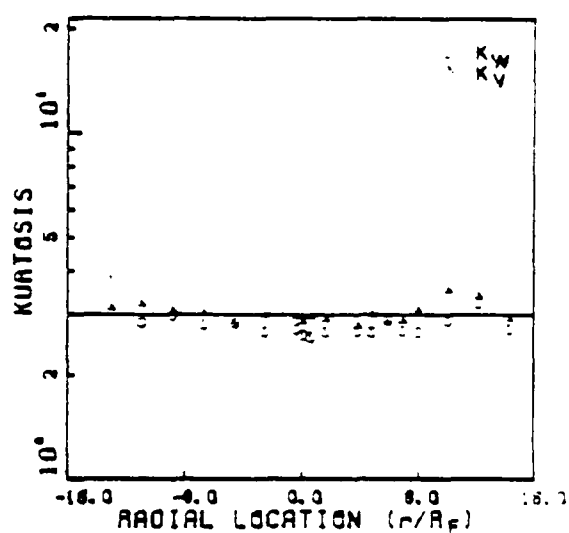
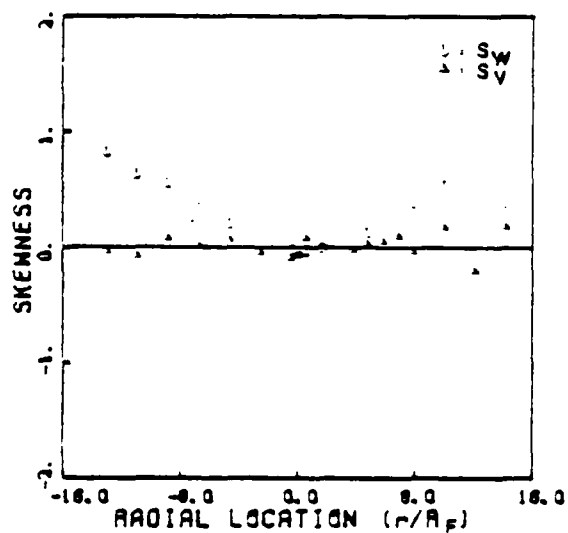
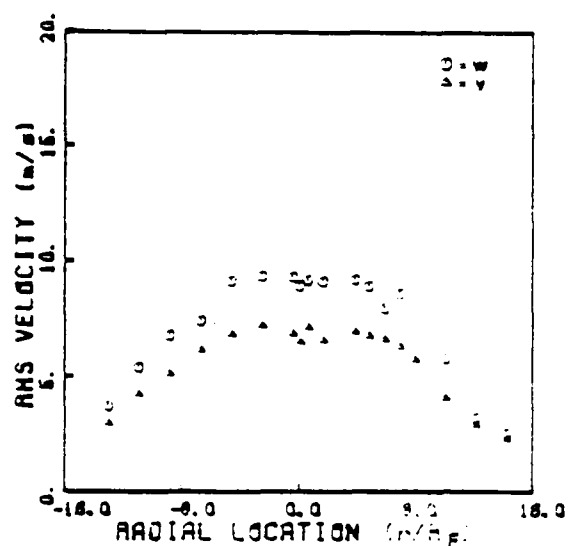
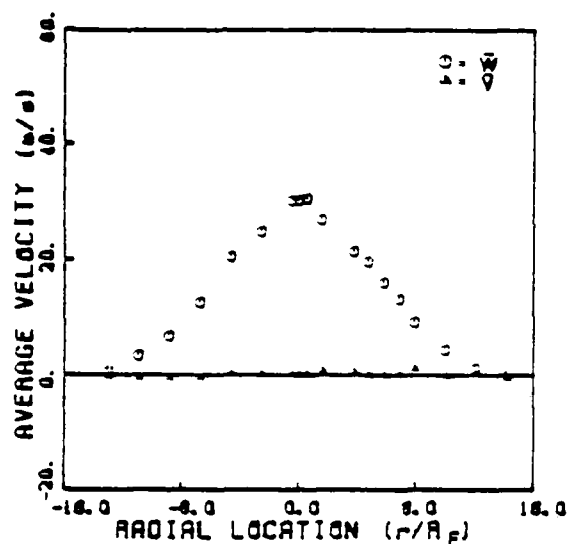
(c)

|                  |      |
|------------------|------|
| Z/D <sub>F</sub> | 20.9 |
| FF               | 16   |
| AF               | 0    |



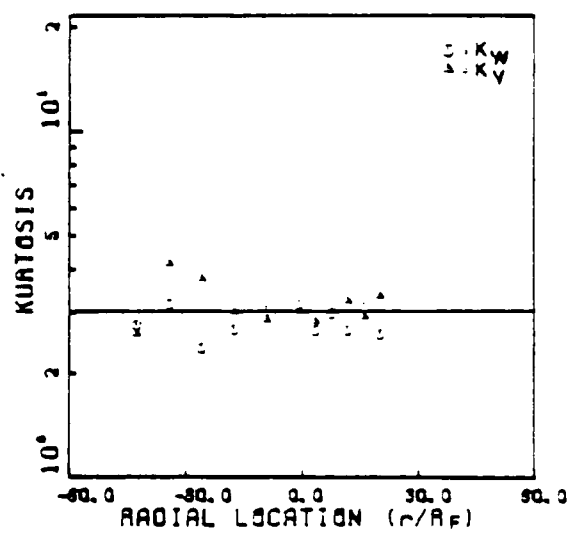
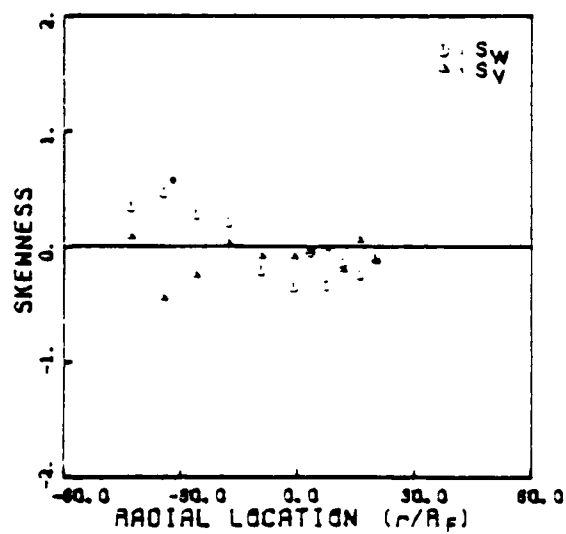
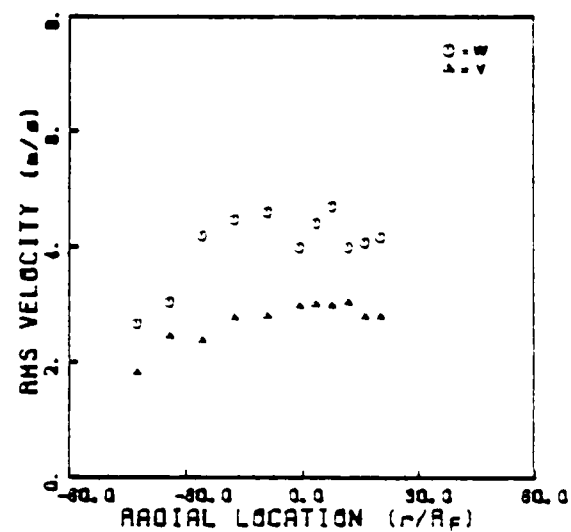
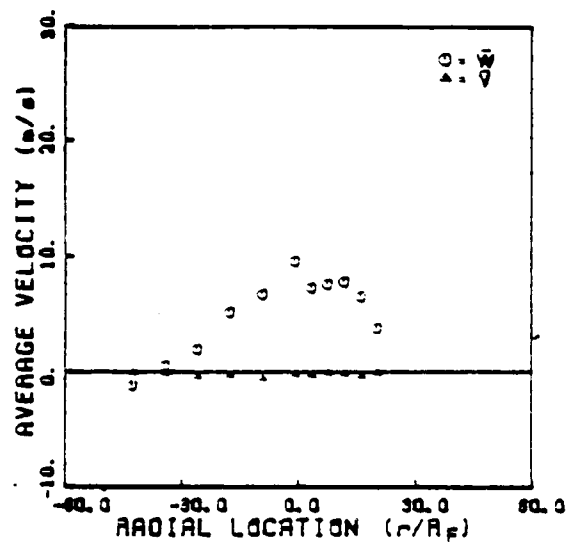
(d)

|                  |      |
|------------------|------|
| Z/D <sub>F</sub> | 29.3 |
| FF               | 16   |
| AF               | 0    |



(e)

|         |      |
|---------|------|
| $Z/D_F$ | 83.8 |
| FF      | 16   |
| AF      | 0    |



(f)



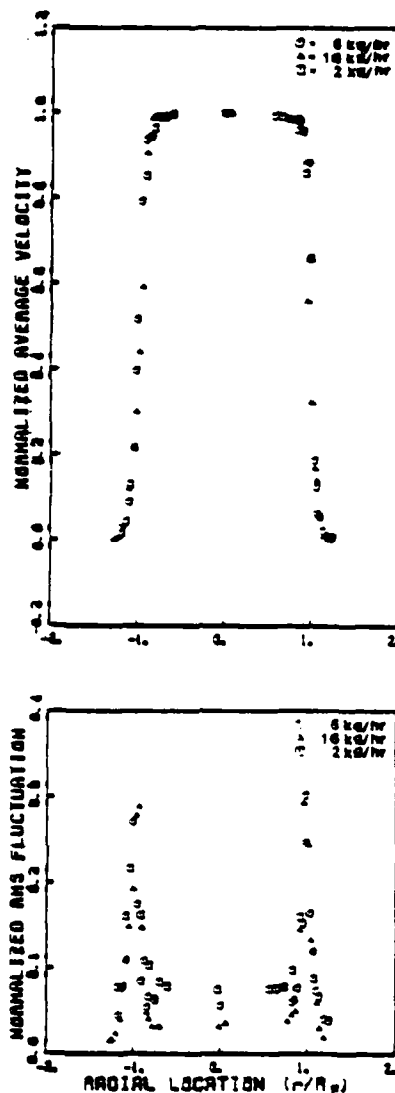
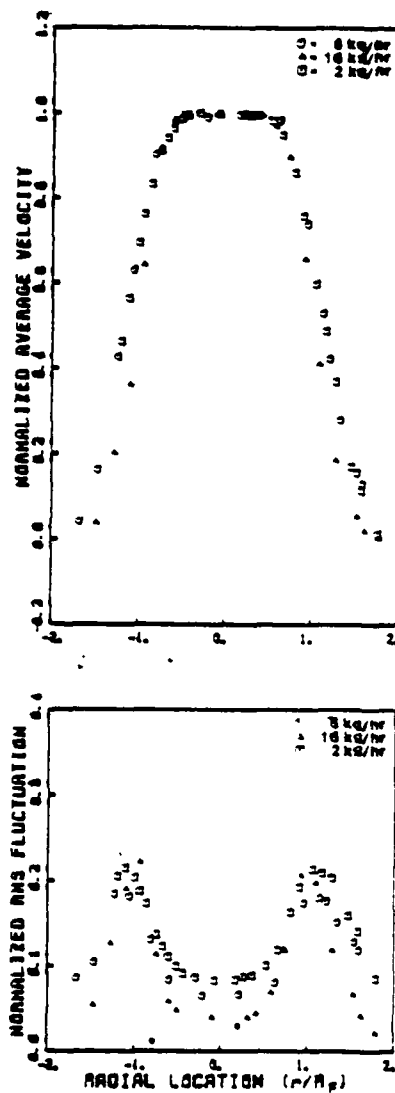
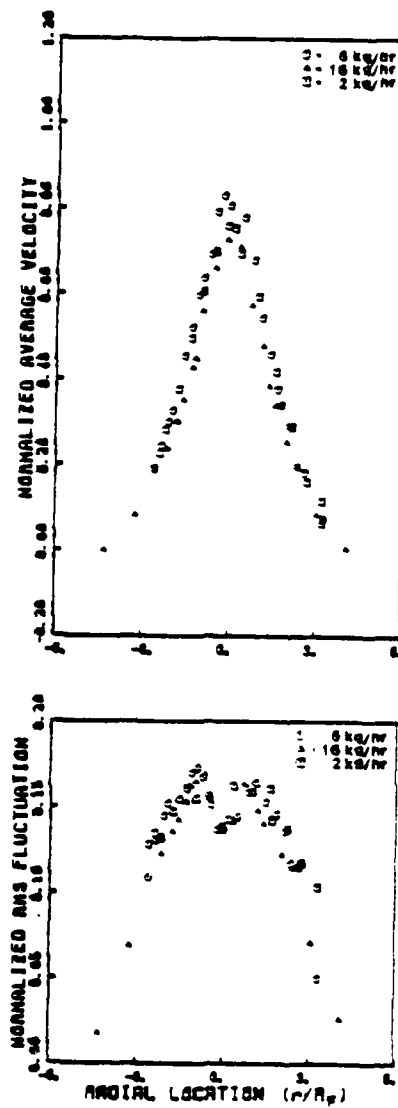


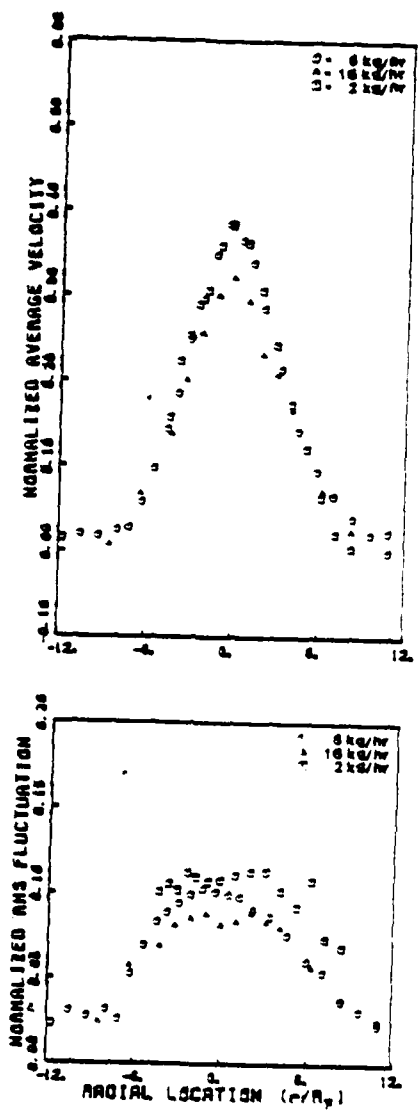
Figure 22. Overlays of the Normalized Average Axial-Velocity ( $\bar{w}_F/\bar{w}_{F0}$ ) and Normalized RMS Axial-Velocity Fluctuations ( $w/\bar{w}_{F0}$ ) for the Flow Conditions of 2, 6 and 16 kg/hr  $\text{CO}_2$ .  $\bar{w}_{F0}$  is the average central jet axial velocity at the entrance plane,  $\bar{w}_F$  is the average axial velocity at the measurement plane, and  $w$  is the average axial RMS fluctuation at the measurement plane. The profiles were measured at  $Z/D_F$ : (a) 0.4; (b) 2.1; (c) 3.4; and (d) 20.9.



(b)



(c)



(d)

identical at  $Z/D_F = 10.5$ , and only the axial component is different.

There are several possible mechanisms by which the measurements might be influenced. First, when taking LDA measurements the flow must be seeded. As a result, the seeded flow mixes with unseeded ambient air. In flow regions where the flow is intermittent, the measurements could be biased. This should show up in a time analysis of the velocity record, when such a study is made. To overcome the problem, it is necessary to prepare a stationary seeded ambient atmosphere, a difficult process at best. Second, the flow is being measured in a duct. At the farthest downstream stations ( $Z/D_F > 84$ ) the jet has spread to  $\phi_{1/2} > 0.30 D_D$ . As the profile broadens it will interact with the duct boundary layer flow and no longer be a simple jet. Third, the mixing and spreading of the jet are accompanied by entrainment of the surrounding fluid. This fluid comes from the duct and must be replenished by fluid drawn in from upstream of the bluff body. As this fluid slowly flows past the centerbody, large eddies might be shed which could influence the flow downstream. Other mechanisms for perturbing the flow undoubtedly exist.

The measurements shown do not clearly indicate that perturbations exist within the measurement region, as can be seen by the linear development of the profile width to  $Z/D_F = 105$  as expected. If perturbation does occur, the on-axis flow should show the effects least. Figure 23 is a plot of  $\bar{w}_O^F / \bar{w}_{O0}^F$  vs  $Z/D_C$ , the centerline velocity normalized to the issuing velocity as a function of downstream location, for the three flow rates studied. The form has the expected shape, a flat top in the potential core region, a transition region, and then a region that falls off as  $Z^{-1}$ . In the region  $Z/D_F > 30$ , the centerline velocity decays much faster than anticipated.

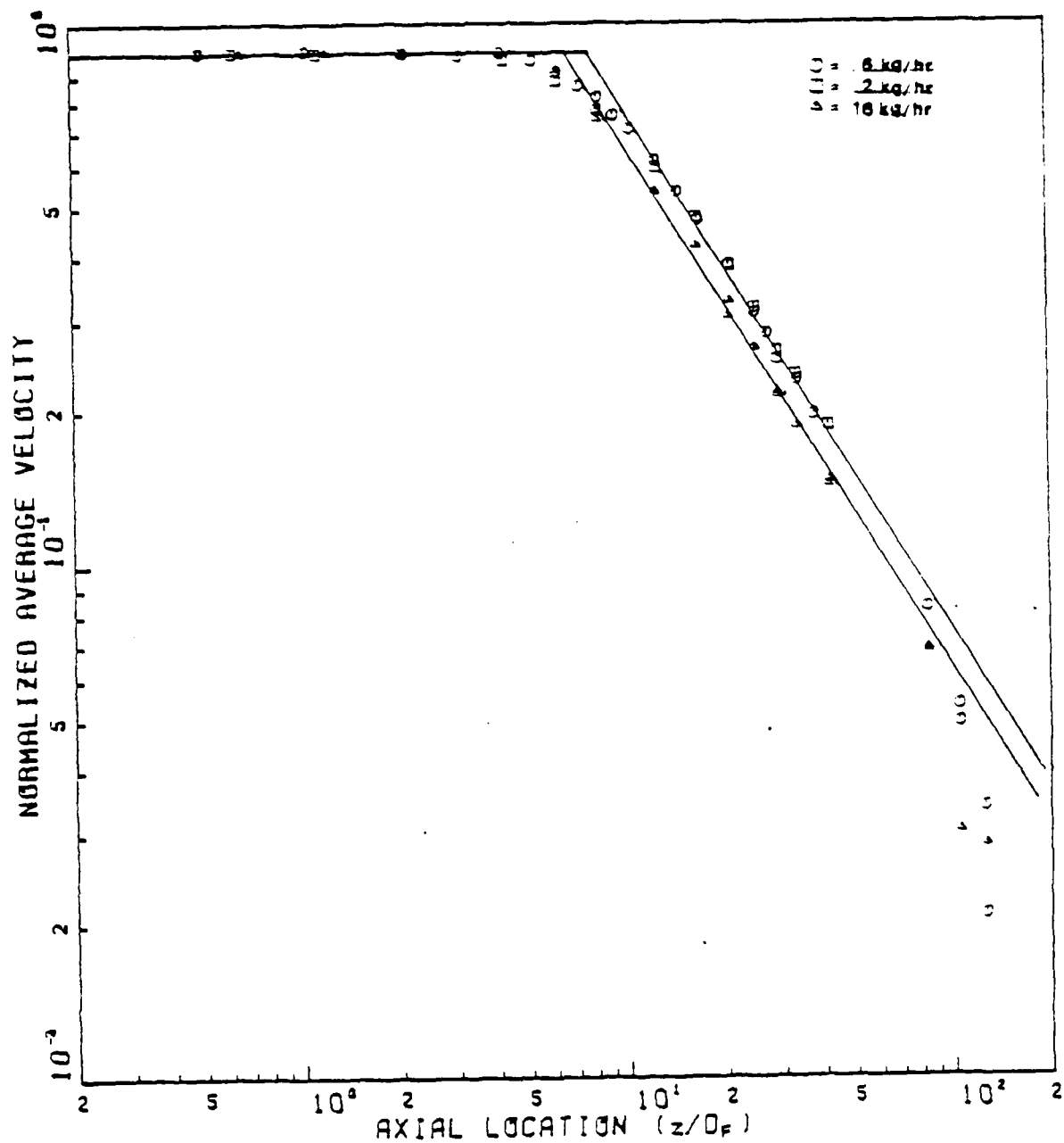


Figure 23. Dependence of Average Axial Centerline Velocity on Downstream Location. The centerline velocity has been normalized by the entrance velocity. The lines with slopes of -1 are drawn for illustration only.

The 16 kg/hr results show that the apparent  $Z^{-1}$  dependence occurs upstream of the 2 and 6 kg/hr velocity decay. This is in keeping with the profiles observed, shown in Figures 22(a) to (d) and discussed earlier. The  $Z^{-1}$  dependence region is usually described by the relation<sup>20</sup>

$$\frac{\bar{w}_O^F}{\bar{w}_{OO}^F} = A \frac{D_F}{Z+a} .$$

This is a first order approximation to the relation

$$\frac{\bar{w}_O^F}{\bar{w}_{OO}^F} = 1 - e^{-A \frac{D_F}{Z+a}}$$

and the simplification is only valid if  $Z+a/D_F \gg A$ . The apparent  $Z^{-1}$  dependence observed in Figure 23 is misleading. Fitting both forms to the data in the region  $Z/D_F > 12.6$  yields  $A = 7.5$  and  $a = -0.55 D_F$  for the linear approximation, and  $A = 6.8$  and  $a = -5.23 D_F$  for the exponential form. The change in the value of  $A$  is small but the shift in the virtual jet origin,  $a$ , is large. Both curves fit the data within the experimental uncertainties but it is clear that the criterion  $Z+a/D_F \gg A$  is not valid until  $Z/D_F > 70$ , beyond the region of measurement. Thus, the apparent  $Z^{-1}$  behavior is misleading and the linear approximation should not be used.

Experimentally determined values of  $A$  and  $a$  using the velocity decay data are shown in Table 4. Recall, the parameter  $a$  was also determined from the profile width data by Eq. (6),  $a = -4.8 D_F$ .

TABLE 4  
PARAMETERS DESCRIBING CENTERLINE VELOCITY DECAY

| A   | a/D <sub>F</sub> | $L < \frac{Z+a}{D_F} < U$ |    | REFERENCE |
|-----|------------------|---------------------------|----|-----------|
|     |                  | L                         | U  |           |
| 5.9 | -0.5             | 10                        | 50 | 22        |
| 5.9 | -3               | 10                        | 50 | 25        |
| 5.4 | -7               | 25                        | 90 | 25        |
| 7.5 | -6.5             | 15                        | 50 | 26        |
| 6.8 | -5.2             | 10                        | 80 | *         |
| 6.1 | -4.1             | 10                        | 80 | **        |

\* this study, Re = 11,000 and Re = 31,000

\*\* this study, Re = 83,000

The rms velocity fluctuations are plotted in Figure 24. They exhibit the expected behavior<sup>27</sup> rising to 25 to 30% turbulence intensity at  $Z/D_F \approx 30$  and holding constant farther downstream.

The velocity profiles, Figures 18, 20, and 21, were combined with the CO<sub>2</sub> concentration measurements of Bradley,<sup>19</sup> (see Appendix A) made under the same flow conditions. A numerical integration scheme was used to obtain the total mass flow within the profile, the mass flow of CO<sub>2</sub> within the profile, and the momentum flow. The results are shown in Figure 25, where the quantities plotted are (momentum flow)/(entrance velocity)<sup>2</sup>, (CO<sub>2</sub> mass flow)/(entrant mass flow), and (total mass flow)/(entrant mass flow). The particular normalization factor chosen for the momentum flow has no special significance. (It is equivalent to using mass flow.)



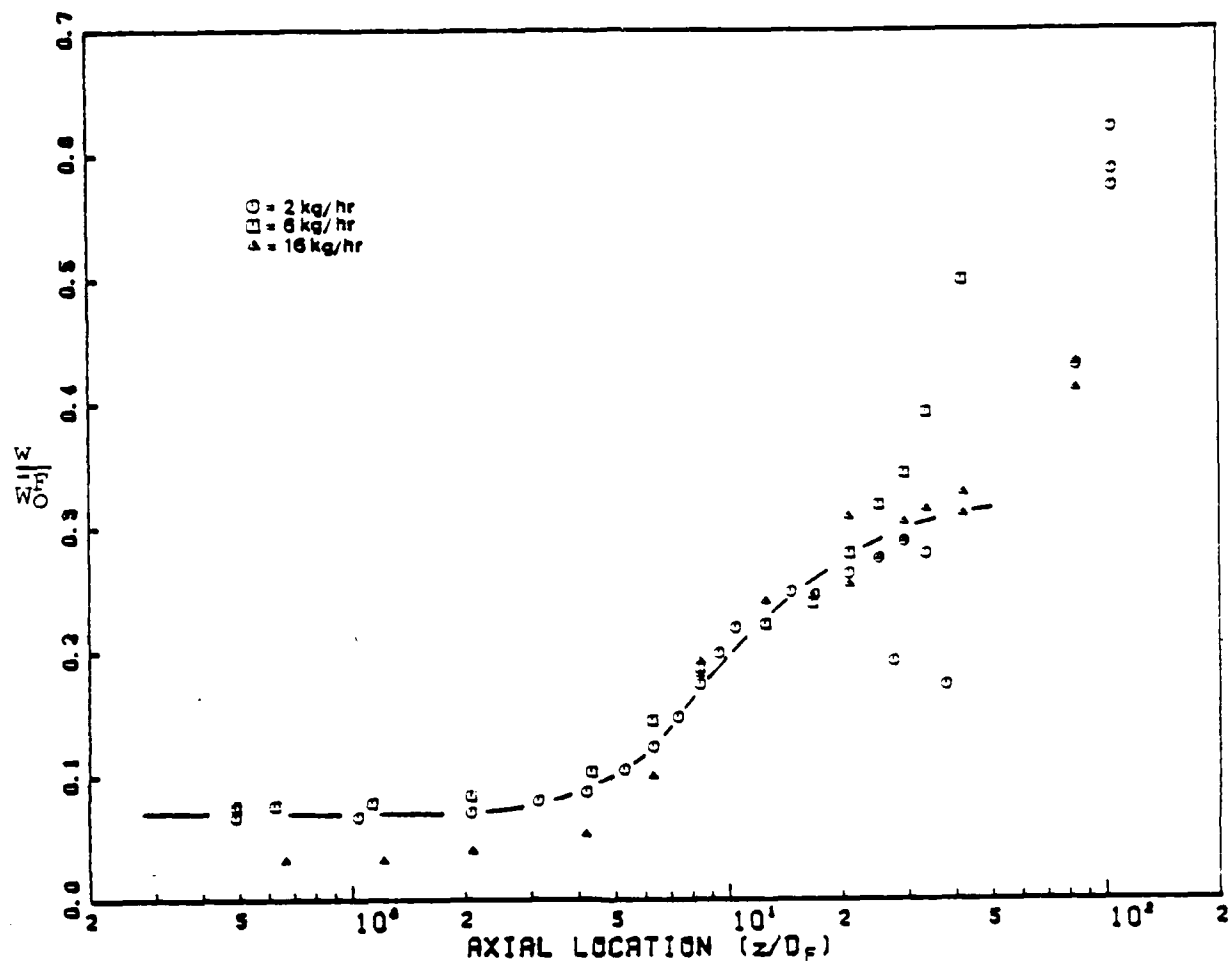


Figure 24. Variation of Local Axial RMS Turbulence Fluctuation as a Function of Downstream Location.

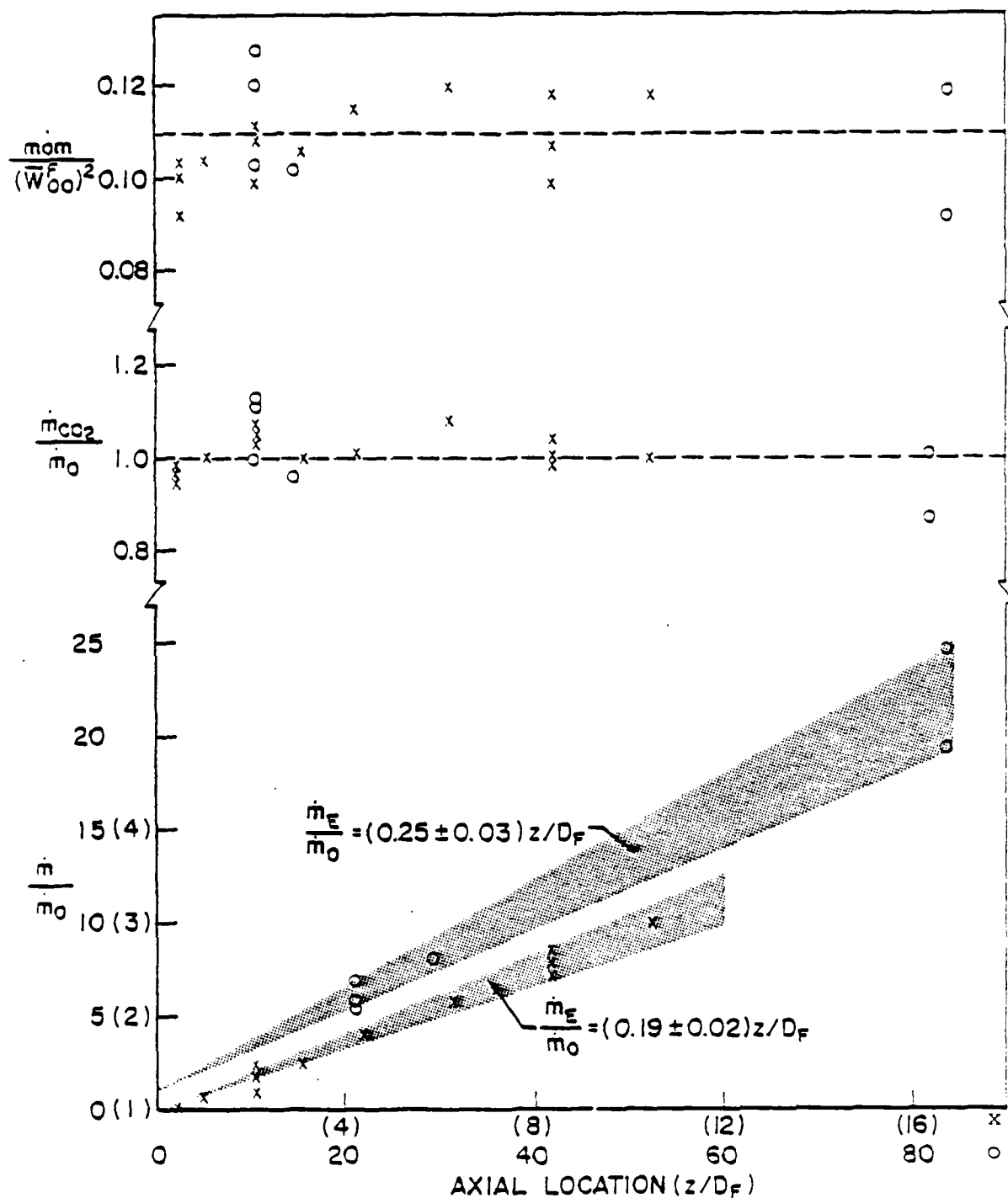


Figure 25. Total Mass as a Fraction of Entrance Mass at Each Downstream Measurement Station ( $\dot{m} = \dot{m}_0 + \dot{m}_E$ ). The data is for all three flow rates (2, 6, and 16 kg/hr  $CO_2$ ). The normalized  $CO_2$  mass flow and normalized total momentum flow at each station is shown to demonstrate the consistency of the results. The dashed lines are the expected values.

The plot of the total mass (normalized to the entrant mass) is divided into two regions. In the region from the entrance plane to  $Z/D_F \approx 10$  (plotted with the symbol x in Figure 25) the entrained mass grows linearly with the downstream distance, the rate of growth given by

$$\frac{\dot{m}_E}{\dot{m}_O} = (0.19 \pm 0.03) Z/D_F ,$$

and  $\dot{m} = \dot{m}_O + \dot{m}_E$  is the total mass flow. In the region  $Z/D_F > 20$  (plotted with the symbol o) the growth rate of the entrained mass is also linear but the rate has increased to

$$\frac{\dot{m}_E}{\dot{m}_O} = (0.25 \pm 0.03) Z/D_F .$$

Ricou and Spalding<sup>15</sup> defined a constant,  $C_2$ , describing the growth of the entrained mass which they found to be independent of the density of the jet

$$C_2 = \frac{\delta (\dot{m}_E/\dot{m}_O)}{\delta (Z/D_F)} \left( \frac{\rho_O}{\rho_S} \right)^{1/2} ,$$

where  $\rho_0$  is the jet density and  $\rho_s$  is the density of the gas into which the jet is flowing. Using this definition the experimental results obtained are

$$C_2 = 0.24 \pm 0.03 \quad Z/D_F < 10$$

$$= 0.32 \pm 0.04 \quad Z/D_F > 20$$

The far-downstream value corresponds to the result obtained by Ricou and Spalding<sup>15</sup> and Hill<sup>16</sup>. But, unlike Hill our results show a linear growth region near the entrance plane. Boguslawski and Popiel,<sup>18</sup> using hot-wire measurements of the velocity profile, also observed a constant value of  $C_2$  in the region  $0 < Z/D_F < 10$ , but their measurement yielded  $C_2 = 0.183$ , substantially lower than obtained here. Their study was for an air jet into air. Secondary checks and momentum flow were not presented in their paper. There may be a difference when a  $\text{CO}_2$  jet is used in this initial region of the flow development. In the far downstream region,  $25 < Z/D_F < 500$ , Ricou and Spalding found that  $C_2$  was independent of the jet gas, but this may not be true closer to the entrance.

It should be noted that in the earlier measurements of Ricou and Spalding<sup>15</sup> the value of  $C_2$  depended upon the Reynolds number of the flow, reaching its terminal value for  $Re > 25,000$ . The measurements being reported here spanned the range  $11,000 < Re < 83,000$ . No consistent dependence upon  $Re$  was observed.

The validity of the measurements was checked in two ways. First, the mass flow of  $\text{CO}_2$  in the jet should be constant at each downstream station. Figure 25 shows that at every downstream location the  $\text{CO}_2$  mass flow in the jet is the same as the  $\text{CO}_2$  jet entrance mass flow to within  $\pm 5\%$ , even though the total mass has grown more than 20 fold. Second, momentum should be conserved for the jet. The momentum divided by the entrant velocity squared is plotted in Figure 25. The normalization chosen has no special significance other than it reduces the measurements to a

common value, for the nozzle used, independent of mass flow. (For more generality a density factor should also be used.) The results for the three mass flows used, are shown in Figure 25. The momentum is constant to within  $\pm 10\%$  throughout the measurement region.

The consistency checks made on the measurements have shown that the velocity profiles are accurate throughout the measurement region. Therefore, the entrainment measurements should also be accurate. They indicate that the entrainment changes notably when the jet is in the transition region of its development (see Fig. 17).

## SECTION 4

### ANNULAR FLOW

The annular jet flowfield provides the numerical models with a substantive test for evaluating their effectiveness. A recirculation vortex is established in the wake of the bluff body (Figure 2) and the reverse flow on centerline opposes any flow from the central jet. The flowfield was measured with an annular flow rate of 2 kg/s of air and with central jet flows of 0 and 6 kg/hr of CO<sub>2</sub>. The initial results reported are for the case with no central jet flow. The addition of the central jet produced a localized change in the flowfield which did not extend far downstream. A detailed study of the perturbation is reported next.

#### 4.1 EXPERIMENTAL PROCEDURE

The flowfield was measured using the LDA instrument previously described. The annular jet and central jet are seeded independently, and care must be taken to match the seeding densities as closely as possible.

The experimental procedure for measuring the flowfield consists of: first, scanning the flowfield in the X direction at Y=0 (see Figure 1); second, taking measurements in the Y direction at X=0 to the limit of the window (at Y=20 mm); and, last, scanning the flowfield in the X direction at Y=20 mm (Fig. 26). The first scan provides the axial and azimuthal velocity components. The scans are taken from one side of centerline, through centerline to the window on the other side. The scan region around centerline permits checking of the flow symmetry. The second scan gives the axial and radial velocity components. The third scan determines the axial velocity and a combination of the radial and azimuthal components (Fig. 26). Assuming that the average flowfield is stationary and that the average azimuthal velocities are known from the first scan, the

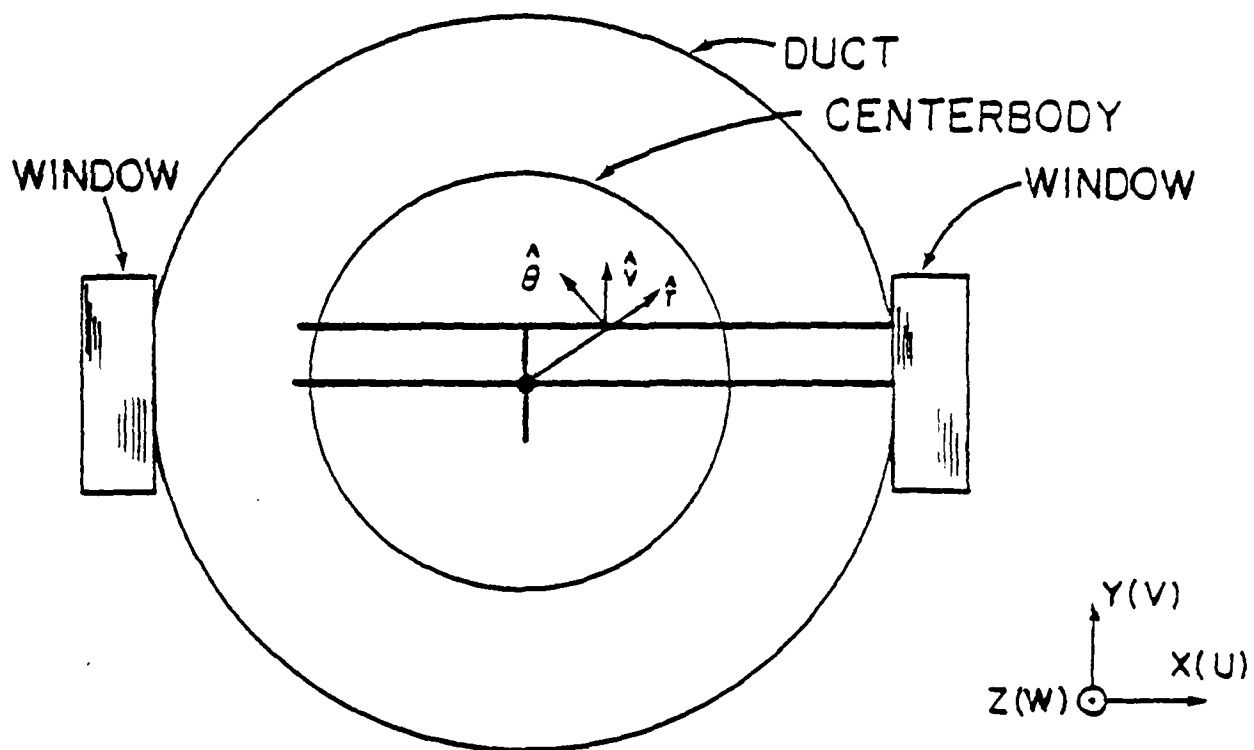


Figure 26. On-Axis View of APL Combustor Showing the Three Scan Profiles Taken at the Axial Stations. The LDA measures  $v$  and  $w$  components.

radial component can be obtained from the combined measurement by the decomposition given in Eqs. (8a) to (8c).

$$R = \sqrt{X^2 + 4} \quad (8a)$$

$$\theta = \tan^{-1}(2/X) \quad (8b)$$

$$V_R = (\sin \theta)^{-1} (V - V_\theta \cos \theta). \quad (8c)$$

where  $(R, \theta)$  are the cylindrical coordinates of the measurement location at  $(X, 2)$  in cartesian coordinates,  $V_R, V_\theta$  are the radial and azimuthal velocity components, and  $V$  is the velocity component in the  $Y$  direction.

#### 4.2 RESULTS

The measurements taken at  $Y=0$  are shown in Figures 27(a) to (n). The measurements were made at locations  $0 < Z/D_c < 4.29$ , where  $D_c$  is the centerbody diameter, 140 mm. The edge of the centerbody occurred at  $r/R_F = 29.3$ . The relatively flat entrance profile of the annular jet is seen in Figure 27(a). The rms velocity fluctuations are uniform until the centerbody boundary layer is entered, and then they increase to four times the value in the annulus. As the measurements proceed downstream, the recirculation zone increases in strength, the rms fluctuations in the recirculation zone increase, and the fluctuations in the shear layer diminish. This process continues until at  $Z/D_c = 0.29$  the shear layer is not distinguishable from the recirculating flow on the basis of the fluctuating component.

In the region  $Z/D_c \approx 0.86$  the fluctuating components have reached their maximum. Further downstream the axial fluctuation falls faster than the azimuthal fluctuation and this remains the case to the end of the first window's observations at  $Z/D_c = 1.43$ . In the second window the velocity profile is approaching a flat-top profile and the fluctuating components are equal for the two directions measured.



|         |     |
|---------|-----|
| $Z/D_c$ | 0.0 |
| FF      | 0   |
| AF      | 2   |

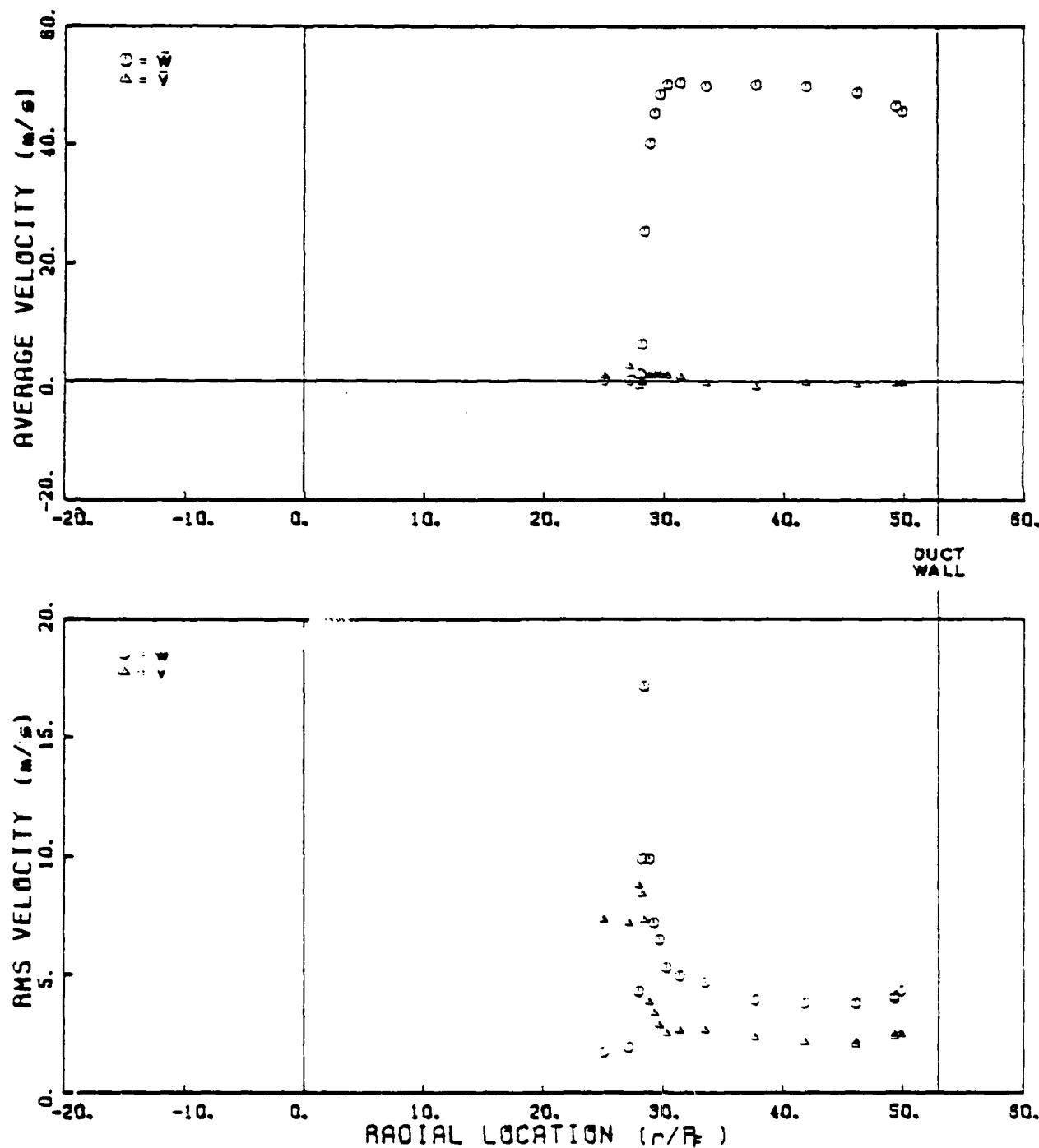
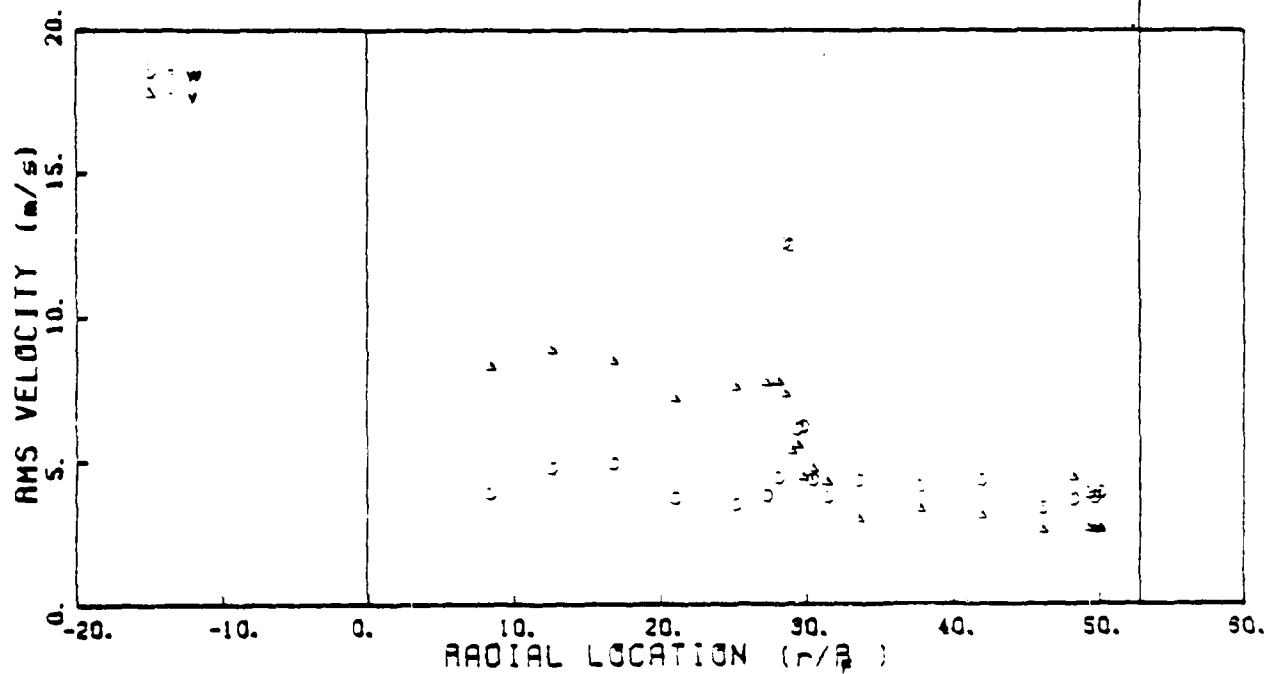
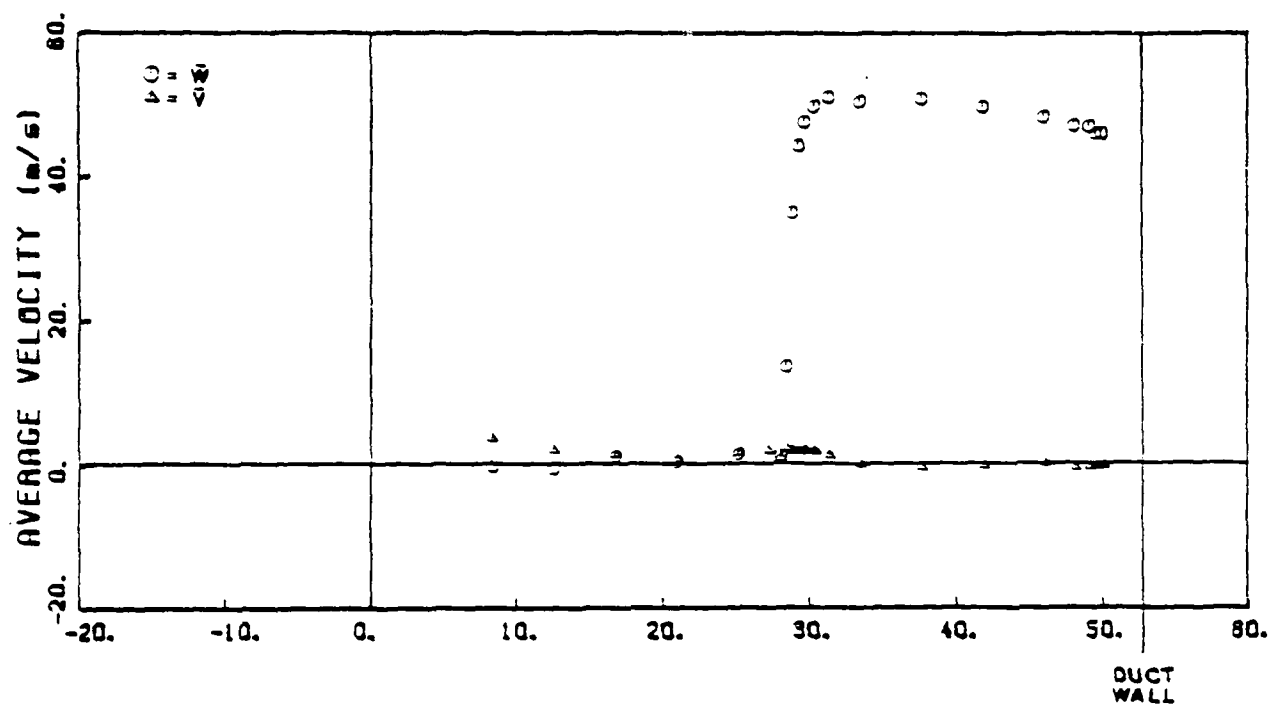


Figure 27. (a) - (n) Radial Profiles of the Average Axial- and Azimuthal-Velocity and Average Axial- and Azimuthal-RMS Velocity Fluctuations for Annular-Jet-Only Flow of 2 kg/s Air. The downstream location is given for each profile at the top of the page.

|         |      |
|---------|------|
| $Z/D_c$ | 0.01 |
| FF      | 0    |
| AF      | 2    |



(b)

AD-A134 691

LASER DIAGNOSTIC DEVELOPMENT AND MEASUREMENT AND  
MODELING OF TURBULENT FL. (U) DAYTON UNIV OH RESEARCH  
INST A J LIGHTMAN ET AL JUN 83 UDR-TR-83-22

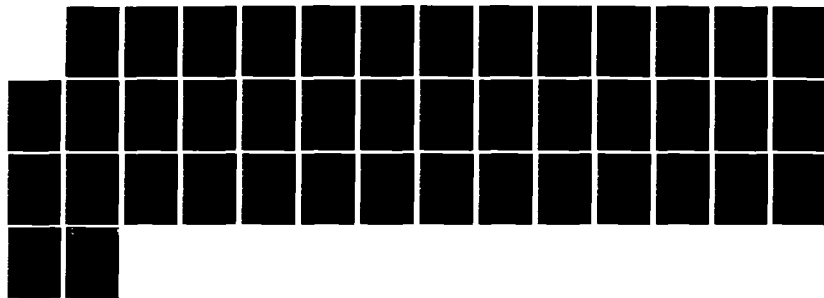
2/2

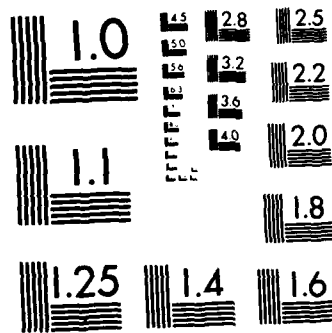
UNCLASSIFIED

AFWAL-TR-83-2044-PT-1 F33615-78-C-2005

F/G 20/4

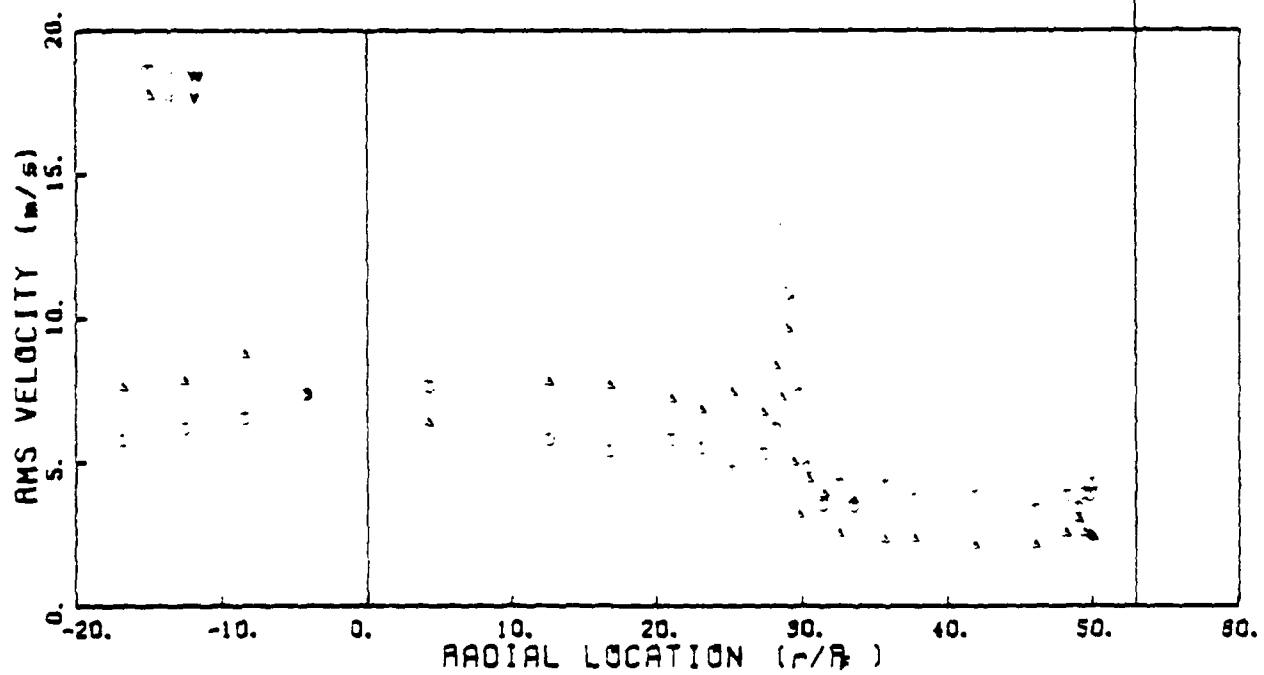
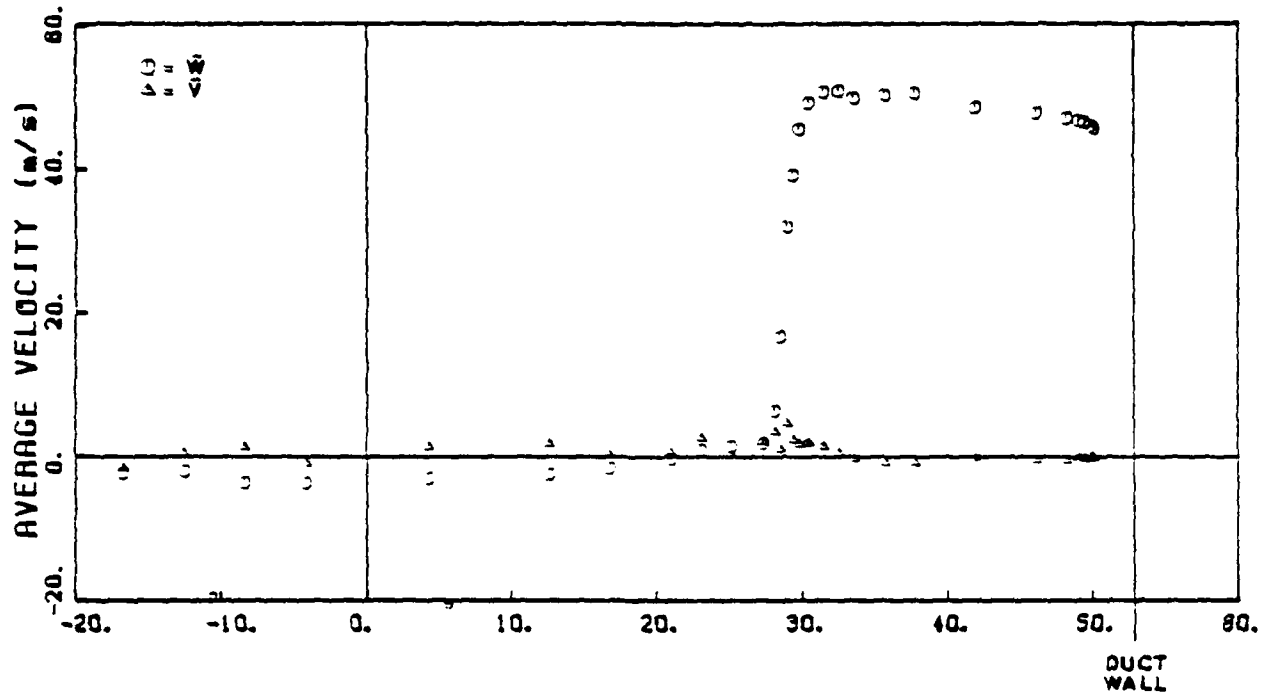
NL





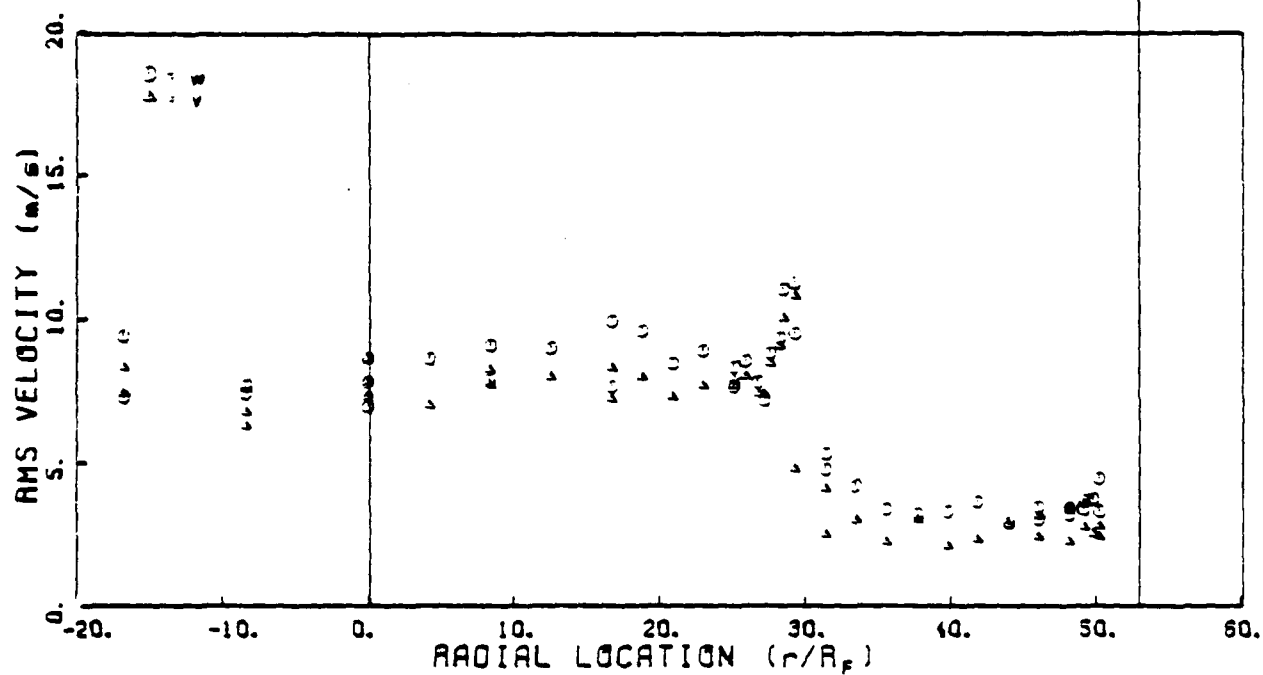
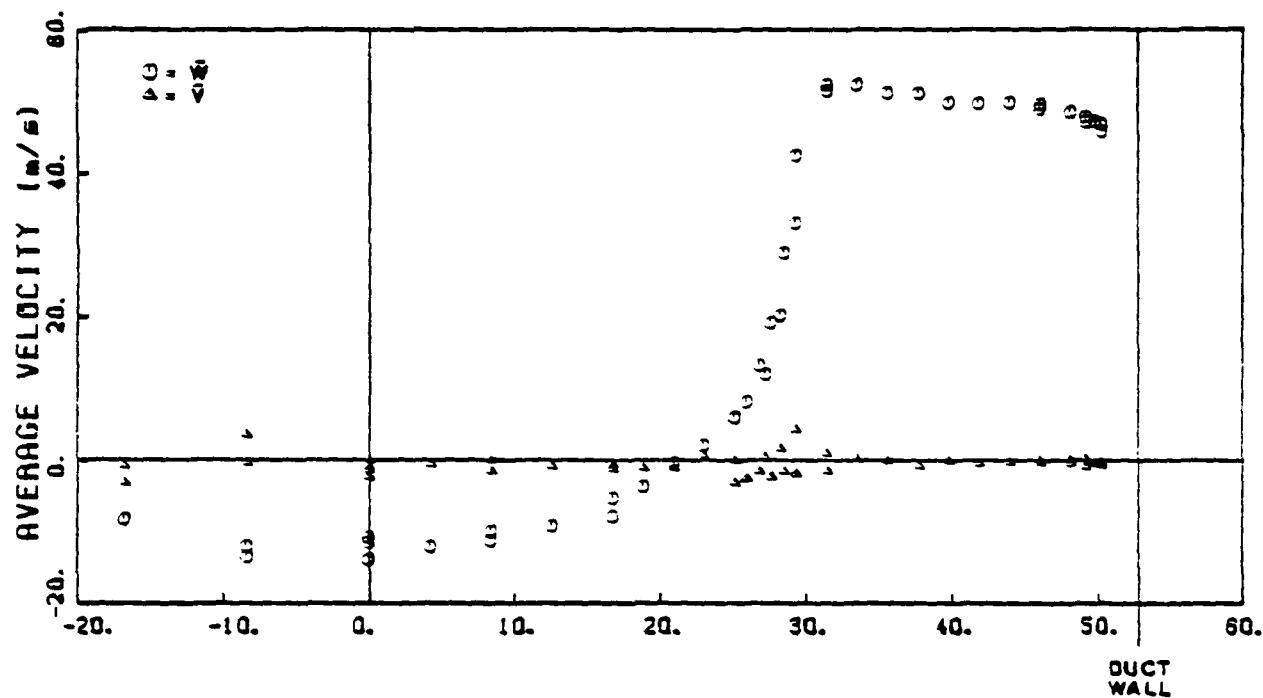
MICROCOPY RESOLUTION TEST CHART  
NATIONAL BUREAU OF STANDARDS-1963-A

|         |      |
|---------|------|
| $Z/D_c$ | 0.04 |
| FF      | 0    |
| AP      | 2    |



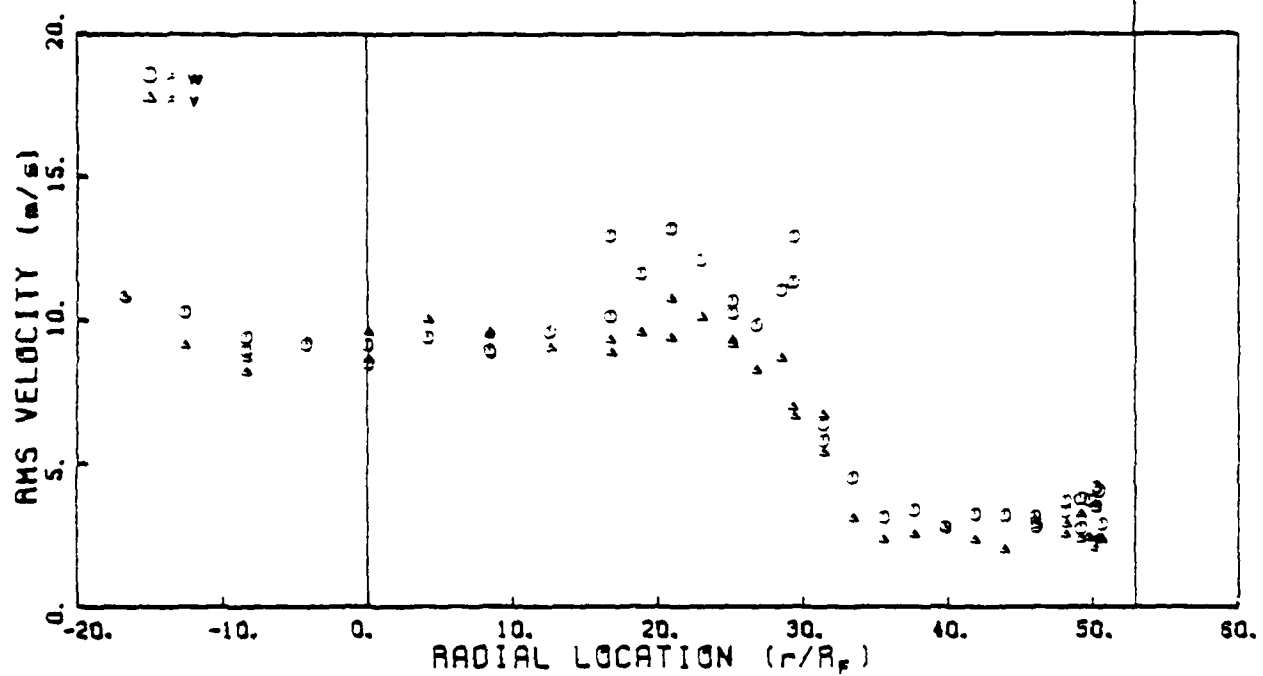
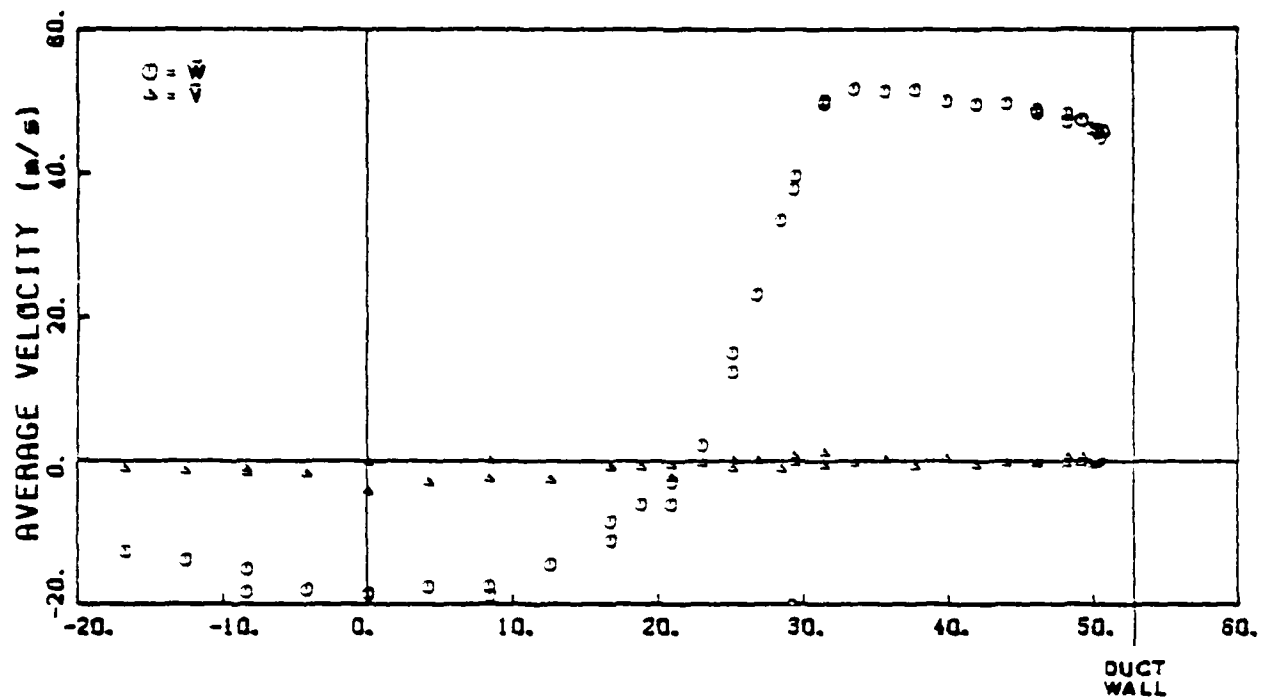
(c)

|         |      |
|---------|------|
| $Z/D_C$ | 0.14 |
| FF      | 0    |
| AF      | 2    |



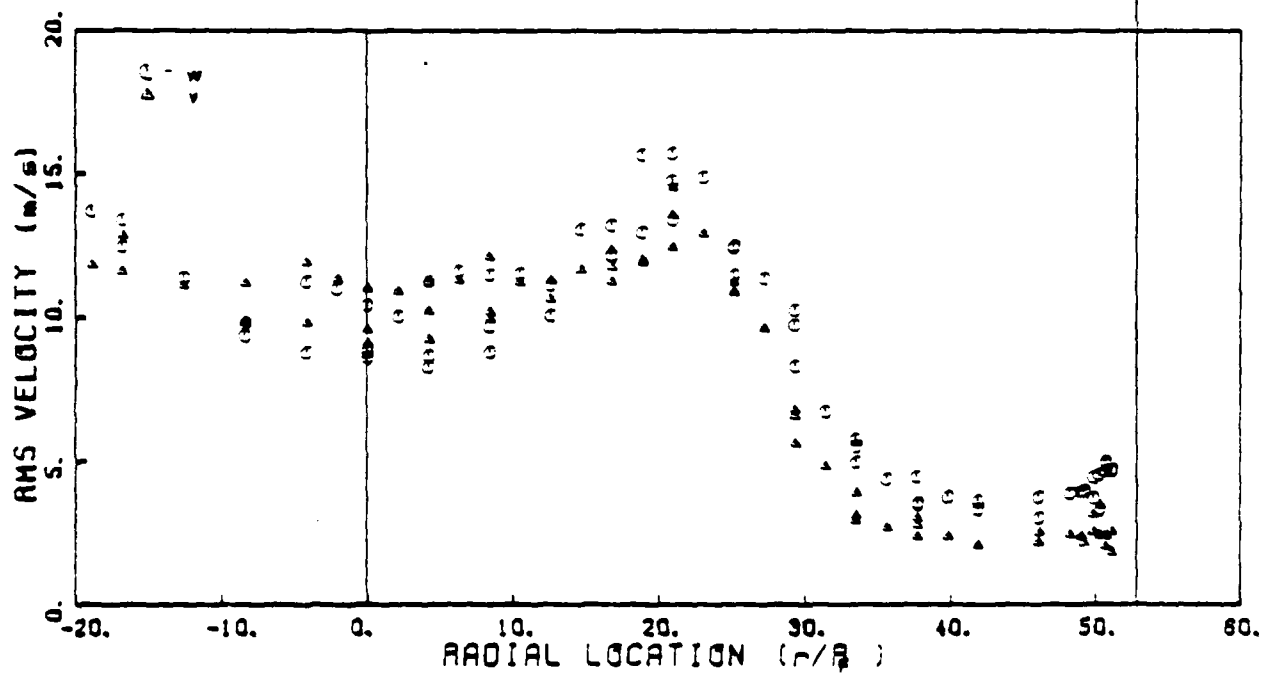
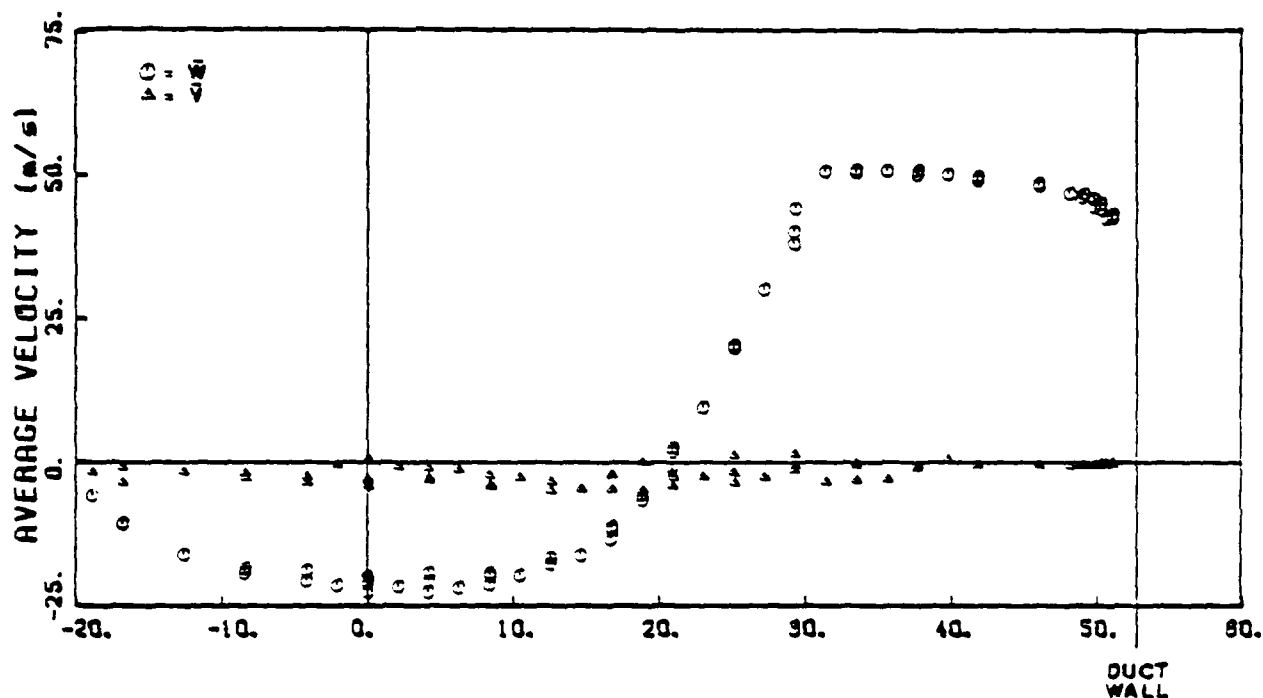
(d)

|         |      |
|---------|------|
| $Z/D_c$ | 0.29 |
| FF      | 0    |
| AF      | 2    |



(e)

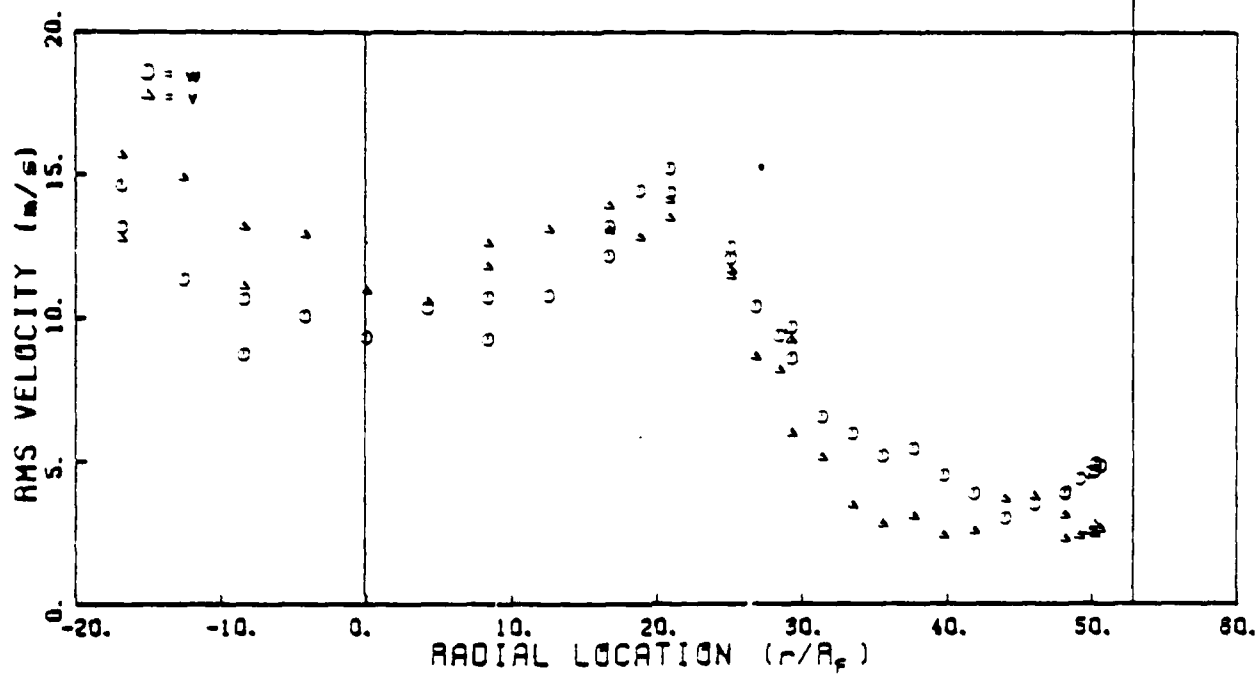
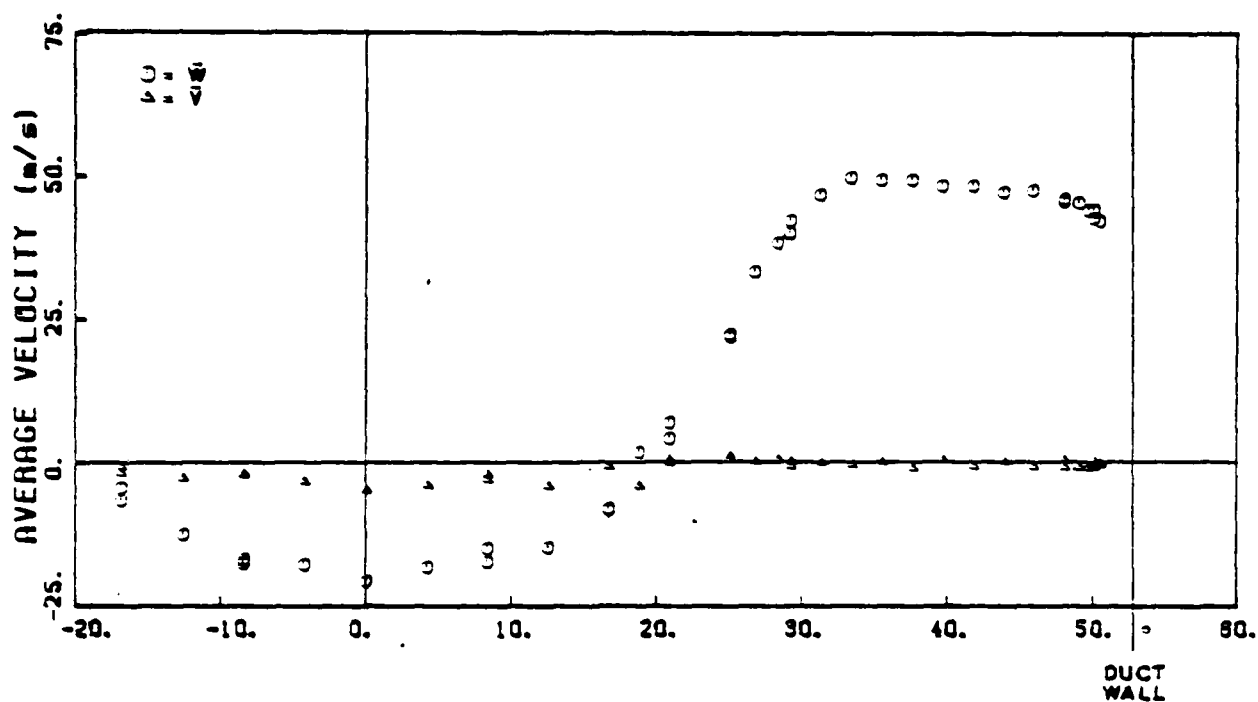
|         |      |
|---------|------|
| $Z/D_c$ | 0.43 |
| FF      | 0    |
| AF      | 2    |



(f)

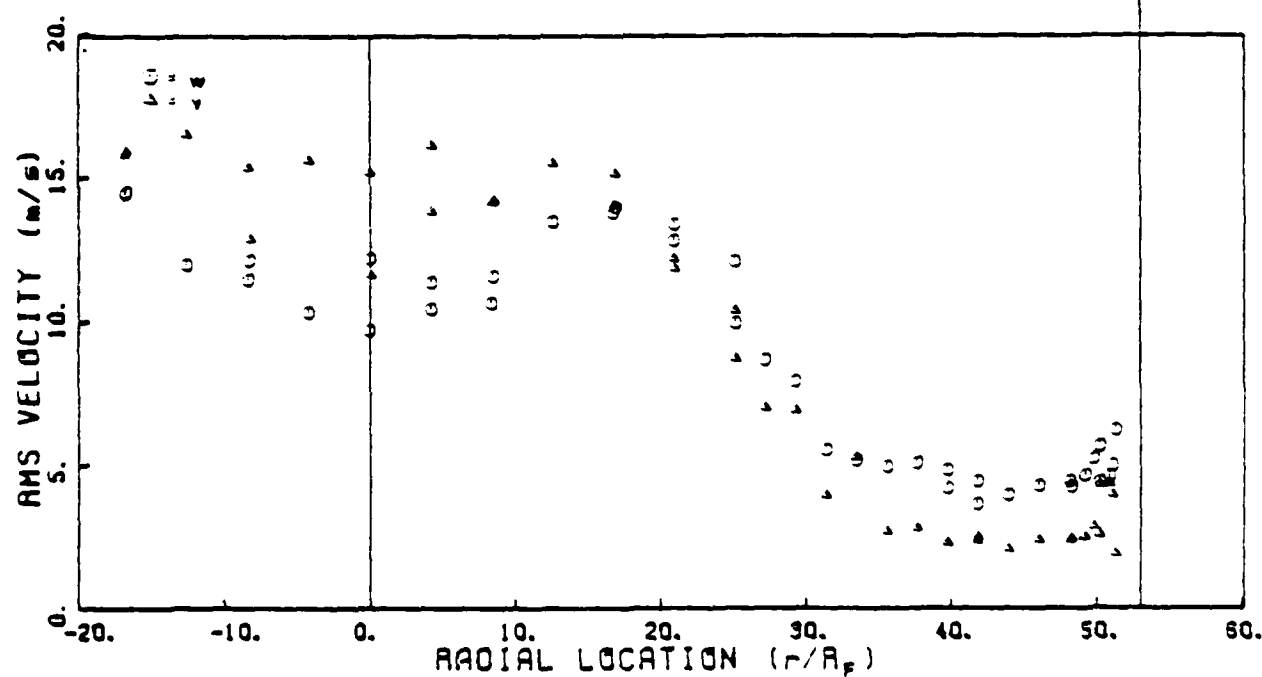
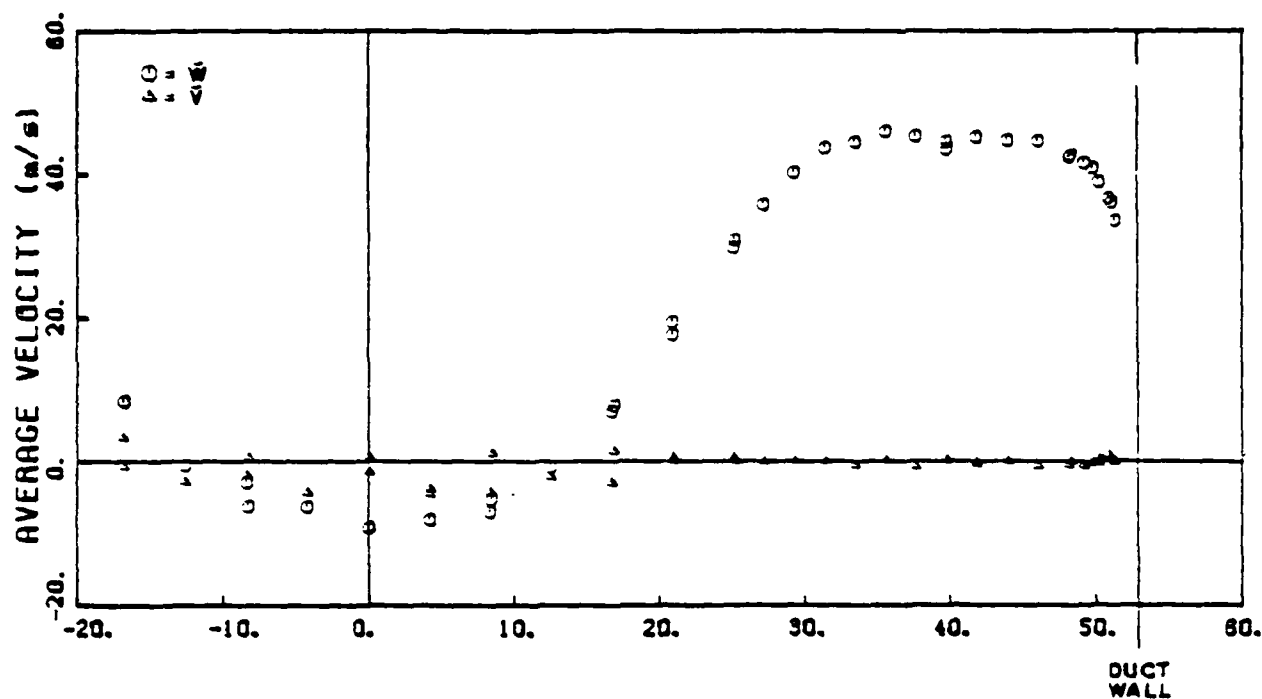


|         |      |
|---------|------|
| $Z/D_c$ | 0.57 |
| FF      | 0    |
| AF      | 2    |



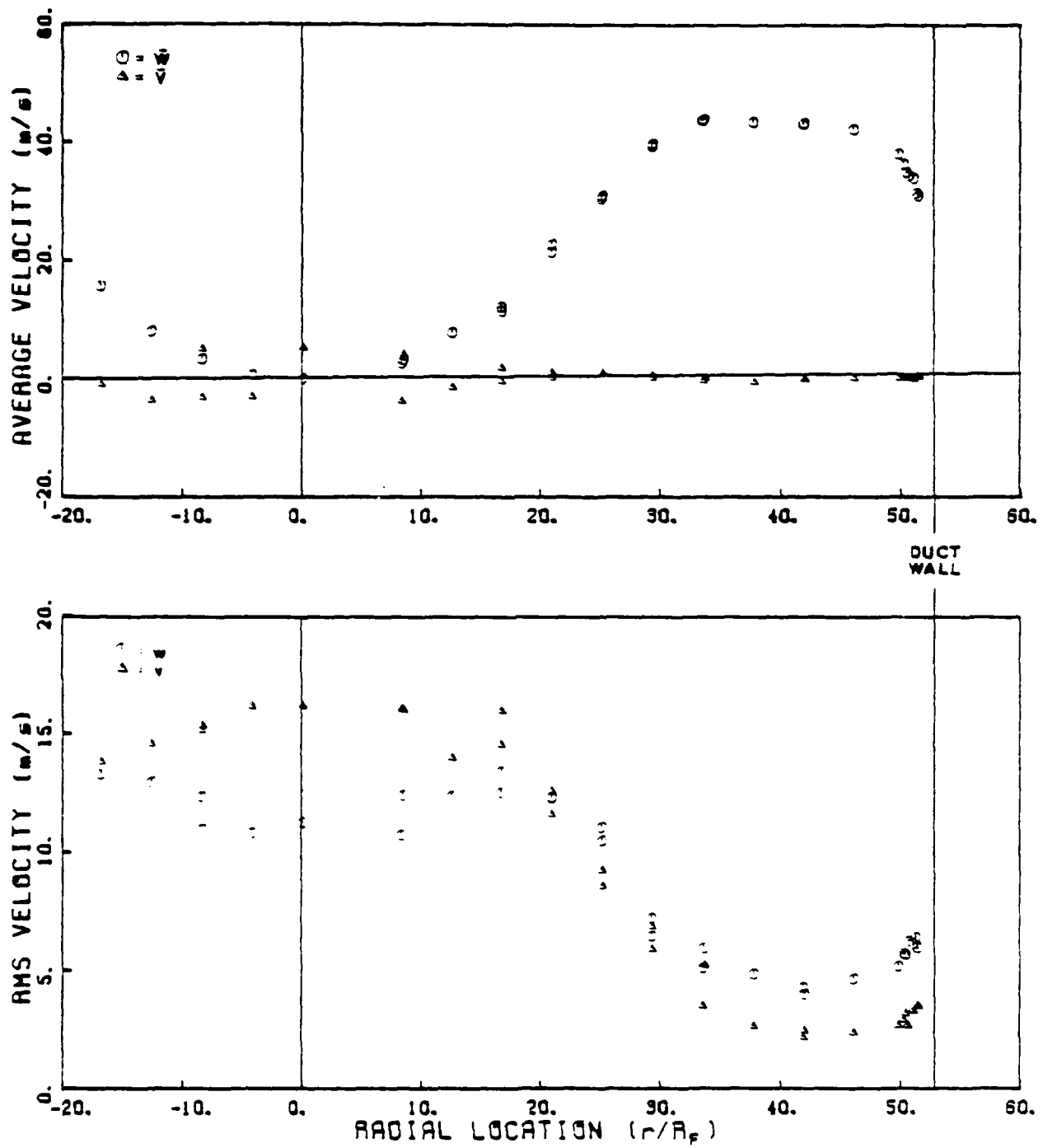
(g)

|         |      |
|---------|------|
| $Z/D_c$ | 0.86 |
| FF      | 0    |
| AF      | 2    |



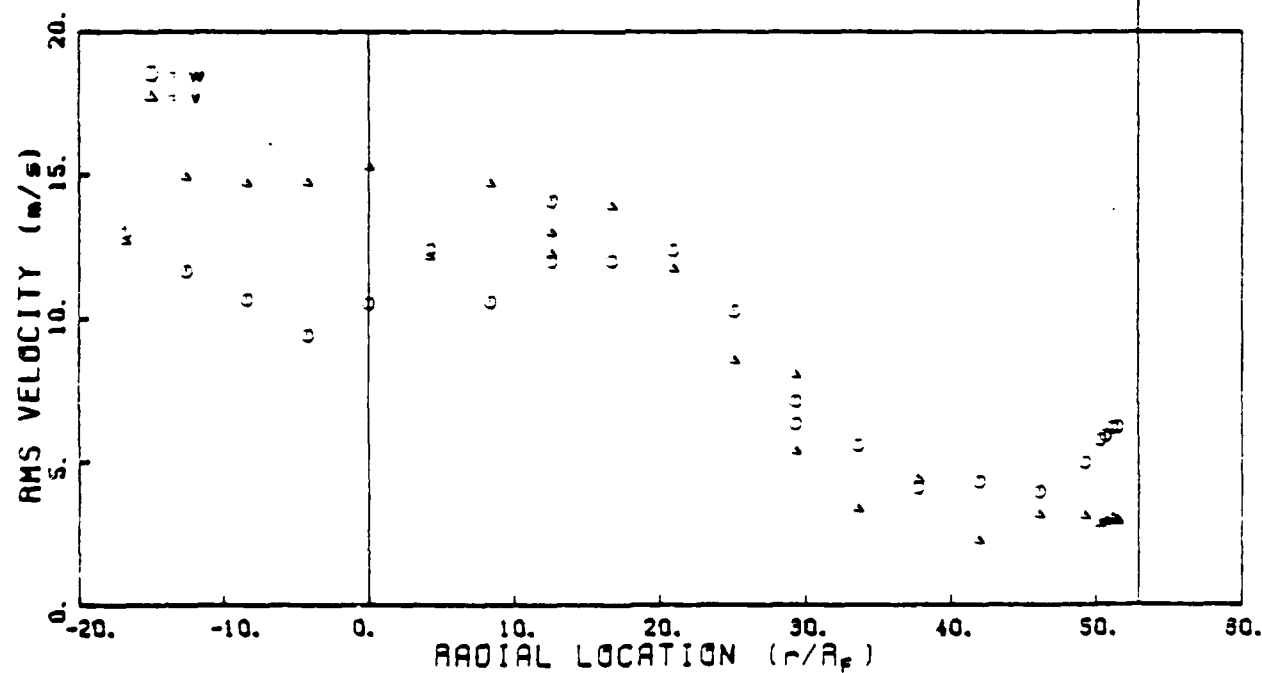
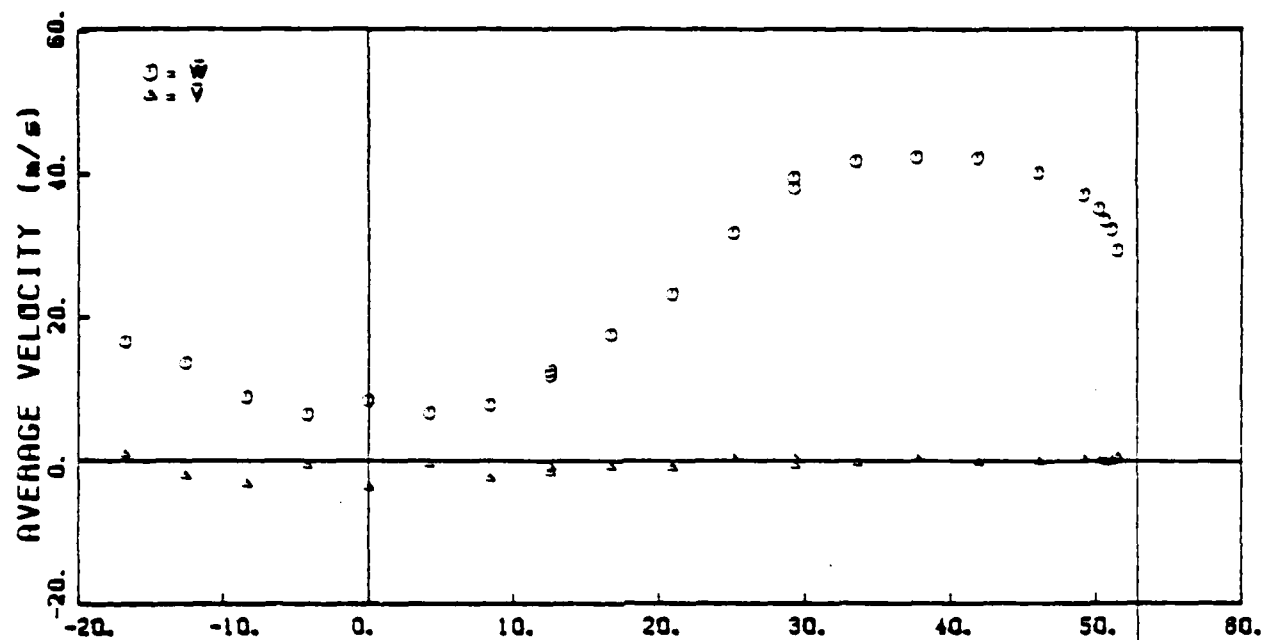
(h)

|         |      |
|---------|------|
| $Z/D_c$ | 1.00 |
| $FF$    | 0    |
| $AF$    | 2    |



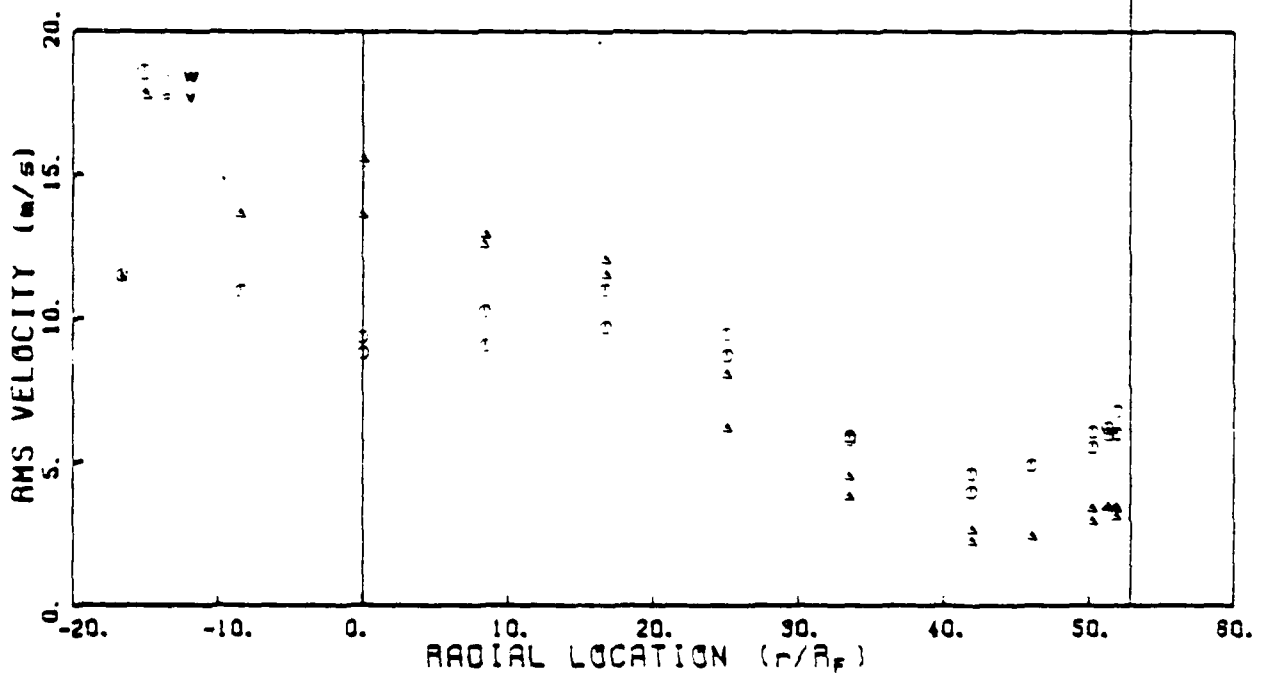
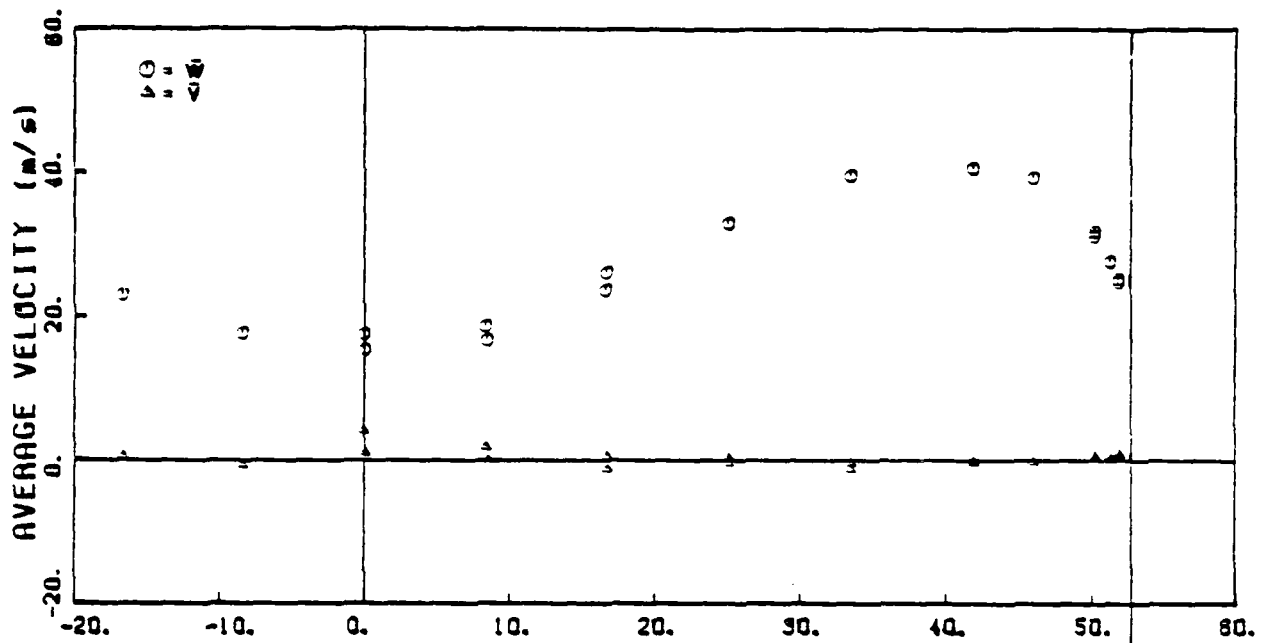
(i)

|         |      |
|---------|------|
| $Z/D_c$ | 1.14 |
| FF      | 0    |
| AP      | 2    |



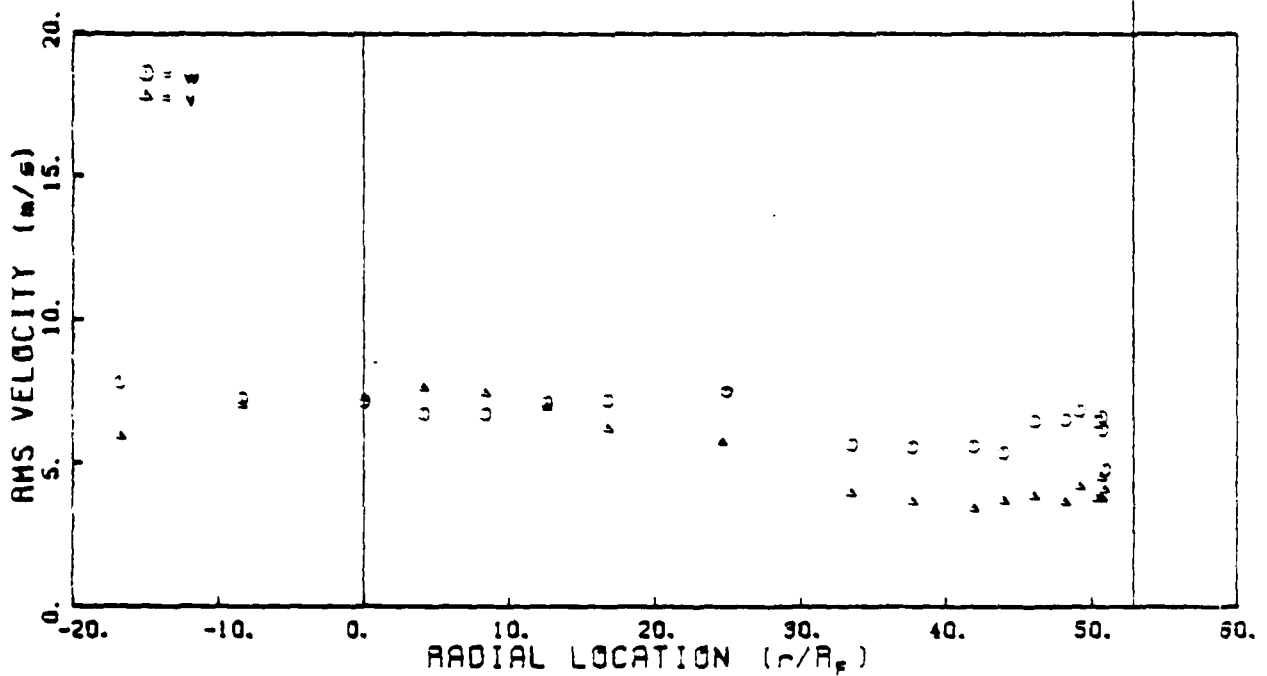
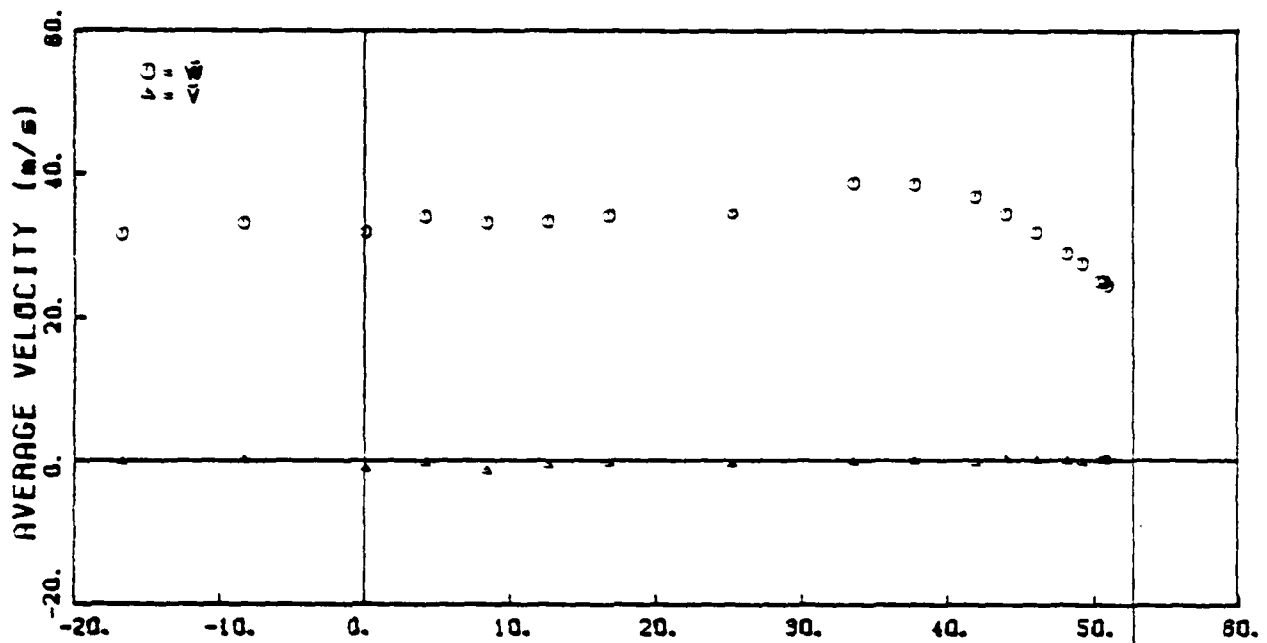
(j)

|         |      |
|---------|------|
| $Z/D_C$ | 1.43 |
| FF      | 0    |
| AF      | 2    |



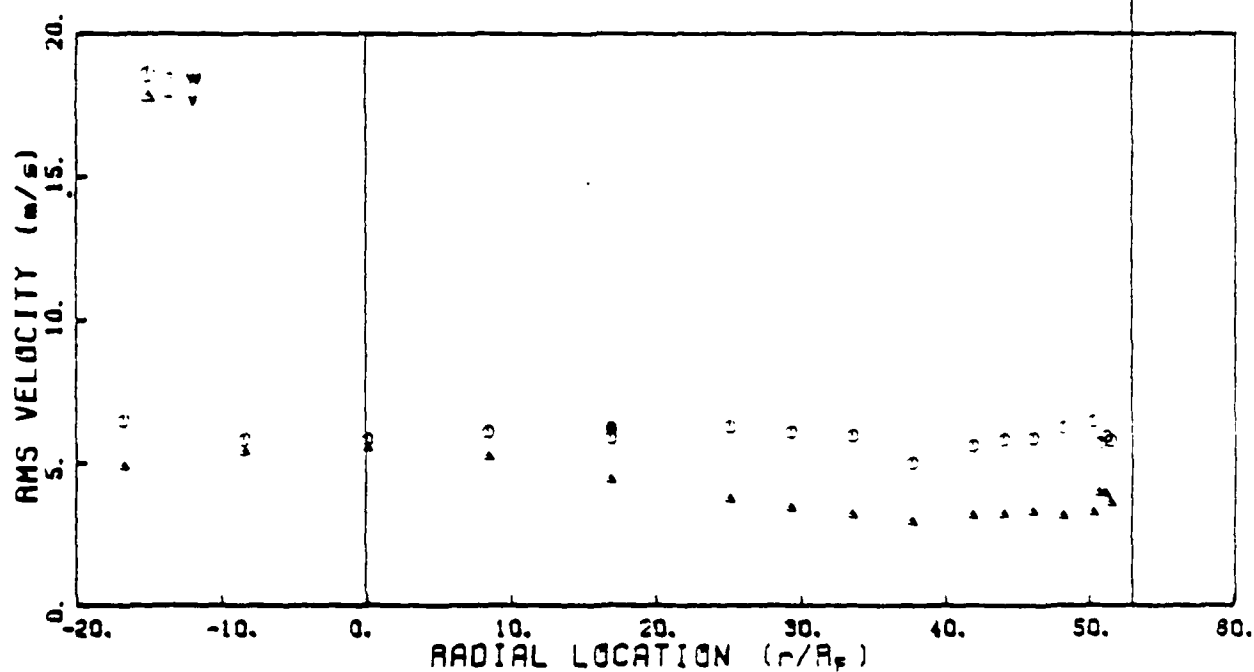
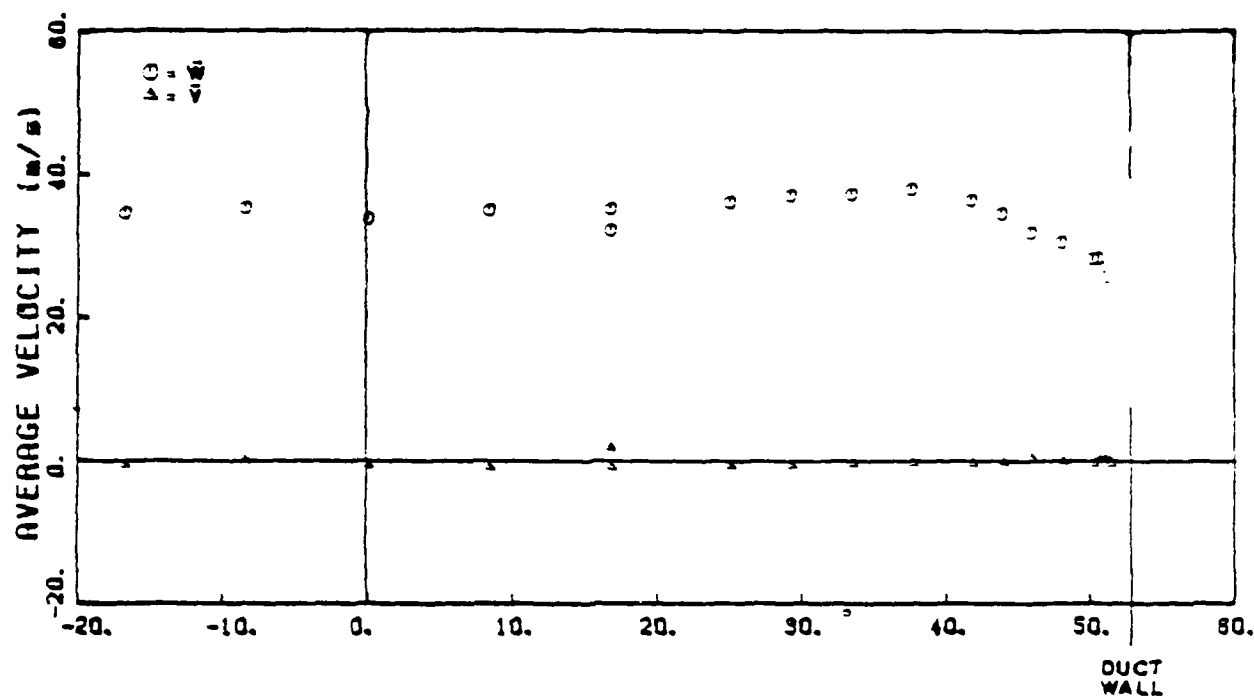
(k)

|         |      |
|---------|------|
| $Z/D_C$ | 2.36 |
| FF      | 0    |
| AF      | 2    |



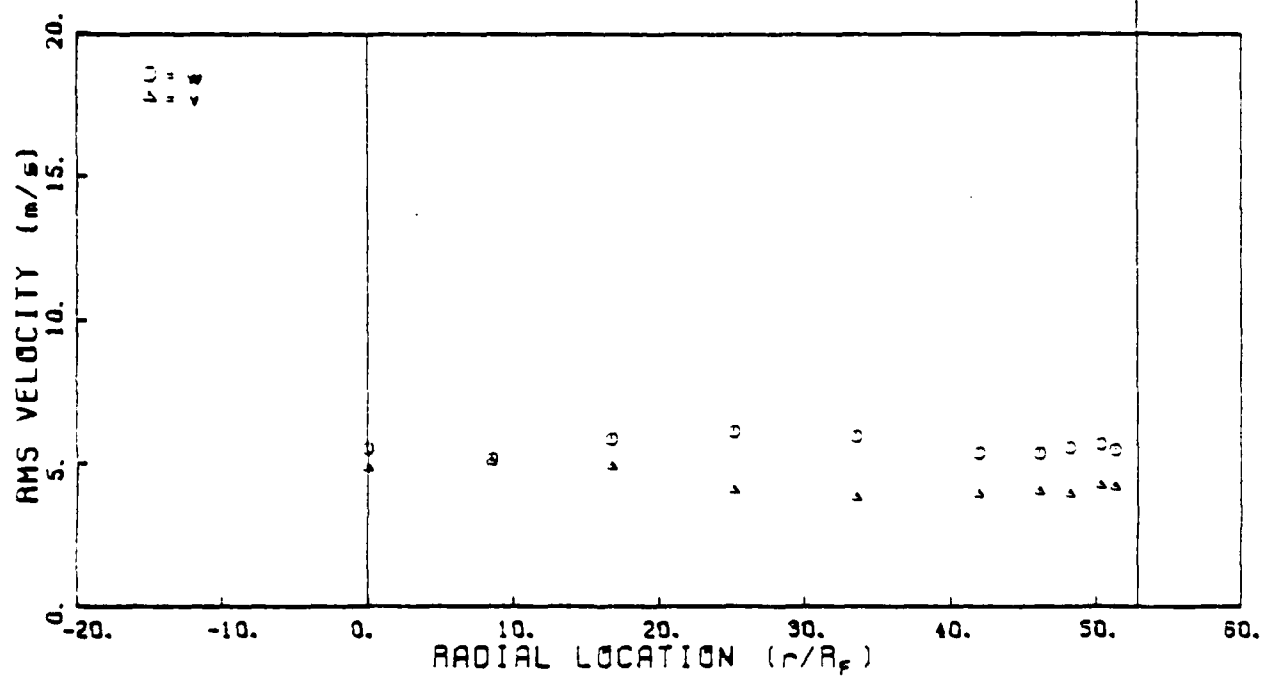
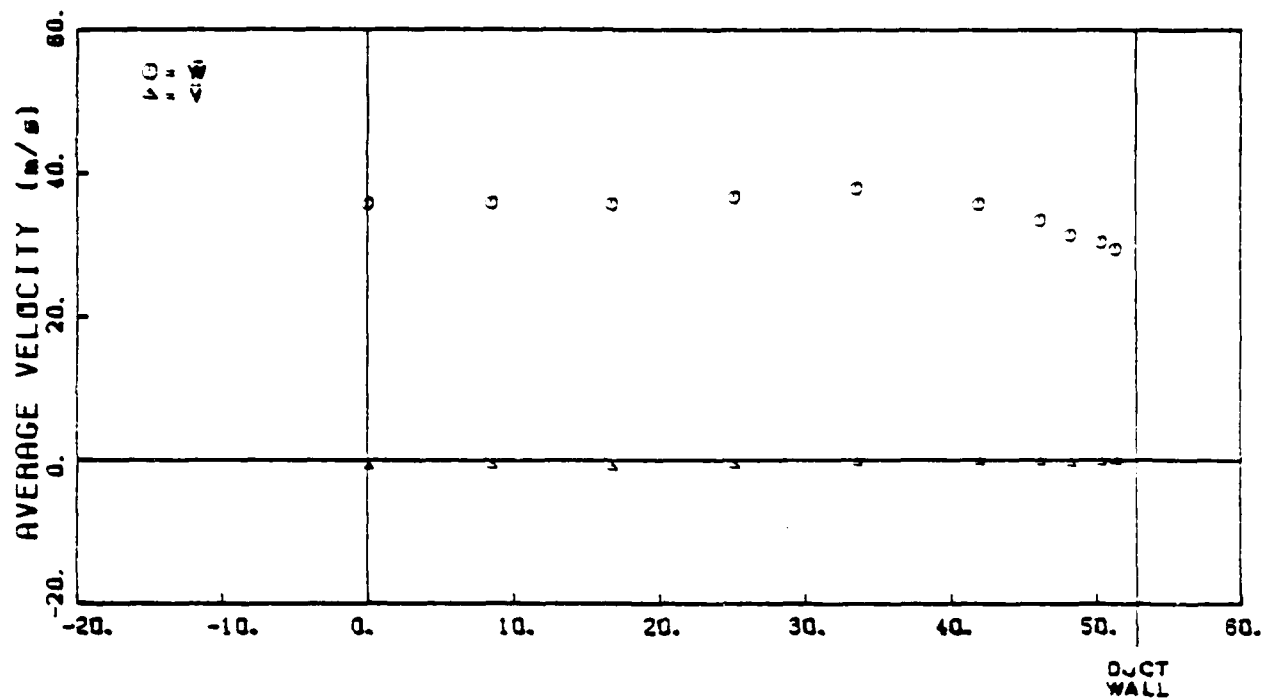
(1)

|         |      |
|---------|------|
| $Z/D_c$ | 3.57 |
| FF      | 0    |
| AF      | 2    |



(m)

|                  |      |
|------------------|------|
| Z/D <sub>c</sub> | 4.29 |
| FF               | 0    |
| AF               | 2    |



(n)



The other two scans were combined with Figure 27 to provide the radial velocity profiles shown in Figure 28, according to the mathematical manipulation of Eqs. (3a) to (3c). These profiles should be used cautiously. Once the measurement location is beyond  $r/R_F \approx 10$  the  $(\sin \theta)^{-1}$  factor quickly becomes large and can combine with small errors in  $\bar{v}$  to severely distort the profile. The velocities reported are small and the uncertainties are comparatively large. The profiles should be used to indicate trends. They do display the expected inversion at  $0.29 < Z/D_C < 0.43$  indicating planes on either side of the vortex center.

The profiles shown in Figures 27(a) to (n) were input to the mass and momentum computation program discussed in the section on free jets. The results are shown in Figure 29. Also plotted are the results using the coaxial flow profiles, the addition of a 6 kg/hr central jet having no observable impact on the 2 kg/s annular jet contribution. The computed mass flow is 2 kg/s  $\pm 3\%$  over the entire range of axial stations  $0 < Z/D_C < 4.29$ . The axial momentum flow starts at the value expected for a flat-top velocity profile in the annulus. As the flow in the recirculation zone builds up, the momentum flow diminishes. The decrease continues past the air stagnation position, until the flow in the region blocked by the centerbody has built up to match the decreased velocity around the periphery. At this point the flow appears to be almost a flat-top velocity profile across the duct, and the momentum bears this out. As the flow proceeds downstream, it is expected to become fully developed pipe flow across the duct. The anticipated momentum flow is shown on Figure 29. Typically a length of  $Z/D_C$  of 50-100 is required to achieve this condition so it is not observed in the modest downstream region observable  $(Z/D_C)_{\max} = 4.29$  although some recovery is observed.

The mass and momentum program provides an output of the integrated mass between centerline and each radial step out to

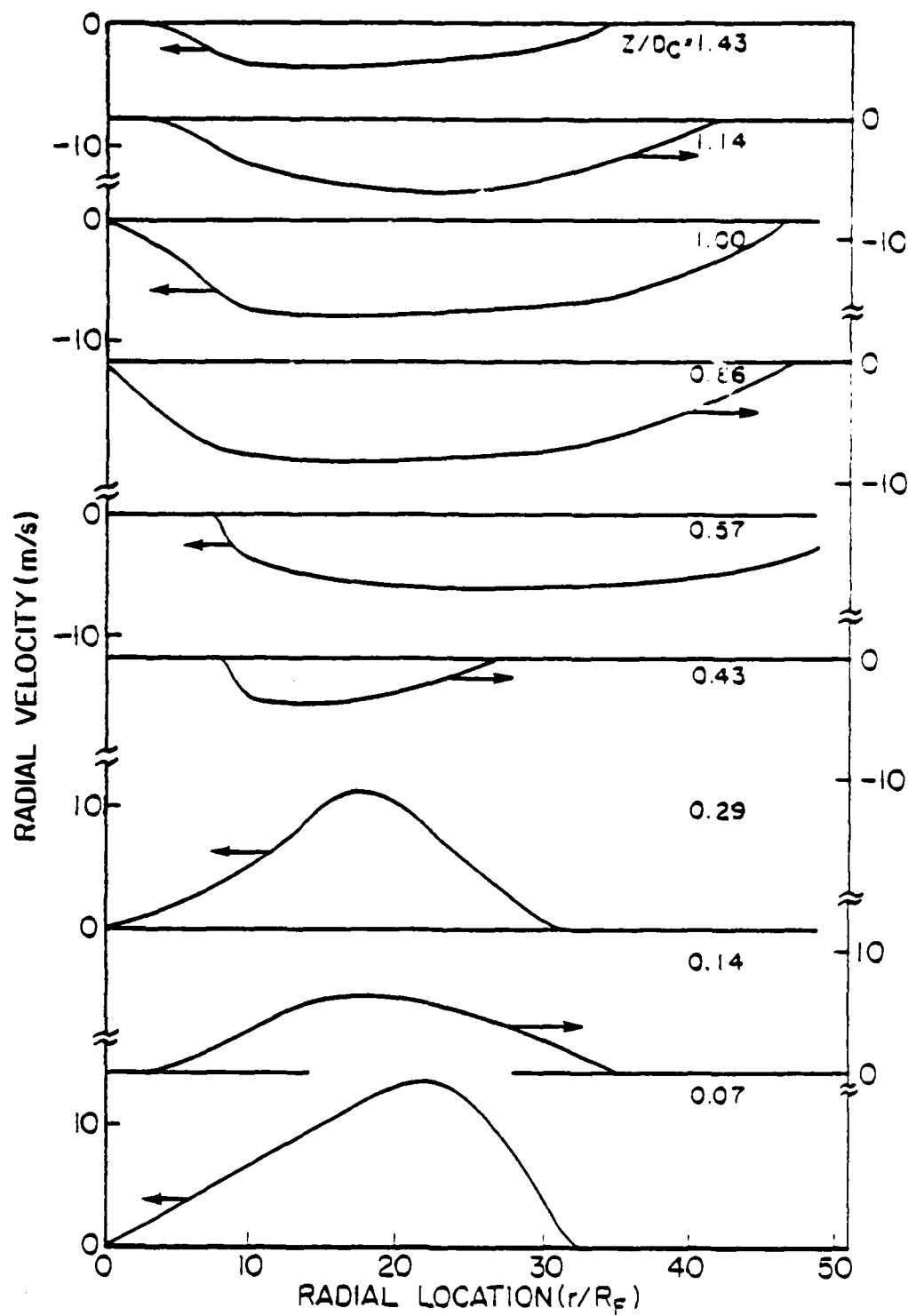


Figure 28. Radial Profiles of the Average Radial Velocity Component at Several Downstream Stations. These curves were computed using composite profiles as discussed in the text.

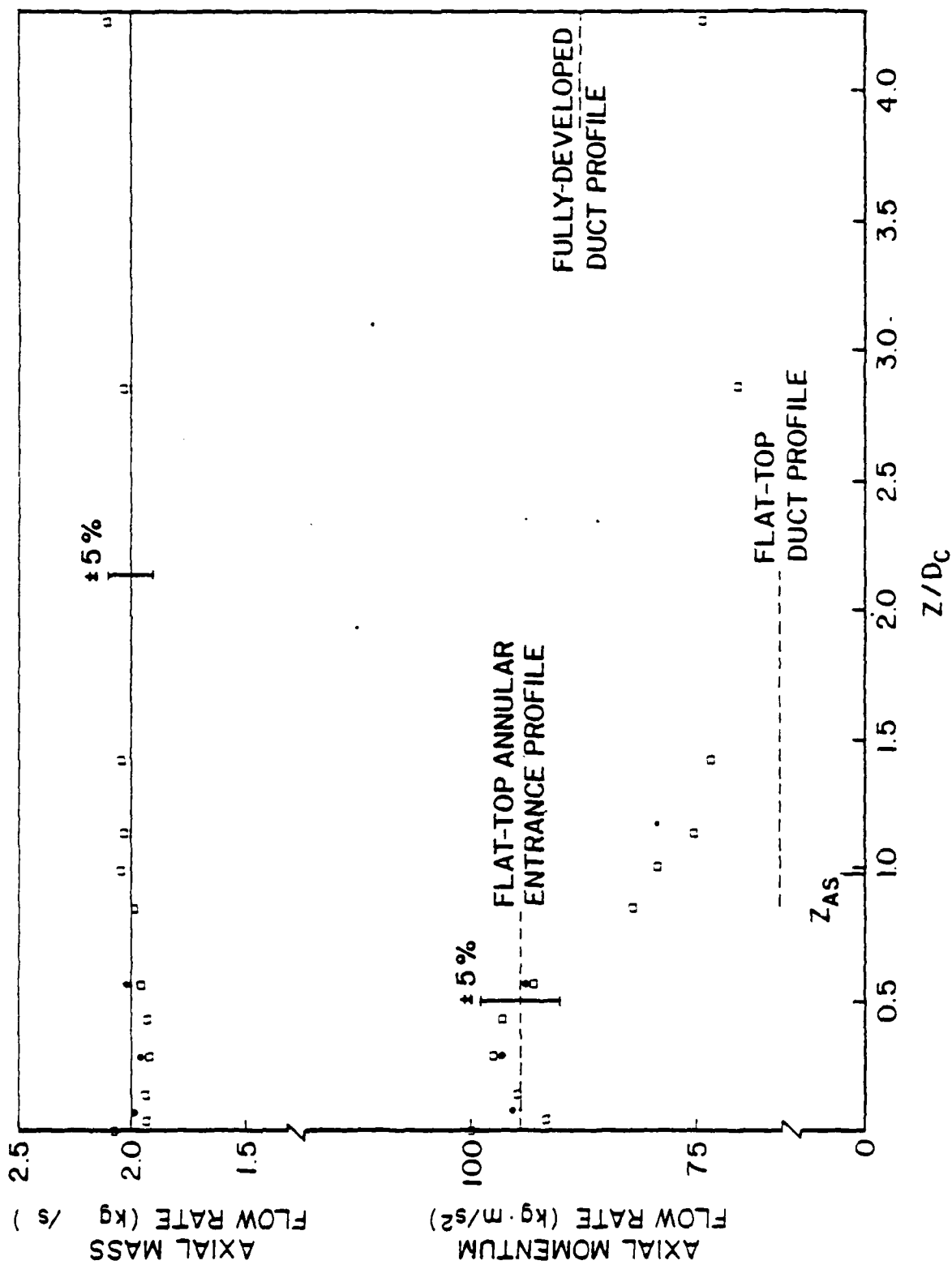


Figure 29. Axial Mass and Momentum Flow Computed from the Radial Profiles of the Axial Velocity. The open data points are for annular-jet-only flow and the closed data points are for coaxial flow (the contribution of the central jet is negligible).

the duct wall. These data are then interpolated to determine the radial locations which encompassed specific mass flow fractions. By connecting these locations of constant mass flow fractions the streamlines for the flow are determined. These are shown in Figure 30. The region of the centerbody  $0 < r/D_c < 0.5$  is shown shaded on the axis;  $0.5 < r/D_c < 0.91$  is the annulus. The recirculation region contours were evolved with substantial artistic license in the regions of severe curvature where data points are sparse. It should be remembered that the data points are measured along planar cuts through the flow. Consequently, it is not possible to follow a streamline to trace it out. Only one planar cut showed a reverse streamline of  $-0.065$  and this is shown as a point in Figure 30. But, from the radial velocity data shown in Figure 28, the center of the vortex should be upstream of this point. Unfortunately, the planes of measurement are too far apart to locate the  $-0.065$  contour and the vortex center cannot be determined any more precisely than  $0.36 < Z/D_c < 0.43$ ,  $0.34 < r/D_c < 0.38$ .

Radial scans along the X axis ( $Y=0$ ) were made with the flow conditions: central jet 6 kg/hr  $\text{CO}_2$ ; and annular jet 2 kg/s air. These were taken at axial positions  $0.01 < Z/D_c < 0.57$ , at which point it was determined that there was no observable difference between the measurements with and without the central jet. The influence of the central jet is restricted to a region near the centerline and this was examined in more detail, at each axial station, by scanning in the Y direction at  $X=0$ . These measurements are also shown in Figure 31. At the entrance plane and for a short distance downstream  $0 < Z/D_c < 0.04$  the central jet has similar characteristics to those measured for the free jet. The jet profile decays much more rapidly due to the reverse flow from the annulus, and the velocity fluctuations increase more dramatically. At the measurement plane  $Z/D_c = 0.29$  the jet is barely discernable, but the axial velocity fluctuations dramatically give evidence to the presence of the central jet.

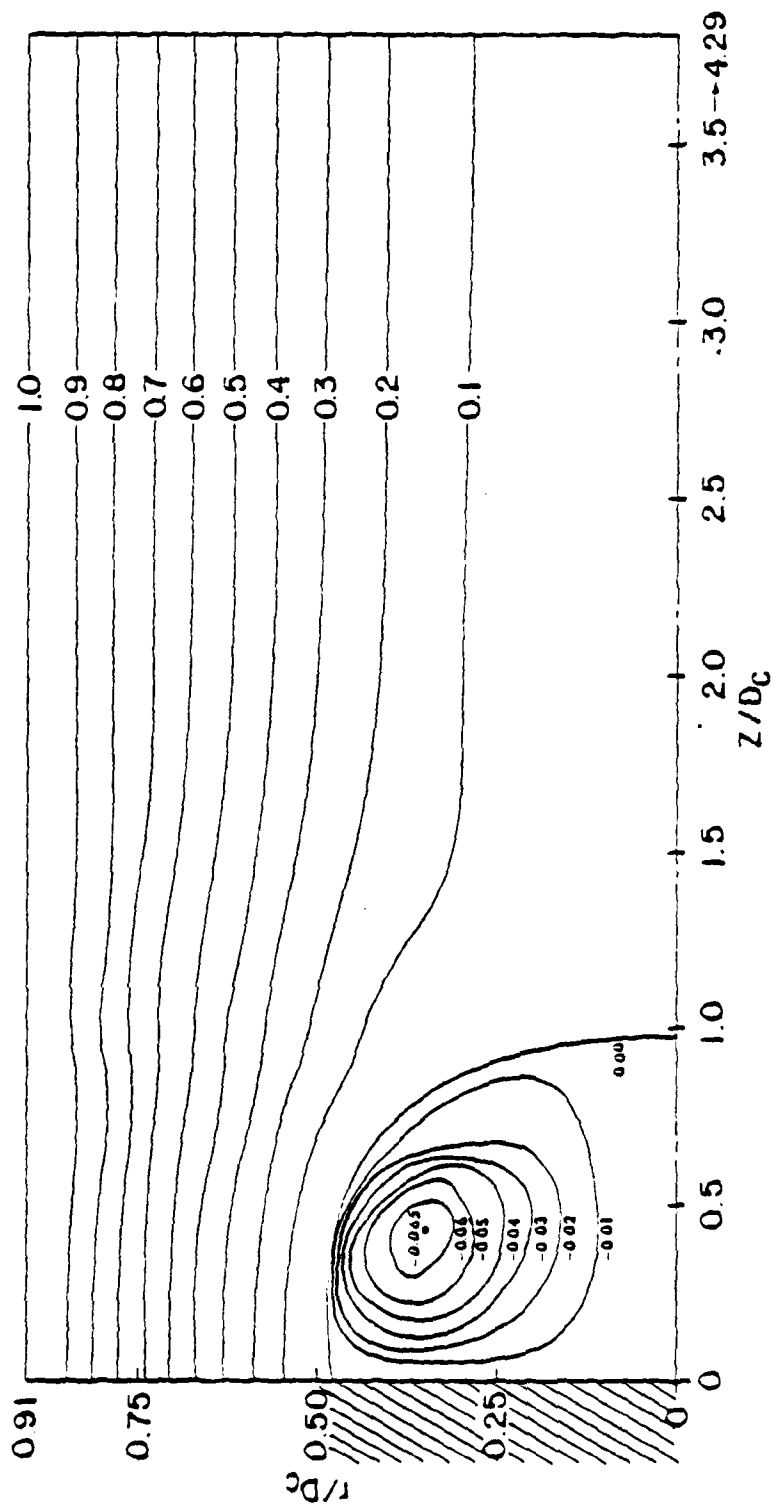


Figure 30. Streamlines Describing the Flowfield for the Annular-Jet-Only Flow Condition (2 kg/s air).

|         |      |
|---------|------|
| $Z/D_c$ | 0.01 |
| FF      | 6    |
| AF      | 2    |

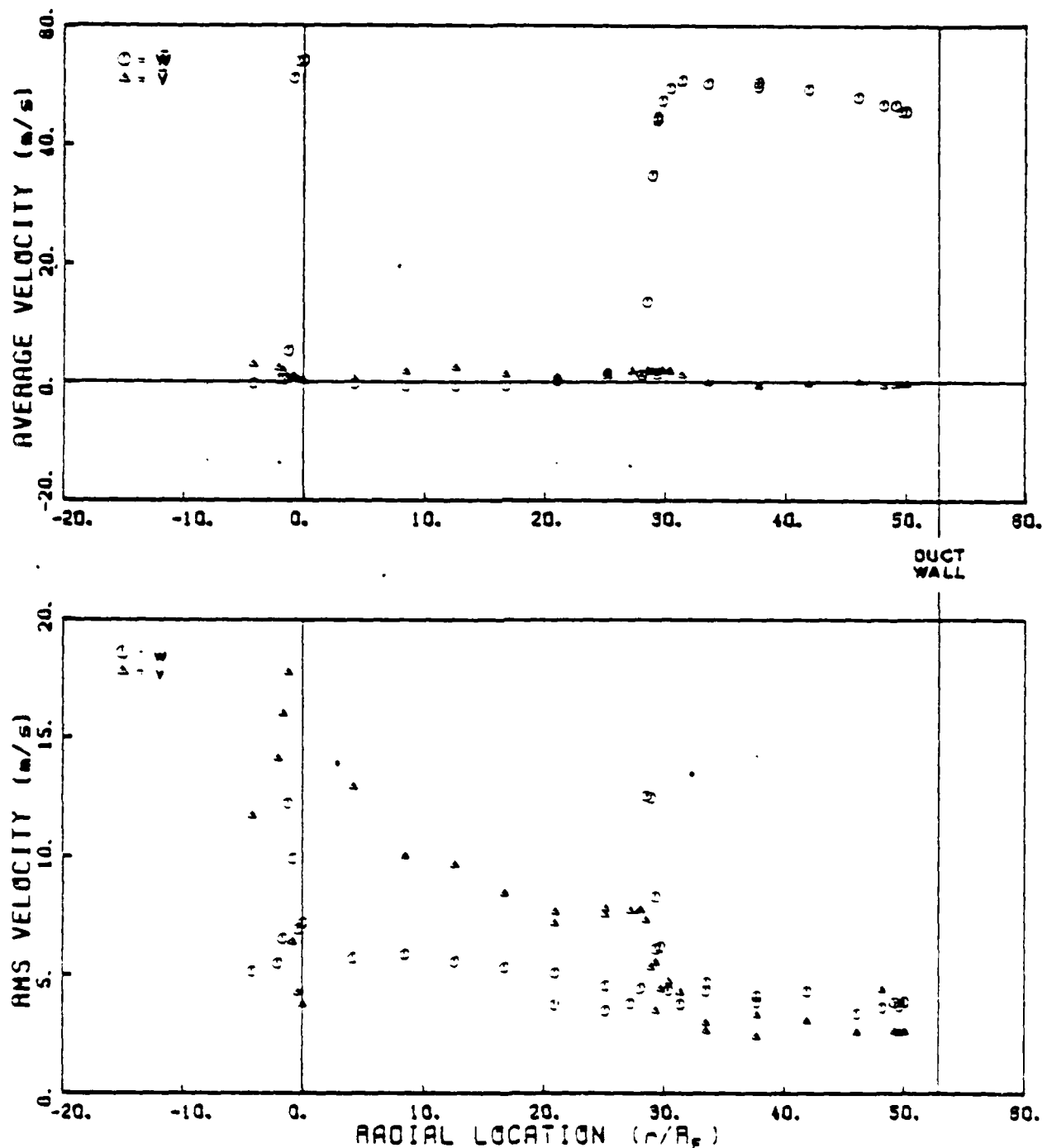


Figure 31. (a.1) - (g.1) Radial Profiles of the Average Axial and Azimuthal Components of Velocity and RMS Velocity Fluctuations for Central Jet Flow of 6 kg/hr  $\text{CO}_2$  and Annular Jet Flow of 2 kg/s Air. The downstream location is marked at the top of each page.

|         |      |
|---------|------|
| $Z/D_C$ | 0.01 |
| FF      | 6    |
| AF      | 2    |

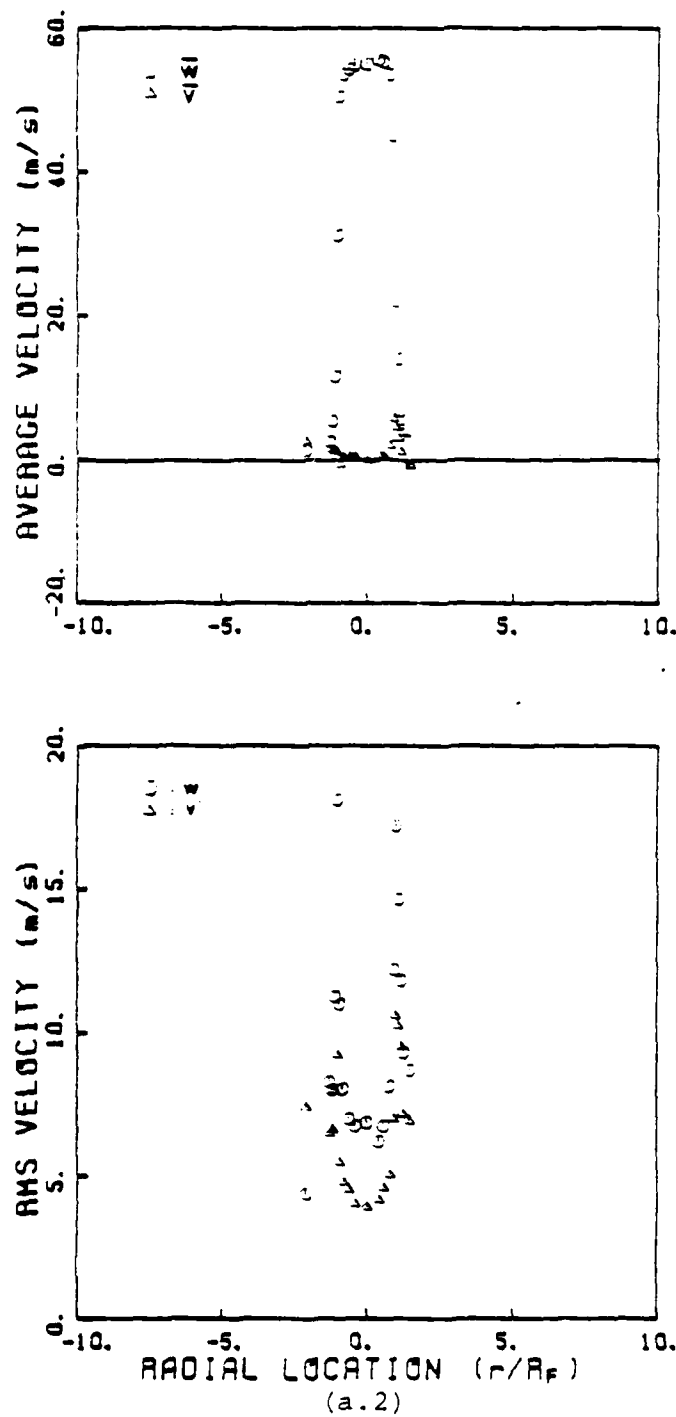
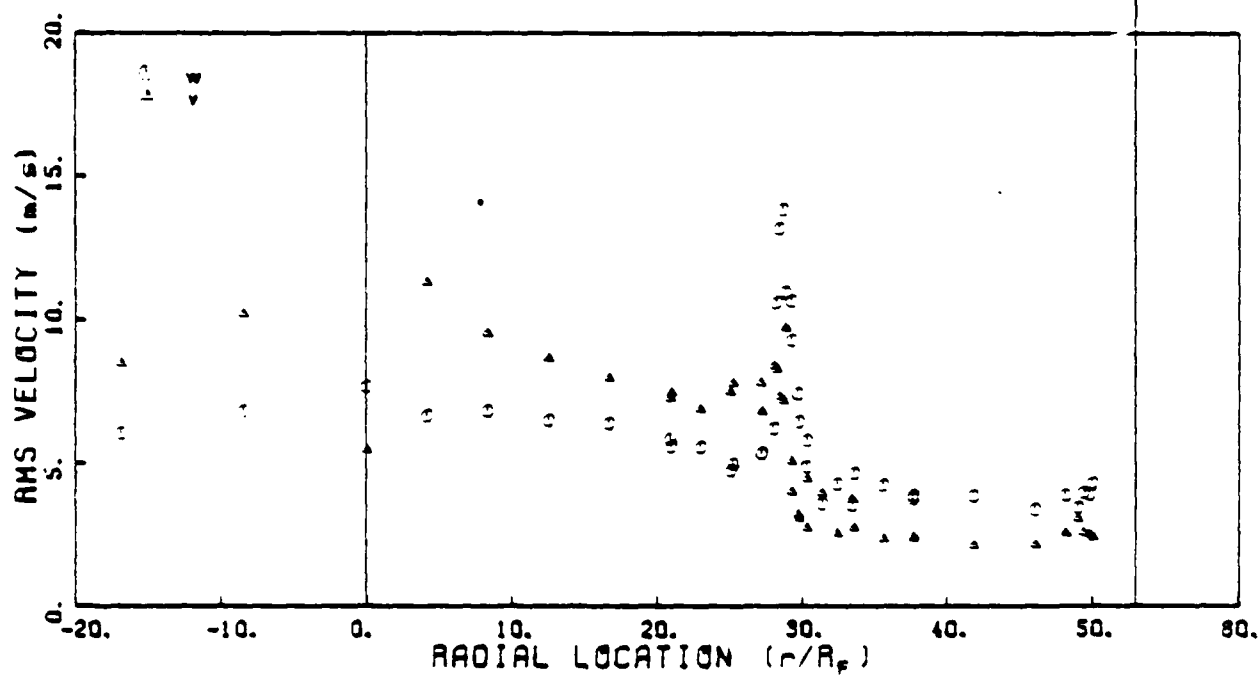
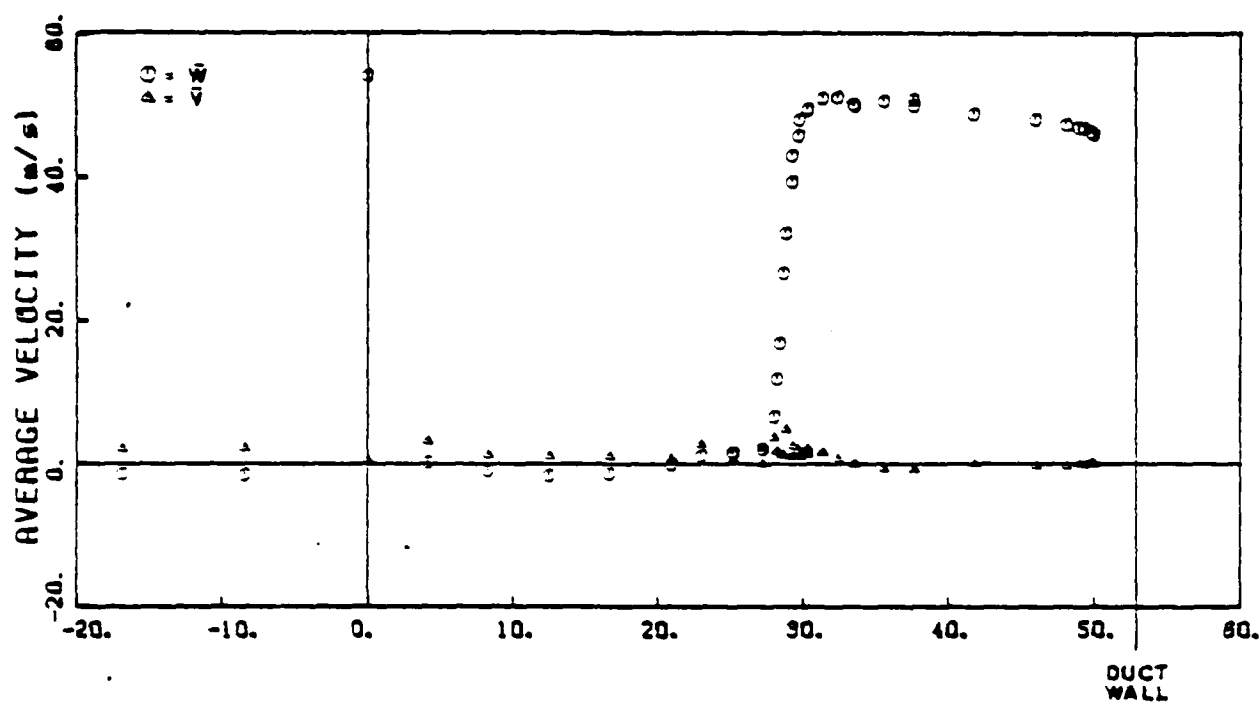


Figure 31. (a.2) - (g.2) Expanded Profiles of the Average Axial and Radial Components of Velocity and RMS Velocity Fluctuations Around Centerline. Each plot accompanies the profile preceding it.

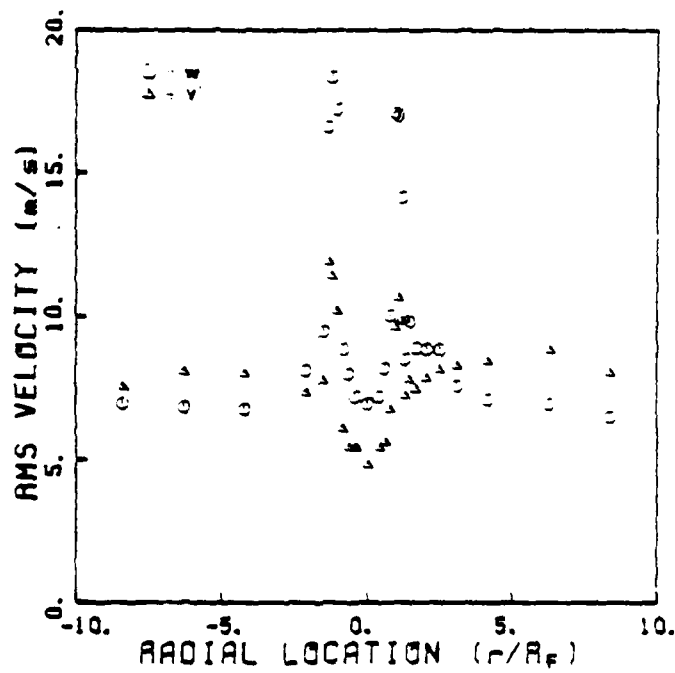
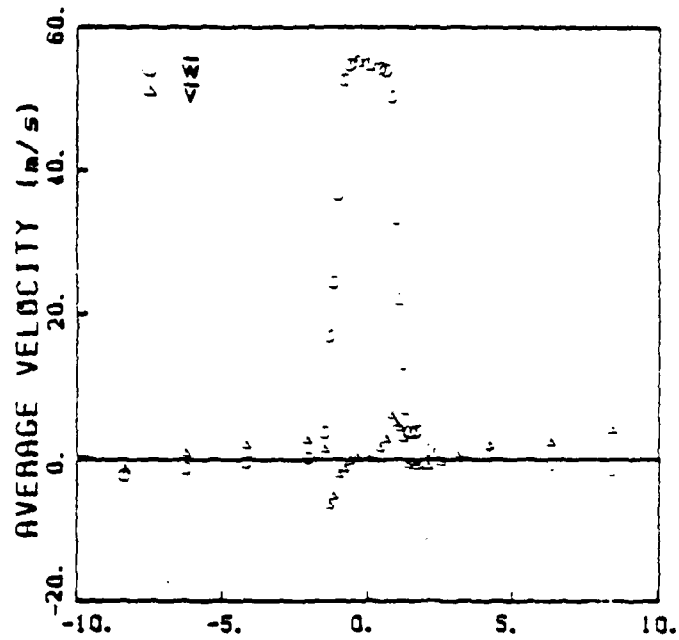
|         |      |
|---------|------|
| $Z/D_c$ | 0.04 |
| FF      | 6    |
| AF      | 2    |



(b.1)

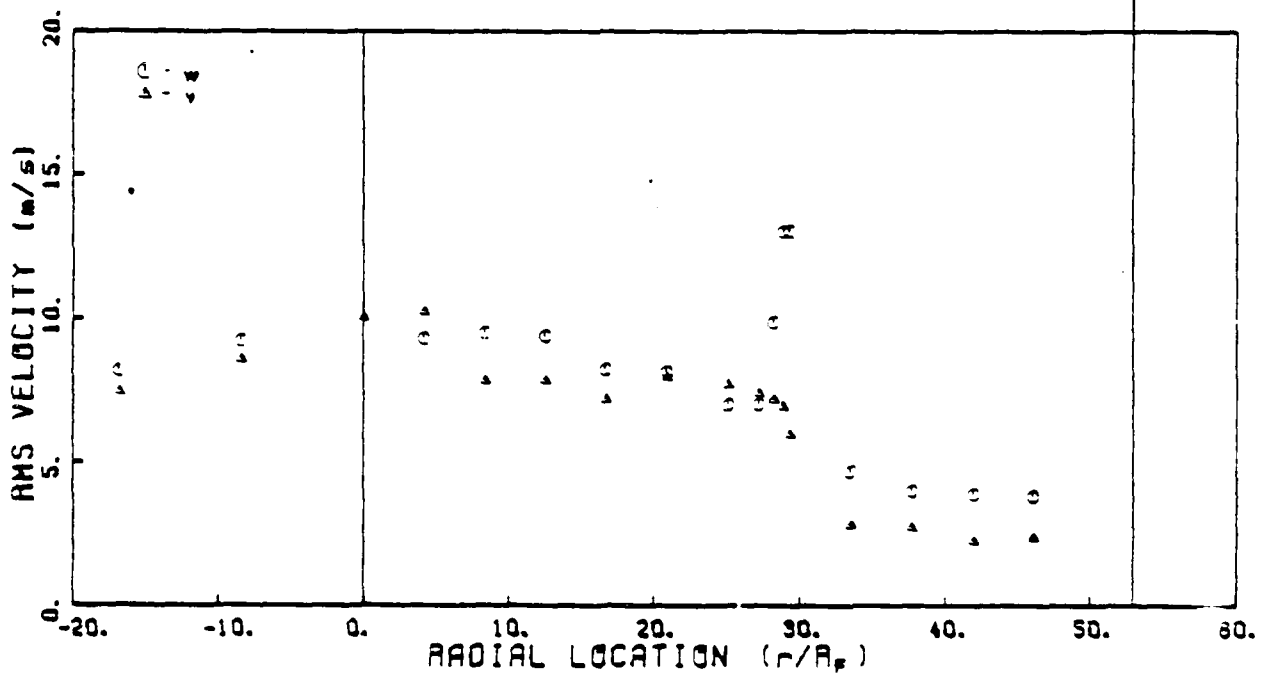
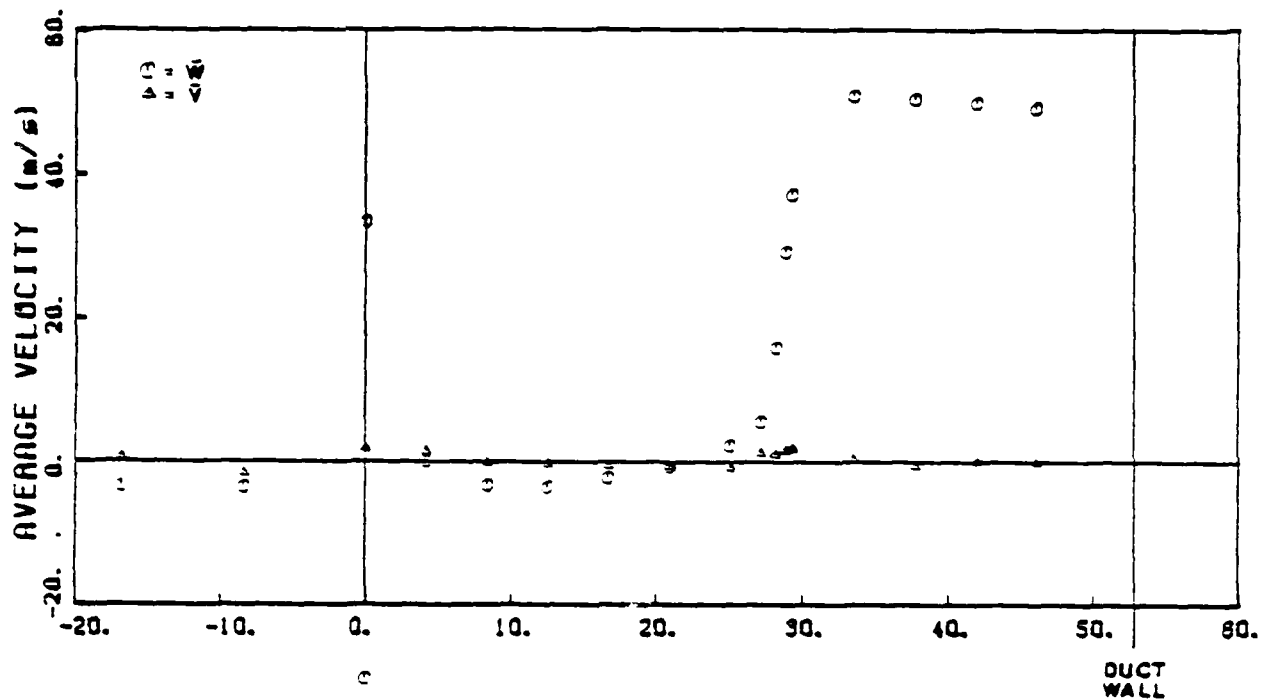


|         |      |
|---------|------|
| $Z/D_C$ | 0.04 |
| FF      | 6    |
| AF      | 2    |



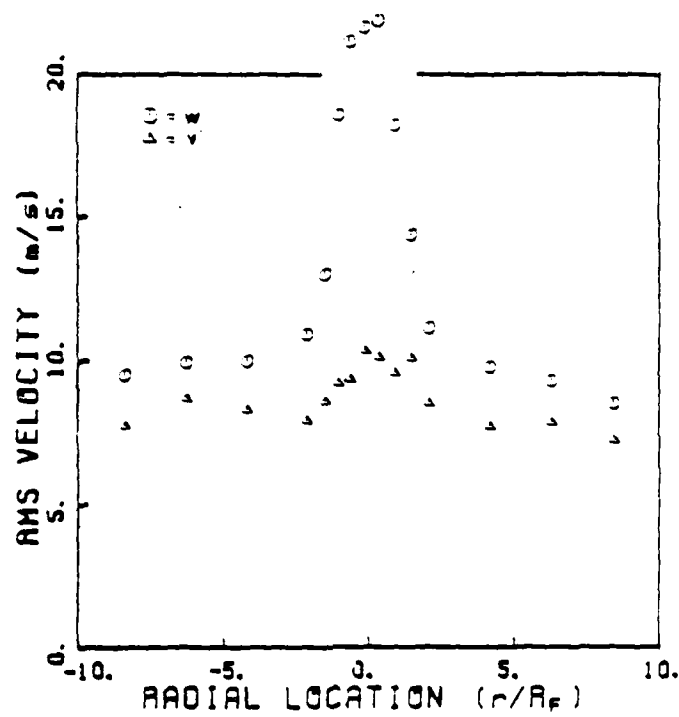
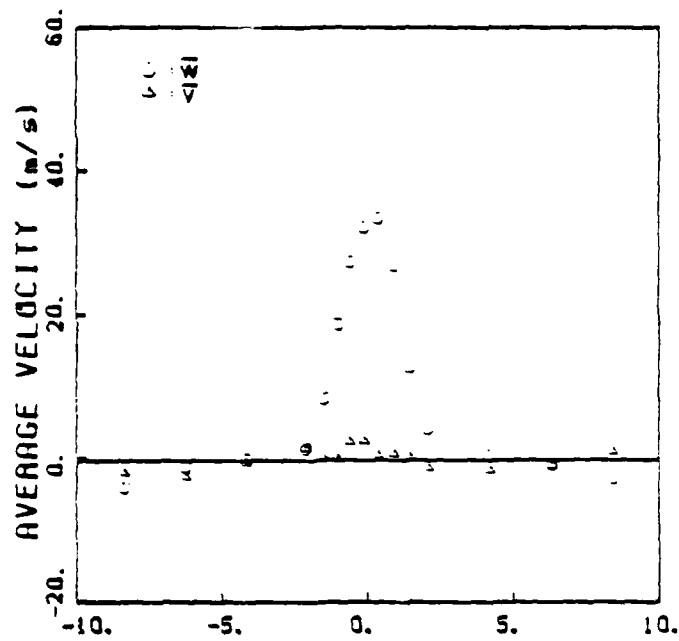
(b.2)

|         |      |
|---------|------|
| $Z/D_c$ | 0.07 |
| FF      | 6    |
| AF      | 2    |



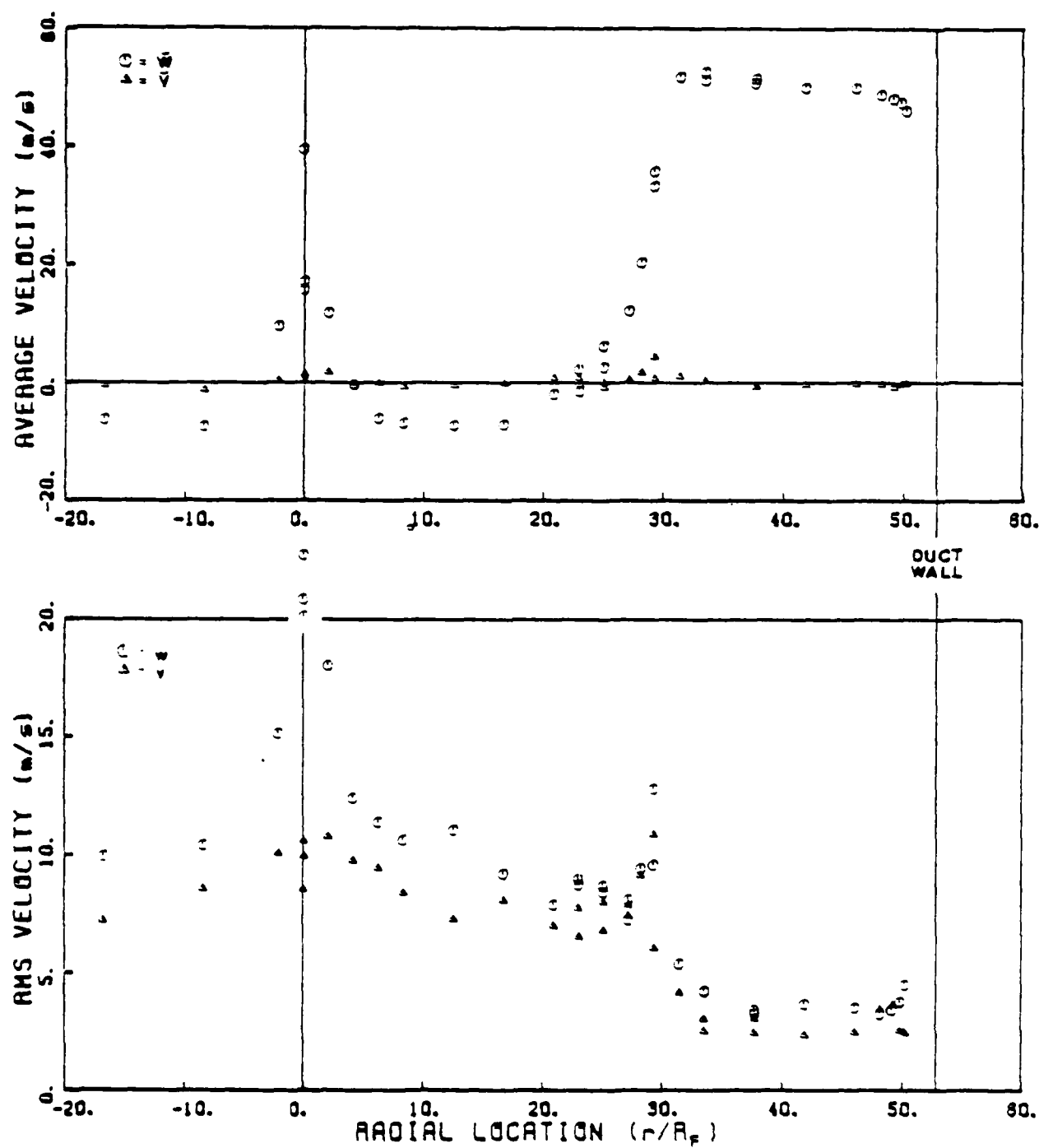
(c.1)

|                  |      |
|------------------|------|
| Z/D <sub>C</sub> | 0.07 |
| FF               | 8    |
| AF               | 2    |



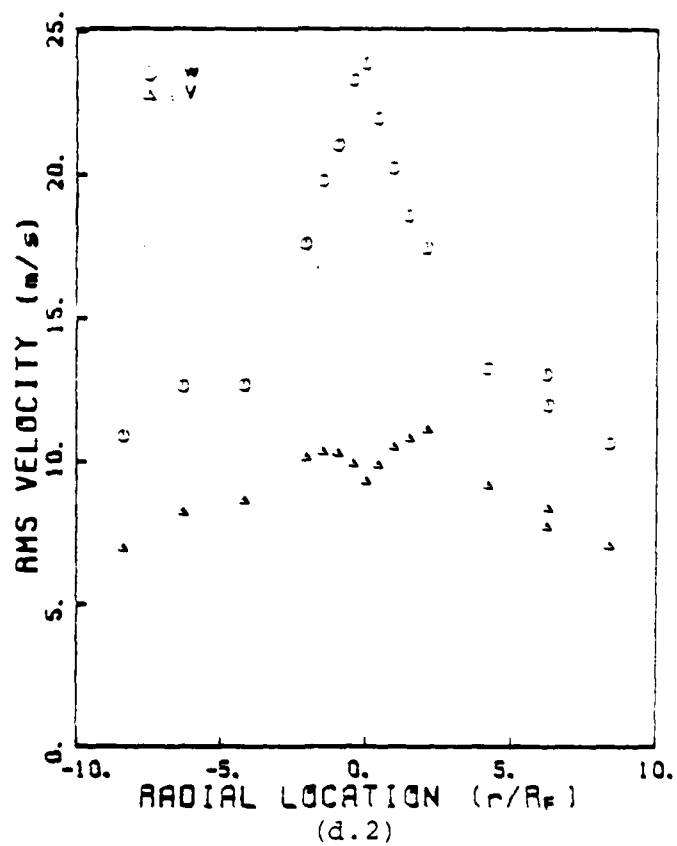
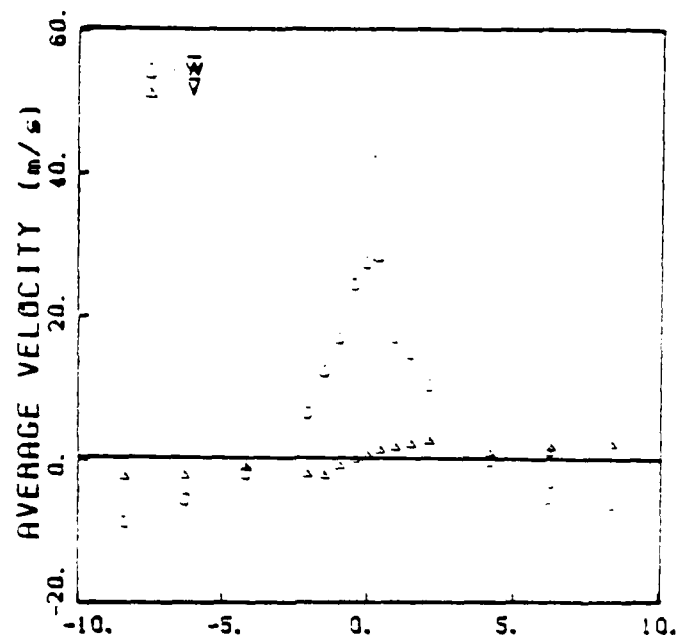
(c.2)

|         |      |
|---------|------|
| $Z/D_c$ | 0.14 |
| FF      | 6    |
| AF      | 2    |

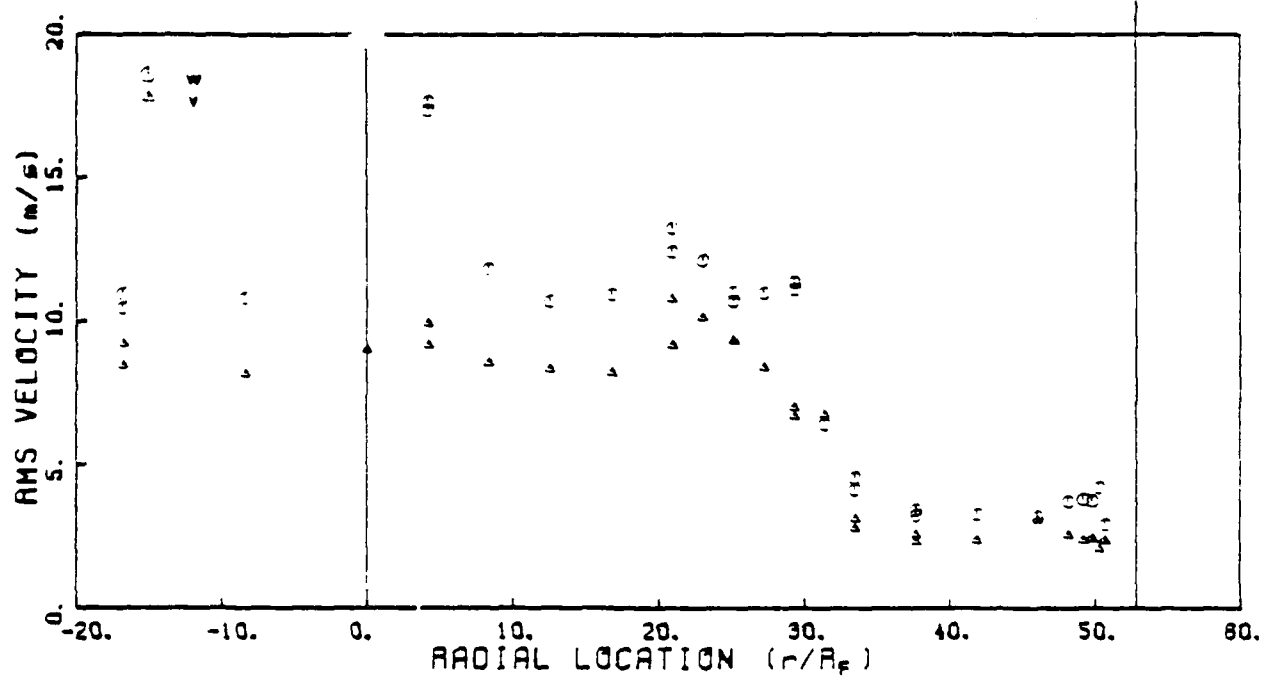
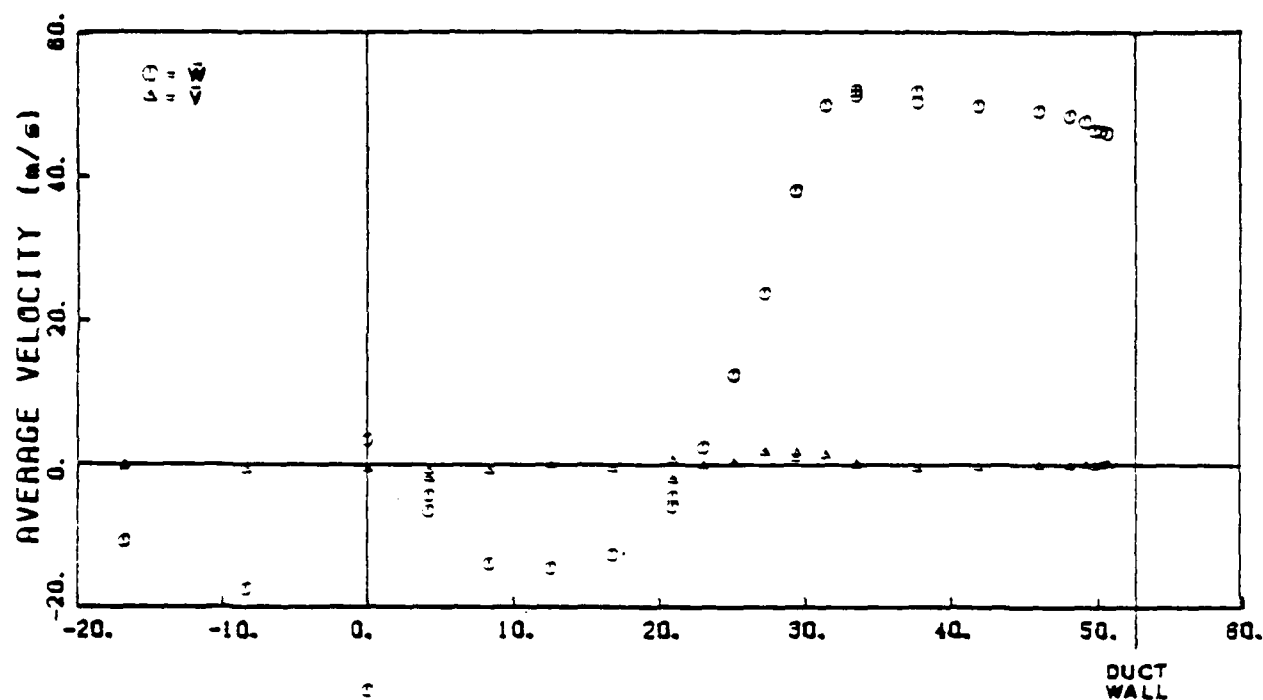


(d.1)

|         |      |
|---------|------|
| $Z/D_c$ | 0.14 |
| FF      | 8    |
| AF      | 2    |

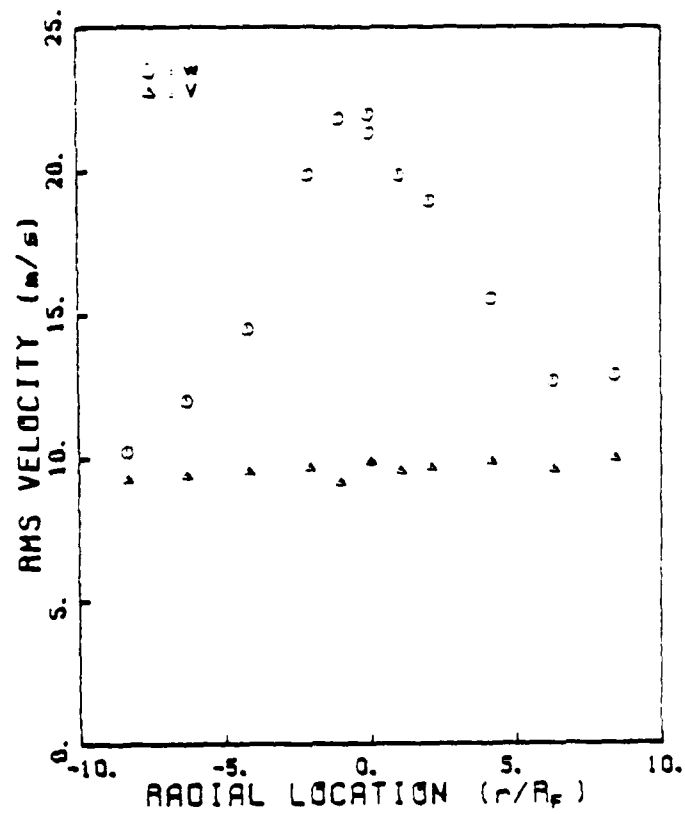
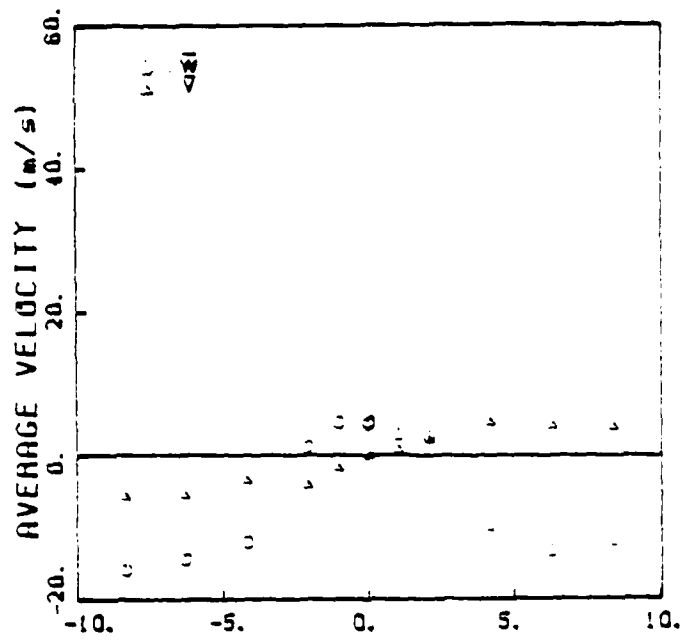


|         |      |
|---------|------|
| $Z/D_c$ | 0.29 |
| FF      | 6    |
| AF      | 2    |



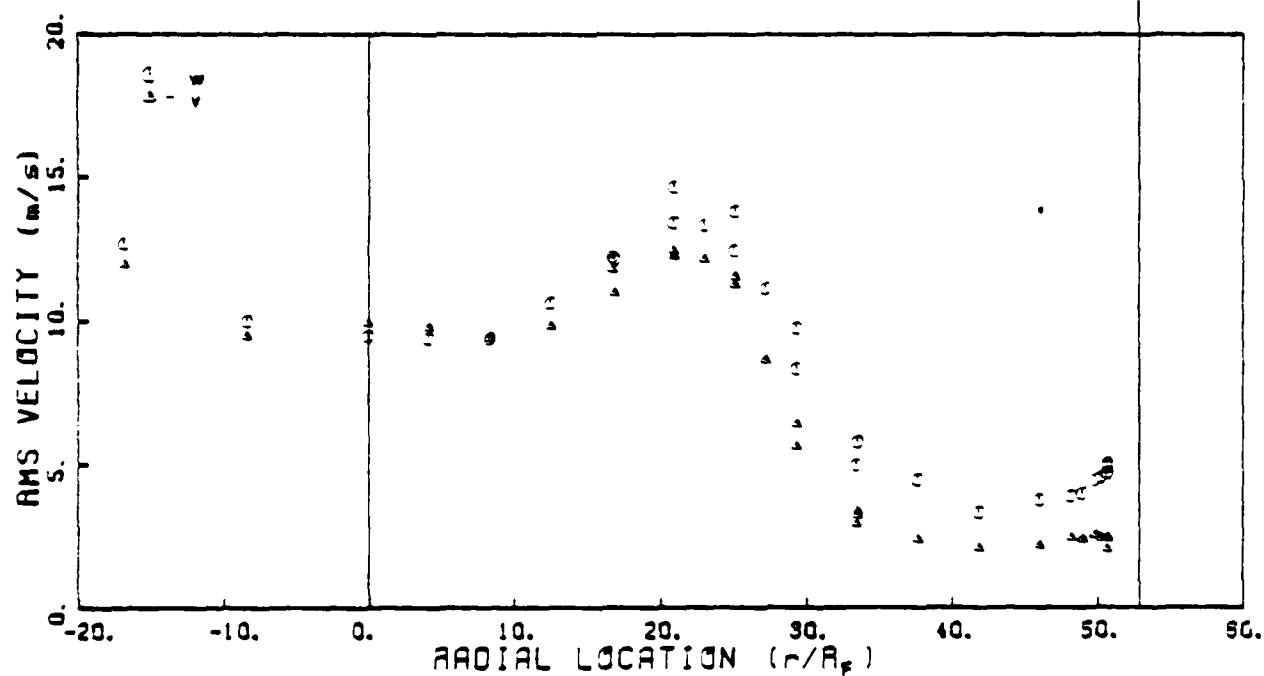
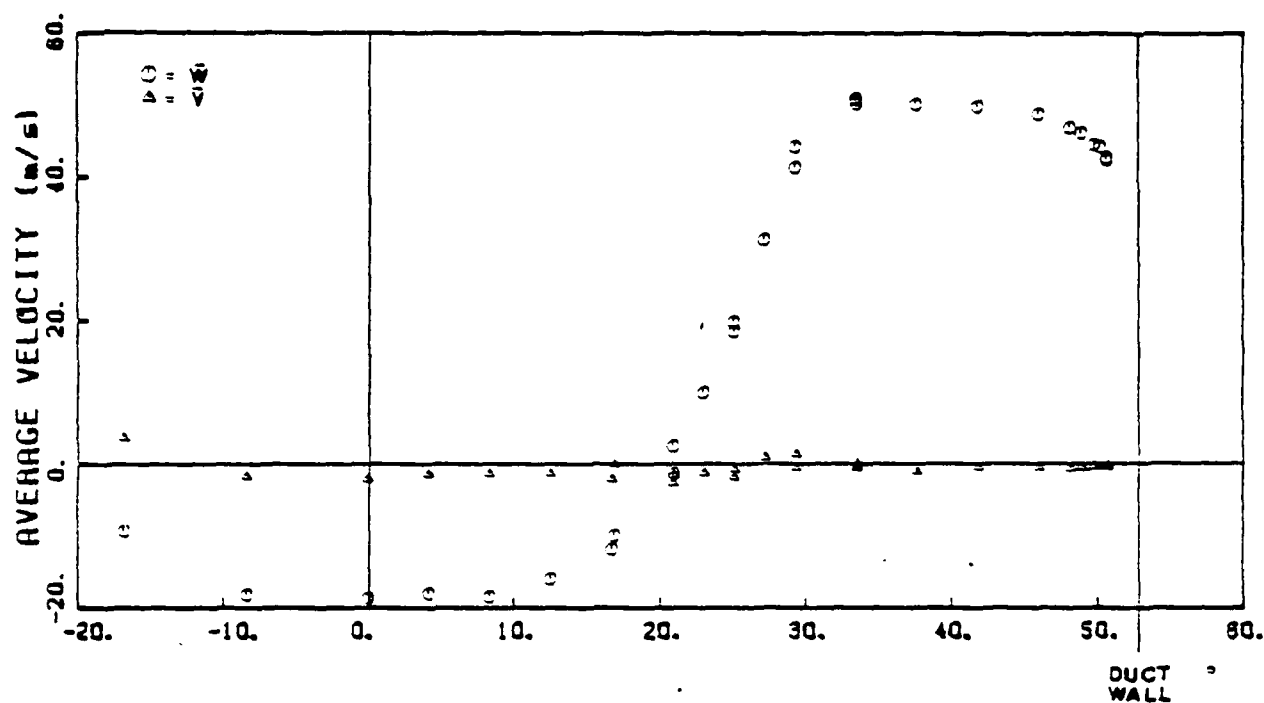
(e.1)

|         |      |
|---------|------|
| $Z/D_C$ | 0.29 |
| FF      | 6    |
| AF      | 2    |



(e.2)

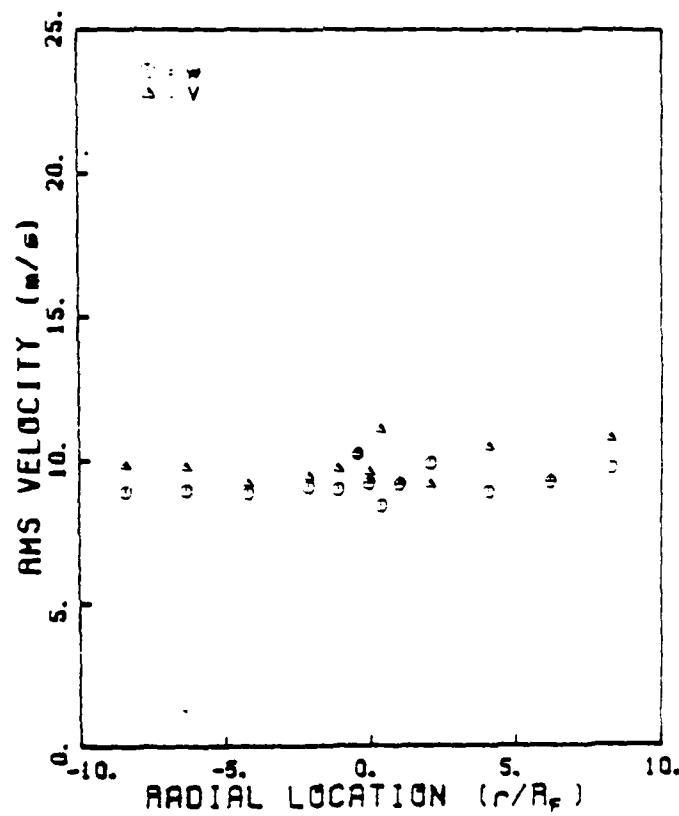
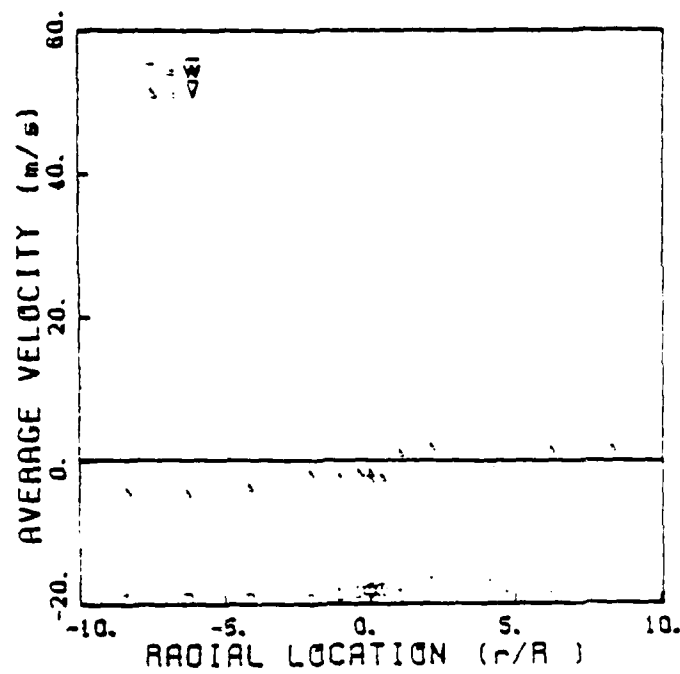
|                  |      |
|------------------|------|
| Z/D <sub>c</sub> | 0.43 |
| FF               | 6    |
| AF               | 2    |



(f.1)

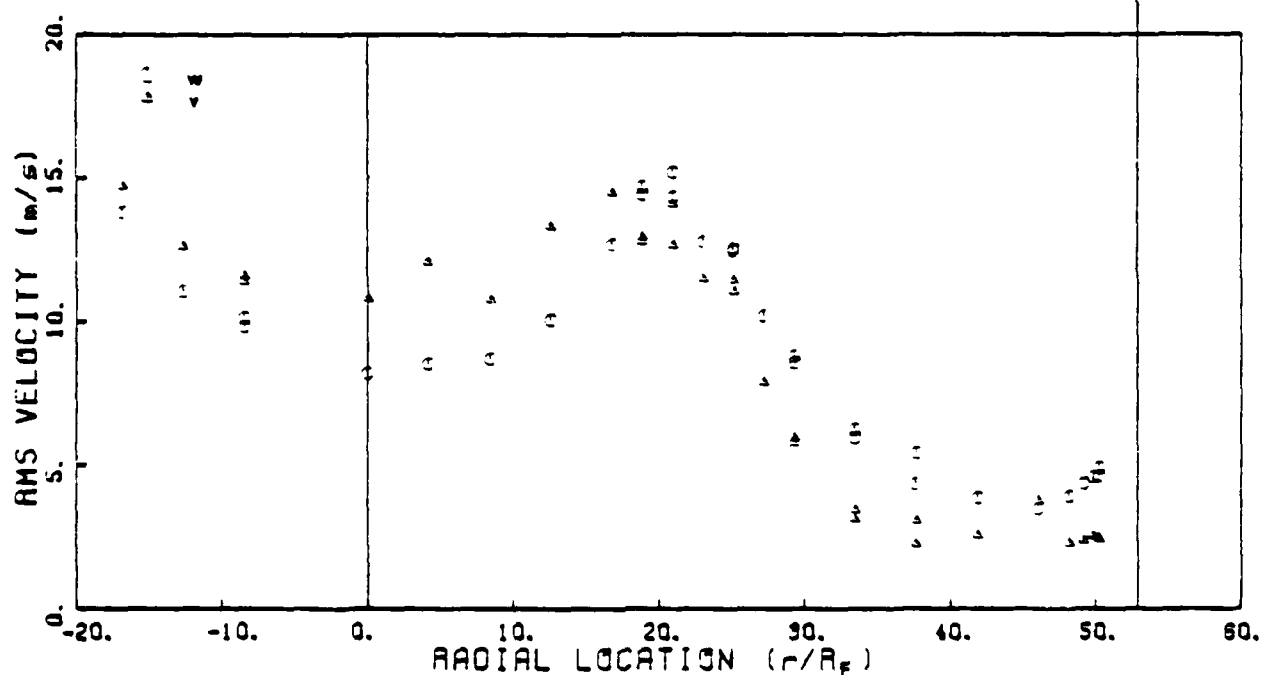
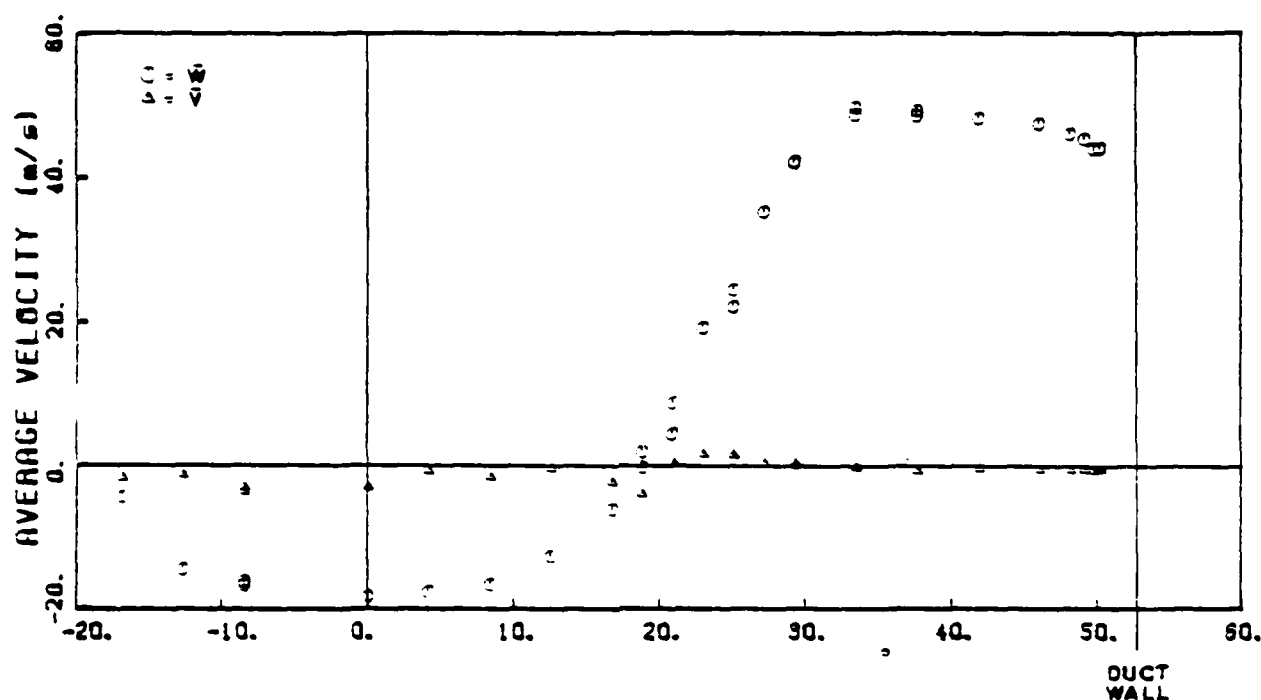


|         |      |
|---------|------|
| $Z/D_C$ | 0.43 |
| FF      | 6    |
| AF      | 2    |



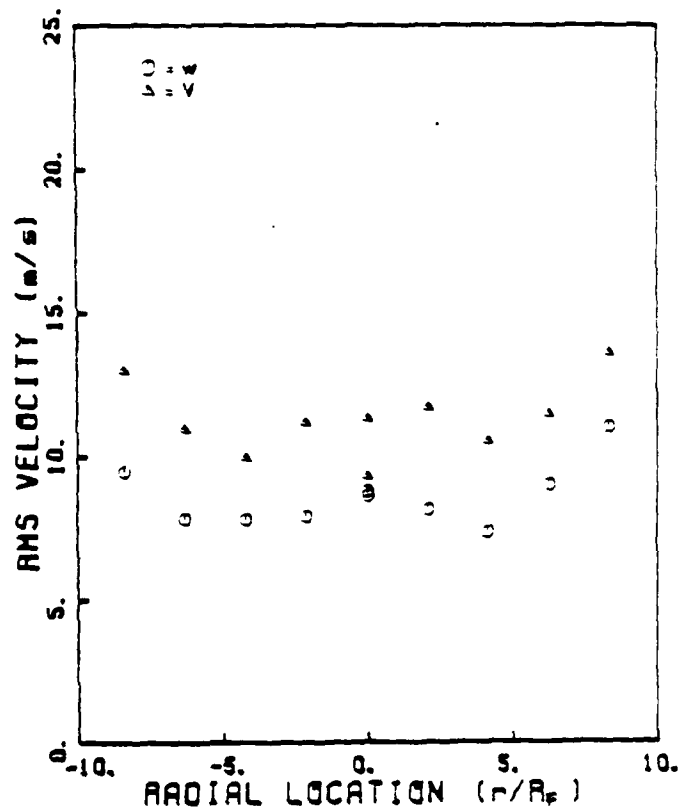
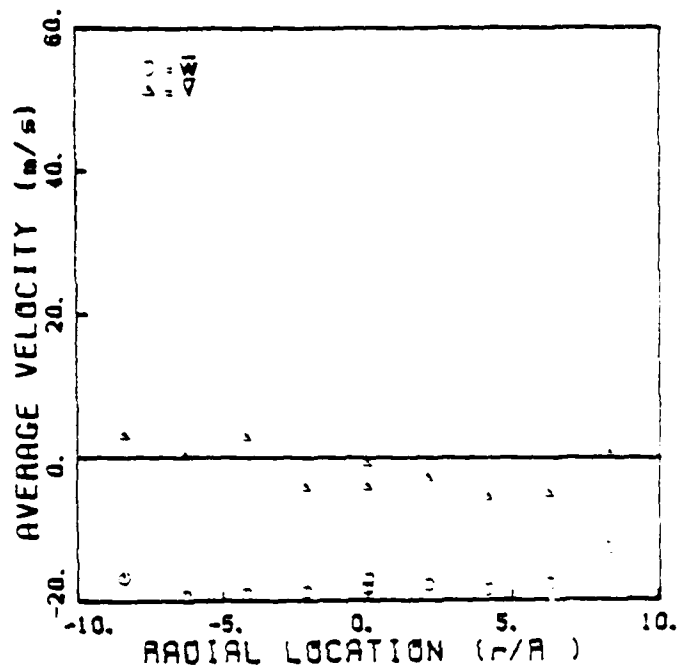
(E.2)

|         |      |
|---------|------|
| $Z/D_c$ | 0.57 |
| FF      | 6    |
| AF      | 2    |



(g.1)

|         |      |
|---------|------|
| $Z/D_c$ | 0.57 |
| FF      | 6    |
| AF      | 2    |



(g.2)

Compare Figures 31(e.1) and 27(e). At  $z/D_c = 0.43$  and beyond, the flow properties have returned to those measured with no central jet.

Centerline profiles were made for the average velocity under the flow conditions: annular jet flow of 2 kg/s air and central jet flow of 0, 2, 6, 16 kg/hr  $\text{CO}_2$ . They are shown in Figure 32. In all cases measured, reverse flow is observed in the average velocity. The maximum reverse velocity, about 41% of the annular inlet plane velocity, is the same as was measured previously.<sup>26</sup> The rms fluctuations are shown in Figure 33.

The locations of the central jet stagnation position were plotted against the ratio of the central jet inlet velocity to annular jet inlet velocity. The result is shown in Figure 34. Also plotted are the results of the previous 1-D LDA measurement, using a different nozzle.<sup>26</sup> It can be seen that with the normalization used the curves are almost identical. Thus it appears that the location of the fuel stagnation point scales with the ratio  $\bar{w}_o^F / \bar{w}_o^A$  and not with the mass or momentum of the central jet.  $\bar{w}_o^F$  and  $\bar{w}_o^A$  are the central jet and annular jet entrance plane velocities.

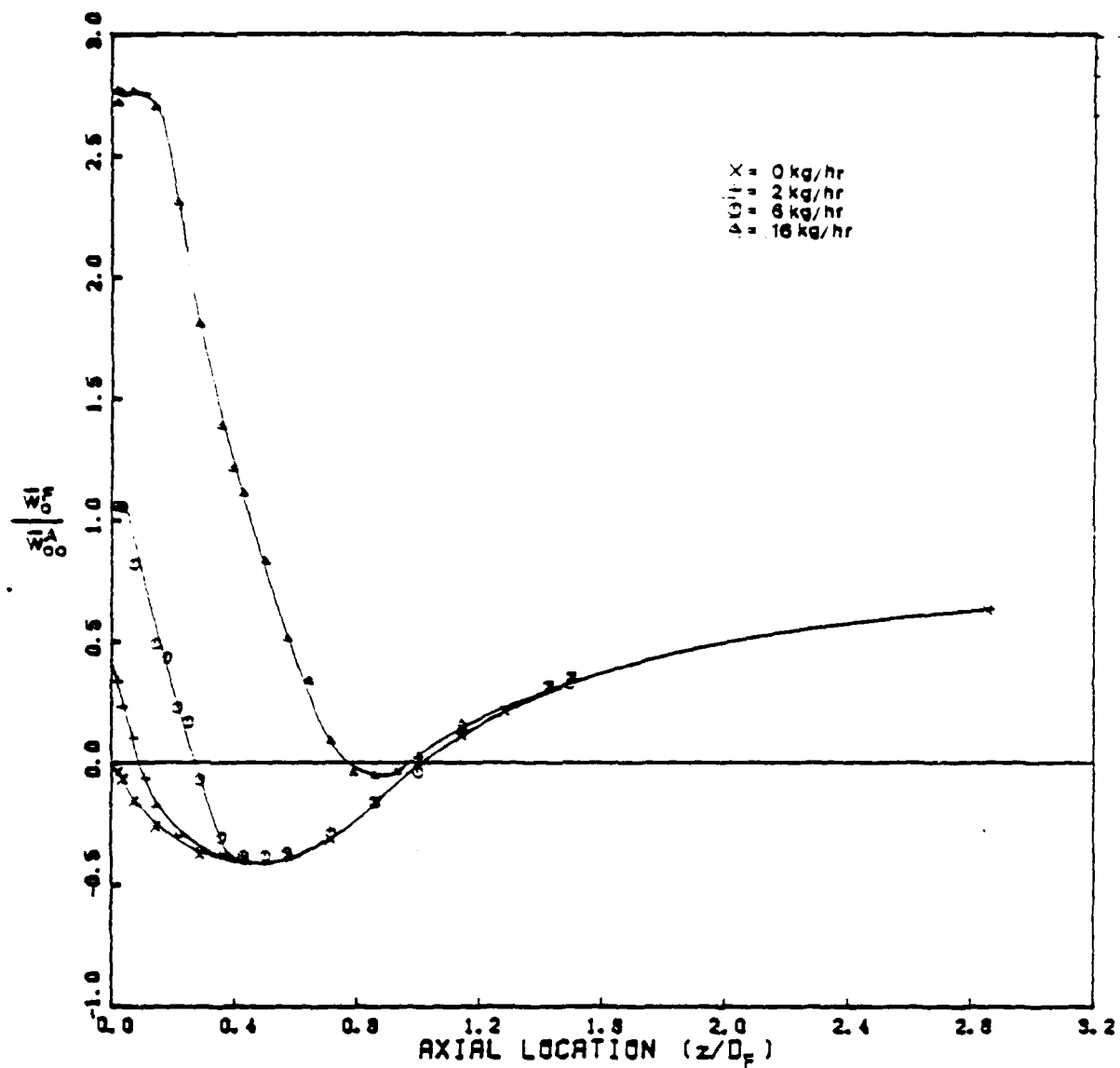


Figure 32. Normalized Centerline Axial-Velocity Profiles Showing the Influence of the Central Jet on the Centerline Recirculation for Each Central Jet Flow Studied.

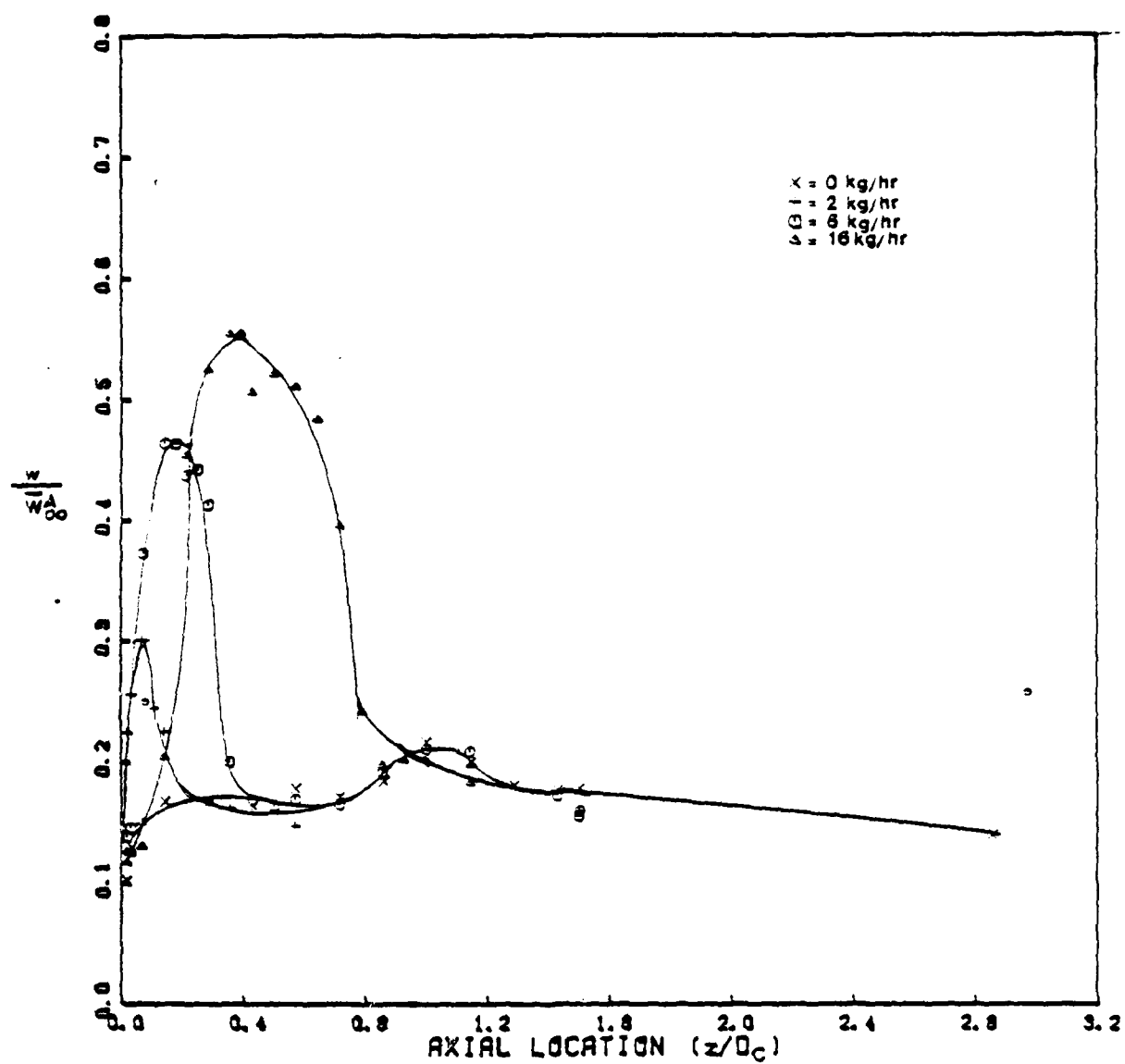


Figure 33. Normalized RMS Axial-Velocity Fluctuation Profiles.

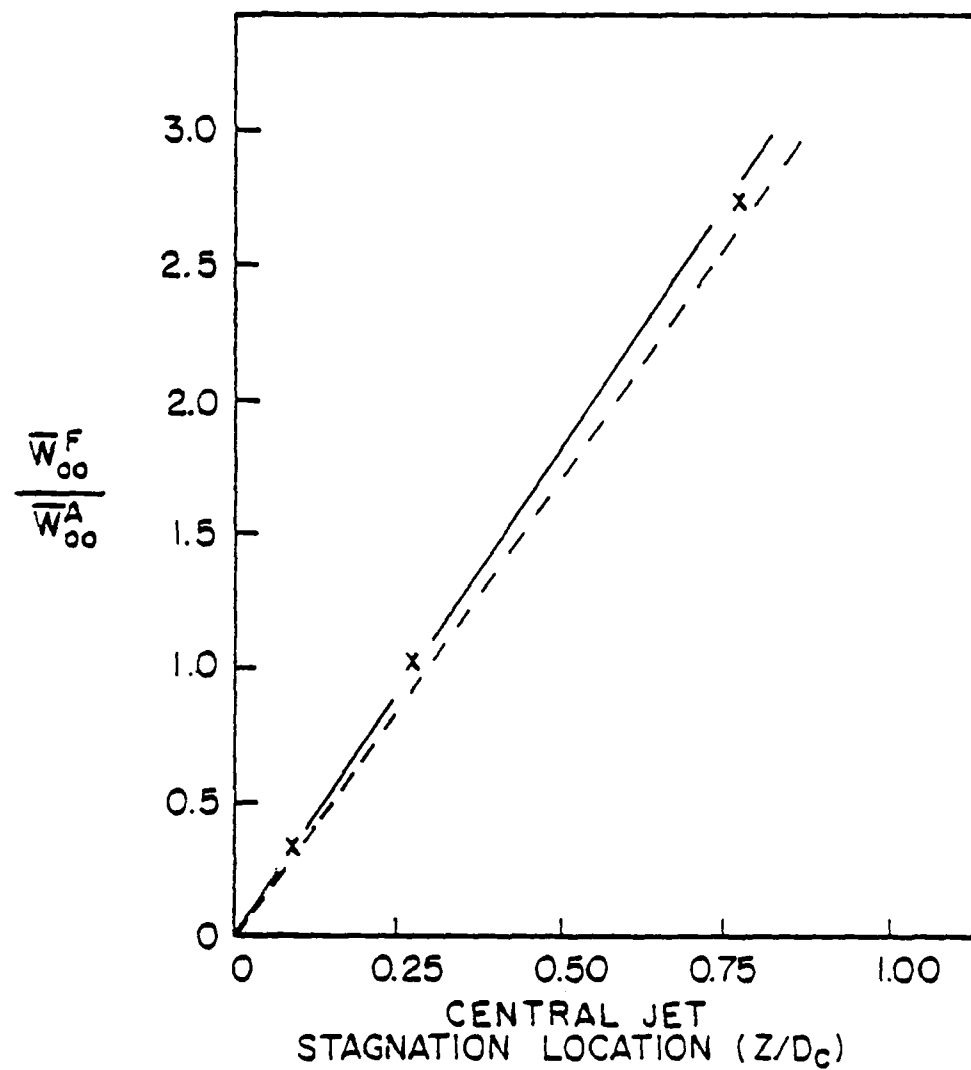


Figure 34. Central Jet Centerline Stagnation Location Plotted as a Function of the Central Jet Entrance Velocity. Results of previous measurements with different nozzle are shown for comparison (----).

## SECTION 5

### CONCLUSIONS

A two-dimensional Laser Doppler Anemometer has been designed and constructed for use in a ducted coaxial flow system having a centerbody. The LDA has been used to take measurements in the flowfield in three flow conditions: central-jet-only; annular-jet-only; and coaxial flow. The measurements have provided the information needed to compute the mean value of the velocity component and the fluctuating component. In addition higher moments of the distributions have been computed.

The parameters describing the central-jet-only measurements have been compared with the standard descriptions obtained by past investigators who have used photography, hot-wire, and other study techniques. The central-jet-only measurements have also been used with concentration measurements made by intrusive probes under the same operating conditions, to compute the entrainment of the surrounding fluid into the jet.

The jet half-maximum-velocity width has the usual development shape, but the asymptotic linear growth for this CO<sub>2</sub> into air jet is at a much higher rate than observed for the air jet into air studies,  $\phi_{1/2}/(Z+a)$  is 0.262 vs 0.17. The entrainment factor  $C_2$  is constant in these studies over the range  $0 < Z/D_f < 10$ , not showing the growth region observed by Hill, and the value observed 0.24 is larger than that obtained by Boguslawski and Popiel (0.18) for an air jet into air. Also, no marked dependence of  $C_2$  on Reynolds number was observed over the range studied  $11,000 < Re < 83,000$ , in contrast to the earlier results of Ricou and Spalding, although their measurements were in a region much farther downstream. Beyond  $Z/D_f \approx 10$  the value of  $C_2$  increases to 0.32 matching the value obtained by Ricou and Spalding. Consistency checks made on the central jet have shown that the mass flow of CO<sub>2</sub> is constant downstream, even in the



presence of a 20 fold increase in mass by the air entrained and, also, the jet momentum is conserved. Both these results give confidence in the measured values.

The annular-jet-only flowfield has been mapped extensively in the region of the wake of the centerbody and downstream from it. The recirculation vortex has been studied and the center located in the region  $0.34 < r/D_c < 0.38$  and  $0.36 < Z/D_c < 0.43$ , and the maximum strength streamline observed had the value  $-0.065$ . The recirculation zone extends downstream, on centerline for a distance  $Z/D_c \sim 0.97$ . To test the consistency of the measurements the mass flow was computed for each velocity profile measured and at every station the value obtained was the inlet mass  $\pm 3\%$ . The axial momentum flow of the annular jet started at the value of the annular flow flat-top entrance profile. It decreased downstream until, at a position well past the stagnation point, it approached the value describing a flat-top velocity profile across the duct. After this point it began to increase, but in the relatively short length of duct observable,  $Z/D_c = 4.29$  maximum, it did not have time to reach the value associated with fully developed pipe flow.

The coaxial flow profile measurements traced the decay of the central jet due to the action of the reverse jet set up by the annular flow recirculation vortex. As the velocity change resulting from the central jet diminishes, the rms fluctuation increases strongly, indicating the great amount of mixing occurring in the region near the central jet stagnation location. In combustion studies, a flame ball is usually observed in this region giving visual evidence to the mixing. Centerline profiles were measured for three central jet flow rates, and the results obtained showed good agreement with previous measurements obtained with a one-dimensional LDA.

APPENDIX A

CO<sub>2</sub> CONCENTRATION MEASUREMENT PROFILES  
FOR CENTRAL JET FLOWS INTO AIR

## APPENDIX A

The  $\text{CO}_2$  concentration measurements of Bradley,<sup>19</sup> in the region  $z/D_F > 20$ , have been fit to functional dependence of the same form as the LDA measurements. The result is

$$C_{\text{CO}_2}(r, z) = (1 - e^{-3.8 \frac{1}{z/D_F - 6.7}}) e^{-2.67 \left( \frac{r}{z/D_F - 2} \right)^2} \quad (\text{A.1})$$

where  $C_{\text{CO}_2}$  is the fractional concentration of  $\text{CO}_2$  in the gas sampled at location  $(r, z)$  [both in mm].

In the same region the LDA was shown to have the relationship (for 2 and 6 kg/hr of  $\text{CO}_2$ )

$$\bar{w}^F(r, z) = (1 - e^{-6.8 \frac{1}{z/D_F - 5.2}}) e^{-2.29 \left( \frac{r}{z/D_F - 4.8} \right)^2} \quad (\text{A.2})$$

The general fit to the data is quite good. There are some points though that should be noted. First, the numerical coefficients in the two equations are not the same as would be expected for fully developed turbulent flow. Second, the location of the virtual origin is different in each exponential expression contrary to what was expected.<sup>20</sup> The discrepancies do not appear to be unreconcilable. They may be due to experimental error and/or to the fact that the data used was not from a region far enough downstream to represent the truly self-similar region of the fluid flow. Further study will be required to resolve the issue.

# REFERENCES

1. F. Durst, A. Melling, and J. H. Whitelaw, Principles and Practices of Laser-Doppler Anemometry, Academic Press, New York, 1976.
2. P. D. Magill, A. J. Lightman, C. E. Orr, R. P. Bradley, and W. M. Roquemore, "Flowfield and Emission Studies in a Bluff Body Combustor," AIAA-82-0883, AIAA/ASME 3rd Joint Thermophysics, Fluids, Plasma and Heat Transfer Conference, St. Louis, Missouri, June 1982.
3. P. K. Snyder, K. L. Orloff, and K. Aoyagi, "Performance and Analysis of a Three Dimensional Laser Doppler Anemometer," NASA TM-81283, 1981.
4. TSI, Model 9100-10, LDV System for Three Component Measurement.
5. Maxlight, Optical Waveguides, KSC200B Series.
6. D. K. McLaughlin and W. G. Tiederman, "Biasing Correction for Individual Realization Laser Anemometer Measurements in Turbulent Flows," Phys. Fluids 16, 2082, 1973.
7. W. Hoesel and W. Rodi, "New Biasing Elimination Method for Laser Doppler Velocimeter Counter Processing," Rev. Sci. Instrum. 48, 910, 1977.
8. P. Buchhave, W. K. George, and J. L. Lumley, "The Measurements of Turbulence with the Laser Doppler Anemometer," Ann. Rev. Fluid Mech. 11, 443, 1979.
9. R. V. Edwards, private communication.
10. T. C. Roesler, W. H. Stevenson, and H. D. Thompson, "Investigation of Bias Errors in Laser Doppler Velocimeter Measurements," AFWAL-TR-80-2105, 1980.
11. A. Yariv, Quantum Electronics, Wiley, New York, 1975.
12. P. T. Harsha, "Free Turbulent Mixing: A Critical Evaluation of Theory and Experiment," AEDC-TR-71-36, AEDC, TN, 1971.
13. ASME PTC 19.5; 4-1959 Long-Radius Flow Nozzles for Code Tests, Low B Series.
14. A. J. Yule, "Investigations of Eddy Coherence in Jet Flows," Lecture Notes in Physics 136, Springer-Verlag, 1981.

15. F. P. Ricou and D. B. Spalding, "Measurements of Entrainment by Axisymmetrical Turbulent Jets," *J. Fluid Mech.* 11, 21, 1961.
16. B. J. Hill, "Measurement of Local Entrainment Rate in the Initial Region of Axisymmetric Turbulent Air Jets," *J. Fluid Mech.* 51, 773, 1972.
17. S. C. Crow and F. H. Champagne, "Orderly Structure in Jet Turbulence," *J. Fluid Mech.* 48, 547, 1971.
18. L. Boguslawski and Cz. O. Popiel, "Flow Structure of the Free Round Turbulent Jet in the Initial Region," *J. Fluid Mech.* 90, 531, 1979.
19. R. P. Bradley, W. M. Roquemore, J. S. Stutrud, C. M. Reeves, and C. M. Obringer, "Second Data Set for APL Combustor," 1982.
20. J. O. Hinze, Turbulence, McGraw-Hill, New York, 1975, pp. 535-533.
21. W. Forstall, Jr., Material and Momentum Transfer in Coaxial Gas Streams, Ph.D. Thesis, MIT, Cambridge, Massachusetts, 1949.
22. J. O. Hinze and B. G. Van der Hegge Zijnen, "Transfer of Heat and Matter in the Turbulent Mixing of an Axially Symmetrical Jet," *Appl. Sci. Res.* A1, 435, 1949.
23. W. Rodi, "A New Method of Analyzing Hot-Wire Signals in Highly Turbulent Flow, and Its Evaluation in a Round Jet," *DISA Inf.* 17, 9, 1975.
24. C. DuP. Donaldson, R. S. Snedeker, and D. P. Margolis, "A Study of Free Jet Impingement, Part 2.," *J. Fluid Mech.* 45, 477, 1971.
25. I. Wygnanski and H. E. Fiedler, *J. Fluid Mech.* 38, 577, 1969.
26. A. J. Lightman and P. D. Magill, "Velocity Measurements in Confined Dual Coaxial Jets Behind an Axisymmetric Bluff Body: Isothermal and Combusting Flows," AFWAL-TR-81-2013, 1981.
27. A. A. Townsend, The Structure of Turbulent Shear Flow, Cambridge University Press, Cambridge, Massachusetts, 1976.

END

FILMED

12-83

DTIC